Theoretische Physik

Analysis of complex systems: From stochastic time series to pattern formation in microscopic fluidic films

Inaugural-Dissertation zur Erlangung des Doktorgrades der Naturwissenschaften
im Fachbereich Physik der Mathematisch-Naturwissenschaftlichen Fakultät
der Westfälischen Wilhelms-Universität Münster

vorgelegt von
Christoph Honisch
aus Düsseldorf

– 2013 –

Westfälische
Wilhelms-Universität
Münster

Dekan:	Prof. Dr. Markus Donath
Erster Gutachter:	Prof. Dr. Uwe Thiele
Zweiter Gutachter:	Prof. Dr. Joachim Peinke
Tag der mündlichen Prüfung:	24.01.2014
Tag der Promotion:	24.01.2014

In memory of

Prof. Dr. Rudolf Friedrich
17.11.1956 – 16.08.2012

Abstract

The current thesis consists of two parts, both of which are dealing with the analysis of complex systems, one with stochastic time series analysis and one with pattern formation in microscopic fluid layers.

The first part is about an analysis method which allows to extract stochastic order parameter equations from measured time series data. Employing this method termed *Kramers-Moyal analysis*, significant problems can occur if the temporal resolution of the measurement data is not sufficient. In the course of this thesis it is analyzed what the term “sufficient” means in this context, and where the limitations of the applicability of the Kramers-Moyal analysis are. Furthermore, the analysis method is extended in order to be able to analyze data with small sampling frequencies more reliably. In this context an estimation of the uncertainties of determined model parameters plays an important role. The latter is done via a Monte Carlo error propagation technique.

First, the extended method is tested employing examples of synthetic data. Then, an application to real-world data from an optical tweezers experiment is performed. In this experiment a micrometer-sized particle diffusing in a fluid is trapped in the center of a highly focused laser beam. The particle then performs Brownian motion subject to an external force that is induced by the optical light pressure of the laser beam, whereas the motion of the particle is filmed by a CCD camera. Subsequently, the positions of the particle are extracted from the recorded images.

An analysis of the measurement data shows a surprisingly large Markov-Einstein time scale, which can be traced back to hydrodynamic memory effects. Above this time scale the process can be mapped to an Ornstein-Uhlenbeck process via the application of the developed extended method. This is in agreement with the classical theory of overdamped Brownian motion.

In the second part of the thesis, an experiment in the field of organic semiconductor research is modeled. The goal of these experiments is to deposit ordered structures of thin layers of small organic semiconducting molecules onto a substrate. This is done via organic molecular beam deposition. Within this technique organic molecules are sublimed at high temperatures in vacuum and subsequently condense onto a cooled substrate. In order to create ordered structures on the substrate, the latter is prestructured with inorganic substances, such that the organic molecules preferably accumulate at

specific sites. One specific type of experiments is regarded, where the prestructure consists of periodic gold stripes on a SiO_2 substrate. Depending on the geometry of the prestructure and the amount of deposited material, instabilities are observed that hinder the formation of homogeneous ridges on top of the gold stripes.

In order to provide a theoretical description of the experiments, a so-called thin film equation is employed that describes the dynamics of the height profile of the layer of deposited molecules on the substrate. Based on this equation, the linear stability of stationary solutions is analyzed that form ridges centered on the gold stripes. This stability analysis is performed employing numerical continuation. Thereby two instabilities are found which are also observed in the experiments. If the amount of deposited molecules is too small, a ridge breaks up into small droplets on the gold stripe. If too much material is deposited, large bulges form which also partly cover the bare substrate between the gold stripes. For both instabilities direct numerical simulations are performed to analyze the full nonlinear dynamics.

Kurzfassung

Die vorliegende Dissertation besteht aus zwei Teilen, die sich beide mit der Analyse komplexer Systeme beschäftigen, der eine mit stochastischer Zeitreihenanalyse und der andere mit Strukturbildung in mikroskopischen Flüssigkeitsschichten.

Der erste Teil behandelt eine Analysemethode, mit deren Hilfe stochastische Ordnungsparametergleichungen aus gemessenen Zeitreihen gewonnen werden können. Bei dieser Methode, *Kramers-Moyal-Analyse* genannt, können erhebliche Probleme auftreten, wenn die zeitliche Auflösung der Messdaten nicht hinreichend groß ist. Im Rahmen der Arbeit wird zunächst untersucht, was "hinreichend" in diesem Zusammenhang bedeutet und wo die Grenzen der Anwendbarkeit der Kramers-Moyal-Analyse liegen. Darüber hinaus wird die Analysemethode erweitert, um Messdaten mit kleiner Samplingfrequenz verlässlicher analysieren zu können. Eine wichtige Rolle spielt dabei die Abschätzung der Ungenauigkeit der gewonnenen Modellparameter. Diese erfolgt mittels einer Monte-Carlo-Fehlerfortpflanzungsmethode.

Die weiterentwickelte Methode wird zunächst an Beispielen mit synthetisch erzeugten Daten getestet. Des Weiteren erfolgt eine Anwendung auf echte Messdaten aus einem Experiment mit optischen Pinzetten. In diesem Experiment wird ein mikrometergroßes Kügelchen, das in einer Flüssigkeit diffundiert, im Zentrum eines stark fokussierten Laserstrahls gefangen. Das Kügelchen vollführt dann eine brownsche Bewegung unter dem Einfluss einer externen Kraft, die durch den Lichtdruck des Lasers hervorgerufen wird. Dabei wird die Bewegung der Kügelchen wird mit einer CCD-Kamera gefilmt. Anschließend wird aus den aufgenommenen Bildern eine Zeitreihe der Positionen des Kügelchens bestimmt.

Eine Analyse der Messdaten zeigt eine überraschend große Markov-Einstein-Zeitskala, die auf hydrodynamische Gedächtniseffekte zurückgeführt werden kann. Oberhalb dieser Zeitskala kann der Prozess durch Anwendung der weiterentwickelten Methode auf einen Ornstein-Uhlenbeck-Prozess abgebildet werden, was im Einklang mit der klassischen Theorie überdämpfter brownscher Bewegung steht.

Im zweiten Teil der Arbeit wird ein Experiment aus der organischen Halbleiterforschung theoretisch modelliert. In diesen Experimenten wird versucht, geordnete Strukturen dünner Schichten aus kleinen organischen, halbleitenden Molekülen auf ein Substrat aufzutragen. Letzteres erfolgt über eine Methode namens Organic Molecular

Beam Deposition. Dabei werden die organischen Moleküle im Vakuum bei hohen Temperaturen sublimiert und kondensieren anschließend auf einem gekühlten Substrat. Um Strukturen auf dem Substrat zu erzeugen, wird dieses vorher mit anorganischen Substanzen vorstrukturiert, so dass die organischen Moleküle sich vorzugsweise an bestimmten Stellen ansammeln. Konkret werden Experimente betrachtet, in denen die Vorstrukturierung aus periodischen Goldstreifen auf einem SiO_2-Substrat besteht. In Abhängigkeit der Geometrie der Vorstrukturierung und der Menge der aufgedampften Moleküle werden Instabilitäten beobachtet, die eine homogene Beschichtung der Goldstreifen verhindern.

Um diese Experimente theoretisch zu beschreiben, wird eine sogenannte Dünnfilmgleichung für die Zeitentwicklung des Höhenprofils der Schicht aufgedampfter Moleküle auf dem Substrat verwendet. Anhand dieser Gleichung wird die lineare Stabilität von stationären Lösungen untersucht, welche die Form von auf den Goldstreifen zentrierten Kämmen haben. Diese Stabilitätsanalyse erfolgt mittels numerischer Kontinuierung. Dabei werden zwei Instabilitäten gefunden, die auch in den Experimenten beobachtet werden. Bei zu geringen Mengen aufgedampfter Moleküle zerfällt ein Kamm in kleine Tropfen auf dem Streifen. Bei zu großen Mengen bilden sich große Beulen, die auch das Substrat zwischen den Goldstreifen bedecken. Für beide Instabilitäten werden außerdem direkte numerische Simulationen durchgeführt, um die volle nichtlineare Dynamik zu analysieren.

Contents

List of abbreviations

ACF	autocorrelation function
AFM	atomic force microscopy
AFPE	adjoint Fokker-Planck equation
AMISE	approximate mean integrated squared error
BDF	backward differentiation formulae
CKE	Chapman-Kolmogorov equation
DtCDQA	$N, N'-$di[(N-(3,6-di-*tert*-butyl-carbazyl))-n-decyl] quinacridone
DNS	direct numerical simulation
DP	disjoining pressure
EIP	effective interface potential
FD	finite difference
FPE	Fokker-Planck equation
KM	Kramers-Moyal
LWS	less wettable stripe
MCEP	Monte Carlo error propagation
ME	Markov-Einstein
MISE	mean integrated squared error
MSD	mean squared displacement
MSE	mean squared error
MWS	more wettable stripe
NPB	N, N'-bis(1-naphyl)-N, N'-diphenyl-$1,1'$-biphenyl-4,$4'$-diamine
ODE	ordinary differential equation
OLED	organic light emitting diode
OMBD	organic molecular beam deposition
OU	Ornstein-Uhlenbeck
PDE	partial differential equation
PDF	probability density function
RHS	right hand side
SRT	Silverman's rule of thumb
VTE	vacuum thermal evaporation

1 Introduction

The current thesis deals with the analysis of complex systems. Complex systems are ubiquitous and play a tremendously important role in our every-day life. If one only considers, for instance, the climate, financial markets or modern power grids, it becomes clear that understanding complex systems is of immense importance for several great challenges humanity faces today. While physicists had great successes in understanding the fundamental interactions of nature during the last few hundred years, culminating in the recent experimental detection of the Higgs boson, we are still far away from understanding the various complex structures created by nature or societies.

What is a complex system? According to the preamble of the Springer Series in Synergetics edited by Hermann Haken, complex systems "[...] are composed of many parts which interact with one another in a more or less complicated manner" (see, e. g., [Hak04]). If such systems are driven out of equilibrium by some external fluxes, they might spontaneously develop spatial, temporal, spatio-temporal or functional structures, a process we call *self-organization*. Demonstrative examples for these different types of structures are animal coat patterns [KM94], synchronization [ABV$^+$05, PM03], convection rolls in the Rayleigh-Bénard experiment [AGL09], and the behavior of humans or animals resulting from neural interactions in their brains.

A mathematical understanding of the emergence of ordered structures or patterns is provided by *synergetics*, Haken's theory of self-organization [Hak04, Hak00, Hak09]. According to this theory, self-organization is accompanied by a dramatic reduction of the relevant degrees of freedom. In the vicinity of a non-equilibrium phase transition that leads to the emergence of ordered structures, it comes to a separation of time scales of the dynamics of the different degrees of freedom. As a consequence, only a few of them, the so-called *order parameters*, determine the dynamics of the system and enforce the emergence of macroscopic patterns.

This reduction of the effective dimensionality of a complex system makes it possible to establish mathematical models one can analyze. In some cases it is possible to derive equations of motion for the macroscopic order parameters directly from the interactions of the microscopic subsystems as Haken demonstrated for the laser [Hak85]. This can be regarded as a *bottom-up* approach to model a complex system. If the interactions of the microscopic subsystems are not known or simply too complex, one has to find another strategy. With the maximum information principle [Hak00], Haken provides a so-called *top-down* approach to describe complex systems. Employing this principle, one can set up a model for macroscopic observables by measuring specific expectation values of these observables from experimental data. One famous application of this method is the Haken-Kelso experiment [HKB85].

The first part of this thesis develops further another top-down approach that was introduced in 1997 by Friedrich and Peinke [FP97b, FP97a]. In order to analyze the statistical properties of the turbulent cascade, they mapped the velocity increments of a turbulent flow field onto a Markov process in scale and demonstrated how to measure the drift and diffusion coefficients of a Fokker-Planck equation from measured data. This method, today referred to as *Kramers-Moyal analysis*, has since then been applied to many different complex systems in the natural sciences as well as in medicine, finance and engineering (cf. [FPST11, FPT09] and references therein).

The first part of the current thesis provides a detailed analysis of the problems that arise when the Kramers-Moyal analysis is applied to data sets that are sampled with an insufficient resolution. Since most objects of the Kramers-Moyal analysis are processes in time, these problems are termed finite time effects. An underestimation of the significance of this problem can lead (and has led) to estimated models that in the worst case do not at all reflect the real process.

Chapter 2 of this thesis gives an introduction into the field of Kramers-Moyal analysis and reviews the necessary knowledge about stochastic processes. Chapter 3 presents two data analysis techniques that will be employed in the later analyses. The next chapter contains the discussion about finite time effects. An improved method is introduced that is suitable for the analysis of data sets measured with an insufficient sampling frequency. Chapter 5 presents an application of the extended method to experimental data of an optical trapping experiment. Finally, the first part of this thesis is concluded in Chap. 6.

The second part of the thesis employs a bottom-up approach to describe a specific complex system that arises in experiments in the field of organic semiconductor research. The goal of these experiments is to produce thin layers of organic semiconducting material that are structured on a length scale that should be as small as possible. This is done by a technique termed area-selective growth. This means that the substrate onto which the organic material is deposited is chemically prestructured in a way that the deposited material prefers to accumulate at specific sites to form, e. g., homogeneous ridges. In dependence of the geometry of the prestructure and the amount of deposited material, certain instabilities are observed that hinder the formation of the intended structures.

In this case the macroscopic observable is the height profile of the deposited material. Its dynamics is described by a thin film equation [ODB97, Thi10]. Employing such an equation it is analyzed under which conditions the unwanted instabilities occur. This is done by a transversal linear stability analysis. The findings of this analysis are complemented by direct numerical simulations.

The second part starts with an introductory chapter that reviews organic semiconductor research and theoretical approaches to model these systems. The specific experiments that are investigated in the course of this thesis are described in detail in Chap. 8. Based on the experimental results, the here employed theoretical description is motivated. Chapter 9 provides the basic theory including a sketch of the derivation of the thin film equation and an explanation of the specific form used here. The numerical methods that are employed to analyze the model are the subject of Chap. 10. Chapter 11 contains the transversal linear stability analysis, followed by a chapter presenting the direct numerical simulations. The thesis closes with a conclusion in Chap. 13.

Part I

Stochastic time series analysis

2 From complex systems to Kramers-Moyal analysis

As described in the introduction of the previous chapter, the first part of this thesis is about a top-down approach to model complex systems, the *Kramers-Moyal* (KM) *analysis*. It allows one to extract models in form of Fokker-Planck equations (FPEs) or corresponding Langevin equations from stochastic time series data employing data analysis techniques. This first chapter will give an introduction into this field and will provide the necessary theoretical background about stochastic processes.

First of all, Sect. 2.1 will start with a motivation of the KM analysis which lies in the analysis of complex systems. The next section is about different classes of stochastic processes with special emphasis on Markov processes. Section 2.3 introduces the FPE for Gaussian Markov processes, followed by a section about the Langevin equation. Finally, Sect. 2.5 introduces the KM analysis technique.

2.1 Analyzing complex systems

When people try to model a complex system consisting of a large number of degrees of freedom, they are usually interested in the behavior of a few macroscopic observables. If we consider the financial markets as an every-day life example, such a macroscopic observable could be a stock index or an exchange rate. In the case of the human brain, probably the most complex system nature has ever created, one could consider an EEG signal. The dynamics of these observables often display some kind of order together with random fluctuations that stem from the large number of degrees of freedom involved in the system. Therefore, one has to deal with stochastic processes. We forego a review of basic probability theory and refer the reader to textbooks like, e. g., [Ris89, VK07, Gar86].

The most comprehensive information a model of a stochastic process can provide is the N-point probability density function (PDF)

$$f_N(q_N, t_N;\, q_{N-1}, t_{N-1}; \dots ; q_1, t_1)\,. \tag{2.1}$$

Given N points in time $t_1 < t_2 < \cdots < t_N$, the N-point PDF provides the probability that a stochastic process $Q(t)$ assumes the values $q_1, \dots, q_N$ at the N points in time, respectively. If the N-point PDF is known, we are able to compute every expectation value we are interested in. The process $Q(t)$ can be univariate or multivariate, i. e., Q can be a scalar or vector variable, respectively.

For a general stochastic process it is of course practically impossible to obtain the N-point PDF for arbitrary N via data analysis techniques. However, if the process has some specific properties, or can be approximated by processes that have these properties, it becomes possible to obtain the N-point PDF.

2.2 Classes of stochastic processes

The N-point PDF f_N can be split up into a product of a conditional PDF p and an $(N-1)$-point PDF f_{N-1}, like

$$f_N(q_N, t_N; \dots; q_1, t_1) = p(q_N, t_N \,|\, q_{N-1}, t_{N-1}; \dots; q_1, t_1) \cdot f_{N-1}(q_{N-1}, t_{N-1}; \dots; q_1, t_1)\,. \tag{2.2}$$

Depending on the properties of the conditional PDF, also referred to as *transition PDF* in this context, one can devide stochastic processes into different classes.

2.2.1 Pure noise

The easiest class of stochastic processes is pure, uncorrelated noise. This means that the transition PDF satisfies

$$p(q_N, t_N \,|\, q_{N-1}, t_{N-1}; \dots; q_1, t_1) = f_1(q_N, t_N) \tag{2.3}$$

An iterated application of Eq. (2.2) with (2.3) yields

$$f_N(q_N, t_N; \dots; q_1, t_1) = \prod_{i=1}^{N} f_1(q_i, t_i)\,. \tag{2.4}$$

This means that the N-point PDF of a process of uncorrelated noise can be split up into a product of one-point PDFs, which can be estimated from an ensemble of realizations of the process. If the process is furthermore stationary, the estimation of one PDF suffices to gain the complete information about the whole process.

2.2.2 Markov processes

The second easiest class of processes are *Markov processes*. These are defined by the property

$$p(q_N, t_N \,|\, q_{N-1}, t_{N-1}; \dots; q_1, t_1) = p(q_N, t_N \,|\, q_{N-1}, t_{N-1})\,. \tag{2.5}$$

Looking at the definition of a Markov process, one can realize the enormous utility of a mathematical statement because it is very hard to express the exact meaning of this statement in words. Here is a try: If we know that the process $Q(t)$ is in the state q_{N-1} at the current time t_{N-1}, the probability of finding the realization q_N in the future time t_N does not change if we add further information about the past of the process before time t_{N-1}. Therefore, it is often said that a Markov process has no "memory" because it has "forgotten" the information about its past. To get an intuitive understanding of the Markov property, it might be helpful to provide examples for non-Markovian processes.

Consider for example the state variable Q of a harmonic oscillator with a weak δ-distributed noise. Let the oscillator be in the state $q_i = 0$ at time t_i. If we do not know what happened before time t_i, the probability of finding the oscillator at some $q_{i+1} > 0$ at time t_{i+1} is equal to the probability of finding it at $-q_{i+1}$. On the other hand, if we add the information that the oscillator was in the state $q_{i-1} < 0$ at time t_{i-1} closely before t_i, it is more probable to find the oscillator at $q_{i+1} > 0$ at time t_{i+1} than finding it at $-q_{i+1}$ because the velocity $\dot{q}_i$ is probably positive. In this case the relation (2.5) does not hold true. However, if we consider the state Q together with its first derivative $\dot{Q}$, this bivariate process is Markovian. If we know q_i and $\dot{q}_i$ at time t_i, additional information about the past will not change our forecast for the future. Another example for non-Markovianity are processes with correlated noise. If the influence of positively correlated noise was positive in the past, it is more probable that it is positive now. Therefore, the knowledge about the past changes our forecast for the future.

From the first example we can learn that non-Markovianity sometimes results from disregarding relevant degrees of freedom of a system. In those cases it is possible to construct a Markov process by embedding the process into a higher-dimensional phase space. One possibility is the well-known delay embedding that is often used to obtain attractors in classical (non-stochastic) nonlinear time series analysis [KS03].

The second example leads us to the notion of the *Markov-Einstein* (ME) *time scale*. If we consider a correlated noise term $\Gamma(t)$ with an autocorrelation like

$$\langle\, \Gamma(t)\Gamma(t')\, \rangle = \mathrm{e}^{-\gamma(t-t')} \tag{2.6}$$

we have a finite correlation time $\tau_c = \gamma^{-1}$. Then, Eq. (2.5) is approximately valid if the time increment $t_N - t_{N-1} \gg \tau_c$. This implies that there exists a time scale τ_{ME} such that Eq. (2.5) is approximately valid for time increments $t_N - t_{N-1} > \tau_{\mathrm{ME}}$. We call τ_{ME} the ME time scale. That means that as long as we sample the process with sampling intervals larger than τ_{ME}, the process appears to be Markovian.

Now we come back to the N-point PDF. If Eq. (2.5) is valid, f_N can be written as a product over two-point conditional PDFs

$$f_N(q_N, t_N; \ldots; q_1, t_1) = f_1(q_1, t_1) \prod_{i=1}^{N-1} p(q_{i+1}, t_{i+1} | q_i, t_i)\,. \tag{2.7}$$

If the process is furthermore stationary, the two-point conditional PDFs only depend on the time increments $t_{i+1} - t_i$. That means that the function $p_\tau(q' \,|\, q) := p(q', t+\tau \,|\, q, t)$ completely defines the process. It should be noted that if p_τ is known, one can also compute $p_{2\tau}$ via the Chapman-Kolmogorov equation (CKE), which we derive now:

$$\begin{aligned} p_{2\tau}(q'' \,|\, q) &= \frac{f_2(q'', q)}{f_1(q)} \\ &= \frac{\int \mathrm{d}q' \, f_3(q'', q', q)}{f_1(q)} \\ &= \frac{\int \mathrm{d}q' \, f_1(q) \, p_\tau(q'' \,|\, q') \, p_\tau(q' \,|\, q)}{f_1(q)} \\ &= \int \mathrm{d}q' \, p_\tau(q'' \,|\, q') \, p_\tau(q' \,|\, q) \end{aligned} \tag{2.8}$$

Therefore, it suffices to determine the transition PDF p_τ for one small increment τ to get the complete information about a stationary Markov process.

2.2.3 Higher order processes

In principle one can extend our classification scheme by processes that obey the relations

$$p(q_N, t_N \,|\, q_{N-1}, t_{N-1}; \ldots; q_1, t_1) = p(q_N, t_N \,|\, q_{N-1}, t_{N-1};\; q_{N-2}, t_{N-2}), \tag{2.9}$$

$$p(q_N, t_N \,|\, q_{N-1}, t_{N-1}; \ldots; q_1, t_1) = p(q_N, t_N \,|\, q_{N-1}, t_{N-1};\; q_{N-2}, t_{N-2};\; q_{N-3}, t_{N-3}) \tag{2.10}$$

and so on. But we will not discuss these processes here.

2.3 The Fokker-Planck equation

In the last section we classified stochastic processes according to their transition PDFs, but we did not regard the specific forms of the transition PDFs. Regarding the functional forms of transition PDFs, there is one class of Markov processes that allows for a further dramatic simplification. This is when the transition PDFs $p(q, t \,|\, q', t')$ converge towards a Gaussian distribution in the limit $t - t' \to 0$. In this case it is sufficient to determine the first two moments of the transition PDFs in the limit of small time increments in order to get the complete information about the process. This is because the KM expansion stops in this case and results in the FPE.

With use of a Taylor expansion of the CKE, Eq. (2.8), one can derive the KM expansion (in one dimension) [Ris89]

$$\frac{\partial}{\partial t} p(q, t \,|\, q', t') = \sum_{i=1}^{\infty} \left(-\frac{\partial}{\partial q}\right)^n D^{(n)}(q, t) p(q, t \,|\, q', t'), \tag{2.11}$$

where $D^{(n)}$ are the KM coefficients

$$D^{(n)}(q,t) = \lim_{\tau\to 0} \frac{1}{n!\tau} \langle (Q(t+\tau) - Q(t))^n \,|\, Q(t) = q \rangle \,. \tag{2.12}$$

These coefficients will be discussed in more detail in Sect. 2.5. The Pawula theorem [Ris89] states that if $D^{(3)} = 0$, all higher moments vanish, too, i. e., $D^{(k)} = 0 \;\forall k \geq 3$. Then Eq. (2.11) becomes the FPE

$$\frac{\partial}{\partial t} p(q,t\,|\,q',t') = \left[-\frac{\partial}{\partial q} D^{(1)}(q,t) + \frac{\partial^2}{\partial q^2} D^{(2)}(q,t) \right] p(q,t\,|\,q',t') \,. \tag{2.13}$$

The initial condition of this partial differential equation (PDE) must of course be

$$p(q,t'\,|\,q',t') = \delta(q-q') \,. \tag{2.14}$$

As long as the KM coefficients depend explicitly on time, the formal solution of the FPE is given by an unhandy Dyson series (cf. [Ris89]), the first terms of which are

$$\begin{aligned} p(q,t\,|\,q',t') \simeq & \left[1 + \left(-\frac{\partial}{\partial q} D^{(1)}(q,t) + \frac{\partial^2}{\partial q^2} D^{(2)}(q,t) \right) (t-t') + O((t-t')^2) \right] \\ & \times \delta(q-q') \,. \end{aligned} \tag{2.15}$$

From this one can deduce the *short time propagator*, i. e. the transition PDF in the limit $\tau = t - t' \to 0$:

$$p(q,t+\tau\,|\,q,',t) = \frac{1}{2\sqrt{\pi D^{(2)}(q',t)\tau}} \exp\left(-\frac{[q - q' - D^{(1)}(q',t)\tau]^2}{4D^{(2)}(q',t)\tau} \right) . \tag{2.16}$$

As was pointed out in the beginning of this section, it is a Gaussian distribution with mean value $q' - D^{(1)}(q',t)\tau$ and variance $2D^{(2)}(q',t)\tau$. This gives us an understanding of the KM coefficients $D^{(1)}$ and $D^{(2)}$. $D^{(1)}$, also referred to as the *drift* coefficient, determines where the process will go to on average. The second term $D^{(2)}$, also called the *diffusion* coefficient determines the strength of the stochastic influence and therefore the uncertainty about what the process will do.

To summarize, the FPE is a PDE which determines the time evolution of the transition probability of a Gaussian Markov process. It depends on two coefficients, the drift and the diffusion term. Thus, if these two quantities are known, we can compute the transition probabilities for arbitrary time increments and can set up every N-point PDF that we are interested in.

For the sake of completeness, the FPE for a multivariate process $\boldsymbol{Q}(t)$ reads

$$\frac{\partial}{\partial t} p(\boldsymbol{q},t\,|\,\boldsymbol{q}',t') = \left[-\sum_i \frac{\partial}{\partial q_i} D_i^{(1)}(\boldsymbol{q},t) + \sum_{i,j} \frac{\partial^2}{\partial q_i \partial q_j} D_{ij}^{(2)}(\boldsymbol{q},t) \right] p(\boldsymbol{q},t\,|\,\boldsymbol{q}',t') \tag{2.17}$$

Here the multivariate KM coefficients are defined by

$$D_i^{(1)}(\boldsymbol{q},t) = \lim_{\tau\to 0}\frac{1}{\tau}\langle Q_i(t+\tau) - Q_i(t)\,|\,\boldsymbol{Q}(t) = \boldsymbol{q}\rangle\,, \tag{2.18}$$

$$D_{ij}^{(2)}(\boldsymbol{q},t) = \lim_{\tau\to 0}\frac{1}{2\tau}\langle [Q_i(t+\tau) - Q_i(t)][Q_j(t+\tau) - Q_j(t)]\,|\,\boldsymbol{Q}(t) = \boldsymbol{q}\rangle\,. \tag{2.19}$$

2.4 The Langevin equation

In the previous section it was shown that a Gaussian Markov process is fully characterized by the first two KM coefficients. For these processes one can set up a dynamic evolution equation in form of a stochastic differential equation, the *Langevin equation*. Its basic form for a univariate process $Q(t)$ is [Ris89]

$$\dot{Q}(t) = h(Q(t),t) + g(Q(t),t)\Gamma(t)\,. \tag{2.20}$$

Here the function h determines the deterministic part of the dynamics, and g is the state dependent amplitude of a stochastic force Γ with $\langle\Gamma(t)\rangle = 0$. In order for the process to be Markovian, the stochastic force has to be δ-correlated,

$$\langle\Gamma(t)\Gamma(t')\rangle = \delta(t-t')\,. \tag{2.21}$$

Remembering our considerations about the drift and diffusion coefficients from Sect. 2.3, it is obvious that h and g must be connected to $D^{(1)}$ and $D^{(2)}$, respectively. One can easily show that the concrete connection is

$$D^{(1)}(q,t) = h(q,t)\,, \tag{2.22}$$

$$D^{(2)}(q,t) = \tfrac{1}{2}g^2(q,t)\,, \tag{2.23}$$

if Itô's definition of stochastic integrals is used (cf. [Ris89]). If Γ is Gaussian distributed, all KM coefficients of order three and higher vanish.

The generalization to a multivariate process $\boldsymbol{Q}(t)$ is

$$\dot{\boldsymbol{Q}}(t) = \boldsymbol{h}(\boldsymbol{Q}(t),t) + \mathbf{G}(\boldsymbol{Q}(t),t)\boldsymbol{\Gamma}(t)\,, \tag{2.24}$$

where $\boldsymbol{q}$, $\boldsymbol{h}$ and $\boldsymbol{\Gamma}$ are vectors with N components and $\mathbf{G}$ is an $N\times N$ diffusion matrix. The noise vector $\boldsymbol{\Gamma}$ now has to satisfy

$$\langle\Gamma_i(t)\Gamma_j(t')\rangle = \delta_{ij}\delta(t-t')\,, \tag{2.25}$$

where δ_{ij} denotes the Kronecker symbol. The connection to the KM coefficients is now given by

$$D_i^{(1)}(\boldsymbol{q},t) = h_i(\boldsymbol{q},t)\,, \tag{2.26}$$

$$D_{ij}^{(2)}(\boldsymbol{q},t) = \frac{1}{2}\sum_k G_{ik}(\boldsymbol{q},t)G_{jk}(\boldsymbol{q},t)\,. \tag{2.27}$$

The Langevin equation is very useful to simulate Markov processes. A numerical integration of Eq. (2.20) can be easily done using the Euler-Maruyama scheme,

$$Q_i(t+\tau) = Q_i(t) + \tau h_i(\boldsymbol{Q}(t), t) + \sqrt{\tau}\, g_{ij}(\boldsymbol{Q}(t), t)\Gamma_j(t)\,. \tag{2.28}$$

Here, $\Gamma_j(t)$ are standard normal distributed independent random variables which can be computed employing, e. g., the Box-Muller method. The accuracy of the Euler-Maruyama scheme is of order $\tau^{1/2}$. A higher order method is the Milstein scheme, which is of order τ [KP99].

2.5 Estimation of Kramers-Moyal coefficients

As was demonstrated in the previous sections, the information about the first two KM coeffcients is sufficient to set up a thorough model for a Gaussian Markov process. If appropriate data of such a process are available, it is possible to estimate these coefficients by data analysis methods. Friedrich and Peinke were the first who performed this kind of analysis, which is now termed *Kramers-Moyal analysis*, during their investigations of the turbulent cascade [FP97b, FP97a]. Later in Ref. [SFP98], Siegert, Peinke and Friedrich described the general method and pointed out its potential for other applications. Since then there have been numerous applications in the natural sciences, finance, engineering and medicine (cf. Refs. [FPST11, FPT09] for an overview).

The problem of estimating KM coefficients, Eq. (2.12), can be devided into two parts. The first part is to evaluate the conditional expectation values, which we call the *conditional moments*

$$\begin{aligned} M_\tau^{(n)}(q,t) &= \langle (Q(t+\tau) - Q(t))^n \,|\, Q(t) = q\rangle \\ &= \int_{-\infty}^{\infty} (q'-q)^n\, p\,(q', t+\tau \,|\, q, t)\, \mathrm{d}q'\,. \end{aligned} \tag{2.29}$$

This is a regression problem well known in statistics. A common method to solve this regression problem will be presented in Sect. 3.2. However, the conditional moments can only be estimated for finite values of the time increment τ. The smallest τ for which the conditional moments can be estimated is given by the sampling interval of the available time series data. Therefore, the second problem is to perform or approximate the limit

$$\lim_{\tau\to 0} \frac{1}{n!\tau} M_\tau^{(n)}(q,t)\,. \tag{2.30}$$

In the first applications of the KM analysis, researchers were predominantly interested in qualitative models and put not much emphasis on the quantitative accuracy of the estimated KM coefficients. Therefore the regression problem was solved by simple histogram-based regression and not much attention was paid to the limiting process.

Regarding the regression problem, a first improvement was achieved by Lamouroux and Lehnertz who employed a kernel-based regression technique to estimate the conditional moments [LL09]. Ragwitz and Kantz were the first who pointed out the importance of the limiting problem. Based on the short time propagator, Eq. (2.16), they provided correction terms for the estimation of the diffusion coefficient at a finite sampling interval. But, as was pointed out in Ref. [FRSP02], the short time propagator can deviate from Eq. (2.16) for a finite time increment. Therefore, the corrections presented by Ragwitz and Kantz are not correct. However, as we will demonstrate in Chap. 4, the conditional moments can be expressed as an infinite series expansion in the time increment τ (cf. Eq. (4.10)). From this series expansion one can construct correction terms of arbitrary order in τ [FRSP02]. However, higher order correction terms soon become very cumbersome, and the question about which correction order is necessary has not been answered.

Another way to perform the KM analysis is to make a parametric ansatz for $D^{(1)}$ and $D^{(2)}$ and to optimize the free parameters on some observable quantities. The first method of this kind was introduced by Kleinhans *et al.* [KFNP05, KF07]. In this method the free parameters are iterated until the conditional PDF of some fixed time increment of the corresponding model is in optimal agreement to the corresponding conditional PDF estimated from the available time series data. This method also allows for correct results if the sampling interval of the time series data is large. However, we cannot expect the reconstruction method of Refs. [KFNP05, KF07] to work for arbitrary large sampling intervals because at some point the information about the dynamics is lost, and two successive measurements become uncorrelated.

In Chap. 4 the problem of the KM analysis for data sets with large sampling intervals is analyzed in further detail. The question, under which conditions a reliable estimation is possible, is discussed, and another optimization method, which has some advantages over the method of Refs. [KFNP05, KF07], is introduced. In Chap. 5 an application of this method to experimental data of an optical trapping experiment is presented. A conclusion is presented in Chap. 6.

Another problem related to the KM analysis that is not addressed here is measurement noise. An analysis method that regards this problem is presented in [Leh11, Leh13].

Finally it should be stressed that the KM analysis is only suggestive for Gaussian Markov processes. Therefore, a reliable analysis should contain a test of the Markov property and a test, whether or not the third and higher KM coefficients vanish in order to ensure the Gaussianity. Both tests are explained and performed in the course of the analysis of Chap. 5.

3 Data analysis techniques

The scope of this chapter is to introduce some computational data analysis techniques that will be employed in Chaps. 4 and 5. The first section is devoted to kernel density estimation, a method to estimate probability densities from random samples. Subsequently, kernel regression will be introduced in Sect. 3.2.

For a more comprehensive discussion about kernel density estimation and kernel regression, the reader is referred to Ref. [HMSW04].

3.1 Kernel density estimation

The PDF $f_Q(x)$ of a stochastic variable Q can be defined as the expectation value of the Dirac δ function

$$f_Q(x) = \langle \delta(x - Q) \rangle \,, \tag{3.1}$$

where $\delta(x - Q)$ is also called the *fine grained PDF*. For a set of observations $Q_1, \ldots, Q_N$ an estimator for the expectation value of a function $g(Q)$ is

$$\widehat{\langle g(Q) \rangle} = \frac{1}{N} \sum_{i=1}^{N} g(Q_i) \,, \tag{3.2}$$

where here and in the following, a hat above a symbol denotes an estimator for the corresponding object. Therefore, a natural estimate for the PDF of the variable Q would be

$$\hat{f}_Q(x) = \frac{1}{N} \sum_{i=1}^{N} \delta(x - Q_i) \,. \tag{3.3}$$

In the limit $N \to \infty$ this will yield the correct PDF, but for finite N this estimator will not be of much use. To improve our estimator, we define a function $K(x)$, such that

$$\int K(x) \mathrm{d}x = 1 \tag{3.4}$$

and

$$\lim_{h\to 0} \frac{1}{h} K(x/h) = \delta(x) \tag{3.5}$$

and define

$$\hat{f}_Q(x) = \frac{1}{N} \sum_{i=1}^{N} \frac{1}{h} K\left(\frac{x - Q_i}{h}\right) . \tag{3.6}$$

This estimator converges to the true PDF in the limit $N \to \infty,\ h \to 0$. The function $K(x)$ is called a *kernel* and Eq. (3.6) is the definition of the *kernel density estimator*. Kernel functions are usually even, i. e.,

$$K(x) = K(-x) , \tag{3.7}$$

and positive, $K(x) \geq 0\ \forall x$. Table 3.1 shows examples of common kernel functions that satisfy these conditions together with (3.4) and (3.5). Here, we have used the definition

$$I(|x| < 1) = \begin{cases} 1 & \text{for } |x| < 1 \\ 0 & \text{else} \end{cases} . \tag{3.8}$$

The functions listed in Tab. 3.1 are plotted in Fig. 3.1.

Tab. 3.1 Frequently used kernel functions.

Kernel	$K(x)$
Uniform[a]	$\frac{1}{2}\ I(\lvert x\rvert < 1)$
Epanechnikov[a]	$\frac{3}{4}(1 - x^2)\ I(\lvert x\rvert < 1)$
Quartic[a]	$\frac{15}{16}(1 - x^2)^2\ I(\lvert x\rvert < 1)$
Gauß	$\frac{1}{\sqrt{2\pi}} \exp\left(-\frac{1}{2}x^2\right)$

[a] $I(|x| < 1)$ is defined in Eq. (3.8)

A specific kernel density estimate of a given random sample depends on the selected kernel function and on the coefficient h that is called the *bandwidth*. Since the selection of the bandwidth turns out to be the most important issue [HMSW04], we label a specific kernel density estimate with $\hat{f}_h(x)$ and skip the name of the stochastic variable. To assess the quality of an estimate, two quantities, the *bias* and the *variance* are important and will be introduced in the following.

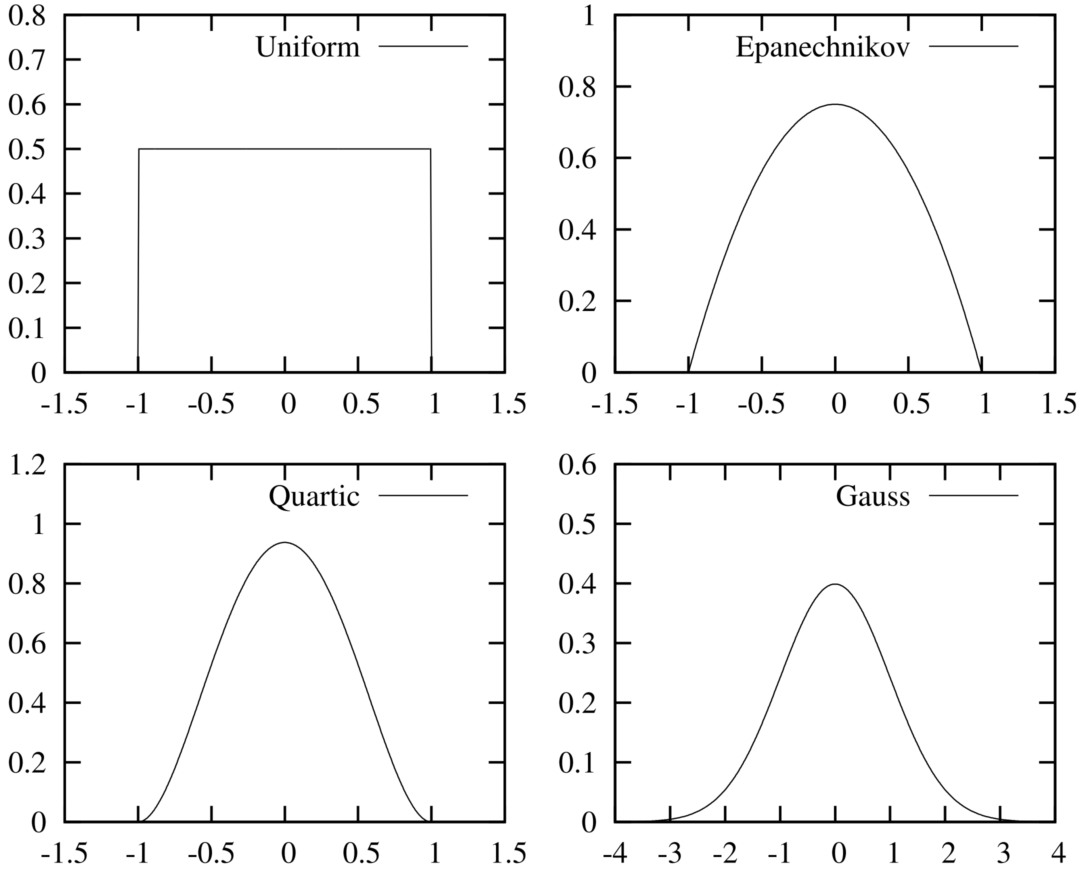

Fig. 3.1 Frequently used kernel functions corresponding to Tab. 3.1.

3.1.1 Bias and variance

The discussion in the remaining sections of this chapter follows the presentation of Ref. [HMSW04].

An estimator is said to be *unbiased* if the expectation value of the estimator equals the quantity that it is supposed to estimate. Otherwise it has a specific *bias* which is defined as the difference between the expectation value of the estimator and the quantity it is supposed to estimate and can be understood as a *systematic* error. As we have already seen, the kernel density estimator is unbiased if the bandwidth is zero. For a finite bandwidth it has the finite bias

$$\begin{aligned}
\mathrm{Bias}\left\{\hat{f}_h(x)\right\} &= \left\langle \hat{f}_h(x) \right\rangle - f(x) &(3.9)\\
&= \frac{1}{N}\sum_{i=1}^{N}\left\langle \frac{1}{h}K\left(\frac{x-Q_i}{h}\right)\right\rangle - f(x)\,. &(3.10)
\end{aligned}$$

Since we assume that all Q_i are drawn from the same distribution $f(x)$, $\langle g(Q_i)\rangle = \langle g(Q)\rangle$. Hence,

$$\begin{aligned}\mathrm{Bias}\left\{\hat{f}_h(x)\right\} &= \left\langle \frac{1}{h}K\left(\frac{x-Q}{h}\right)\right\rangle - f(x)\\ &= \int \frac{1}{h}K\left(\frac{x-y}{h}\right)f(y)\mathrm{d}y - f(x)\\ &= \int K(s)f(x+hs)\mathrm{d}s - f(x)\,. \end{aligned} \tag{3.11}$$

In the last expression we have introduced the variable $s = \frac{y-x}{h}$ and used Eq. (3.7). Expanding $f(x+sh)$ up to second order in h yields

$$\begin{aligned}\mathrm{Bias}\left\{\hat{f}_h(x)\right\} =& f(x)\underbrace{\int K(s)\mathrm{d}s}_{=1} + hf'(x)\underbrace{\int sK(s)\mathrm{d}s}_{=0}\\ &+ \frac{1}{2}h^2 f''(x)\underbrace{\int s^2K(s)\mathrm{d}s}_{=\mu_2(K)} - f(x) + O(h^3)\,. \end{aligned} \tag{3.12}$$

The first integral equals one because of Eq. (3.4), and the second integral vanishes due to Eq. (3.7). Therefore, for small h the bias can written as

$$\mathrm{Bias}\left\{\hat{f}_h(x)\right\} = \frac{h^2}{2}f''(x)\mu_2(K) + O(h^3)\,, \tag{3.13}$$

with $\mu_2(K) = \int x^2K(x)\mathrm{d}x$. We see that the bias grows quadratically with the bandwidth and depends linearly on the curvature of the true PDF.

The second important quantity of an estimator is the *variance* which describes the expected fluctuations around the expected value of an estimator. The variance of the kernel density estimator is

$$\mathrm{Var}\left\{\hat{f}_h(x)\right\} = \left\langle \hat{f}_h^2(x)\right\rangle - \left\langle \hat{f}_h(x)\right\rangle^2\,, \tag{3.14}$$

which can be shown to equal

$$\frac{1}{N}\mathrm{Var}\left\{\frac{1}{h}K\left(\frac{x-Q}{h}\right)\right\}\,. \tag{3.15}$$

For a small bandwidth h the leading term is [HMSW04]

$$\mathrm{Var}\left\{\hat{f}_h(x)\right\} \simeq \frac{1}{Nh}f(x)||K||_2^2\,, \tag{3.16}$$

with $||K||_2^2 = \int \mathrm{d}xK^2(x)$. Therefore a small bandwidth leads to a large variance and vice versa.

3.1.2 Bandwidth selection

We have seen that a large bandwidth leads to a low variance, but also results in a large bias and vice versa. An optimal bandwidth should therefore represent a tradeoff between both effects. This also becomes clear if we consider the *mean squared error*

$$\mathrm{MSE}\left\{\hat{f}_h(x)\right\} = \left\langle \left[\hat{f}_h(x) - f(x)\right]^2 \right\rangle . \tag{3.17}$$

It can easily be shown that the MSE is the sum of the variance and the squared bias,

$$\mathrm{MSE}\left\{\hat{f}_h(x)\right\} = \mathrm{Var}\left\{\hat{f}_h(x)\right\} + \left[\mathrm{Bias}\left\{\hat{f}_h(x)\right\}\right]^2 , \tag{3.18}$$

if one uses the definitions of bias and variance, Eqs. (3.9) and (3.14), respectively. Therefore, as a criterion for an optimal bandwidth we can use the postulation that the MSE is minimal. Using our series expansions (3.13) and (3.16), we obtain

$$\mathrm{MSE}\left\{\hat{f}_h(x)\right\} \simeq \frac{1}{Nh} f(x) \|K\|_2^2 + \frac{h^4}{4} f''(x)^2 \mu_2(K)^2 . \tag{3.19}$$

The only problem is that the MSE depends on x. To obtain a global optimal bandwidth, one can regard the *mean integrated squared error* (MISE) instead of the MSE. The former is defined as

$$\mathrm{MISE}\left\{\hat{f}_h\right\} = \int \mathrm{MSE}\left\{\hat{f}_h(x)\right\} \mathrm{d}x \tag{3.20}$$

If we insert the approximation (3.19), we obtain the *approximate mean integrated squared error* (AMISE)

$$\mathrm{AMISE}\left\{\hat{f}_h\right\} = \frac{1}{Nh} \|K\|_2^2 + \frac{h^4}{4} \|f''\|_2^2 \mu_2(K)^2 . \tag{3.21}$$

From this expression, one can compute the minimum with respect to h, yielding

$$h_{\mathrm{opt}} = \left(\frac{\|K\|_2^2}{\|f''\|_2^2 \mu_2(K)^2 N} \right)^{1/5} . \tag{3.22}$$

The problem with this formula is of course, that it depends on $\|f''\|_2^2$ while $f(x)$ is the unknown quantity we try to estimate. However, one can obtain a *rule-of-thumb* bandwidth by assuming a specific class of distributions. For a Gaussian PDF with variance σ^2 for instance, one obtains

$$\|f''\|_2^2 = \frac{3}{8\sqrt{\pi}} \sigma^{-5} \approx 0.212 \sigma^{-5} . \tag{3.23}$$

The standard deviation can be estimated by

$$\hat{\sigma} = \sqrt{\frac{1}{N-1}\sum_{i=1}^{N}(\langle Q\rangle - Q_i)^2}\,. \tag{3.24}$$

For the Gaussian kernel $K(x) = \frac{1}{\sqrt{2\pi}}\exp\left(-\frac{1}{2}x^2\right)$, we have

$$\left(\frac{\|K\|_2^2}{\mu_2^2(K)}\right)^{1/5} = \left(\frac{1}{4\pi}\right)^{1/10} \approx 0.776\,, \tag{3.25}$$

which results in

$$h_{\mathrm{opt}} \approx 1.06\hat{\sigma}N^{-1/5}\,. \tag{3.26}$$

The last expression is the famous *Silverman's rule of thumb* (SRT). If we introduce the coefficient

$$\delta_0(K) = \left(\frac{\|K\|_2^2}{\mu_2^2(K)}\right)^{1/5}\,, \tag{3.27}$$

we can generalize SRT to

$$h_{\mathrm{opt}} \approx 1.364\,\delta_0(K)\hat{\sigma}N^{-1/5}\,. \tag{3.28}$$

During the analyses presented in this thesis, the Epanechnikov kernel scaled in a way that $\mu_2(K) = 1$ is used. It reads

$$K(x) = \frac{3\sqrt{5}}{100}\left(5 - x^2\right) I\left(|x| < \sqrt{5}\right)\,. \tag{3.29}$$

For this kernel, the rule-of-thumb bandwidth is given by

$$h_{\mathrm{opt}} \approx 1.048\hat{\sigma}N^{-1/5}\,. \tag{3.30}$$

The Epanechnikov kernel is employed because it leads to continuous and (at least piecewise) differentiable estimates and is numerically cheaper than other kernels that have this property.

3.1.3 Multivariate kernel density estimation

The natural extension of the kernel density estimator, Eq. (3.6), for a multivariate stochastic variable $\boldsymbol{Q} = (Q^1, \ldots, Q^d)^T$ is the product kernel estimator

$$\hat{f}_{\boldsymbol{Q}}(\boldsymbol{x}) = \frac{1}{N\prod_{k=1}^{d} h_k}\sum_{i=1}^{N}\prod_{j=1}^{d} K\left(\frac{x_j - Q_i^j}{h_j}\right)\,. \tag{3.31}$$

Now we have a specific bandwidth h_j for each component of $\boldsymbol{Q}$. In analogy to Eq. (3.28) there is also a rule of thumb for the optimal bandwidths [HMSW04],

$$h_{j,\mathrm{opt}} \approx \hat{\sigma}_j N^{-1/(d+4)} , \tag{3.32}$$

where $\hat{\sigma}_j$ is the standard deviation estimator of jth component of $\boldsymbol{Q}$. Here, a constant prefactor is omitted because it is close to one anyway, and aspirations for high accuracy in multivariate density estimation cannot be satisfied in most practical cases.

In many cases it is not suggestive to assign a bandwidth to each component. This is when the cloud of data points has minimal and maximal widths that are not aligned with the coordinate axes. In mathematical terms that means that the eigenvectors of the covariance matrix are not parallel to the coordinate axes. In those cases, an improvement of (3.31) is [HMSW04]

$$\hat{f}_{\boldsymbol{Q}}(\boldsymbol{x}) = \frac{1}{N \det \mathbf{H}} \sum_{i=1}^{N} \mathcal{K}\{\mathbf{H}^{-1}(\boldsymbol{x} - \boldsymbol{Q}_i)\} \tag{3.33}$$

with

$$\mathcal{K}\{\mathbf{H}^{-1}(\boldsymbol{x} - \boldsymbol{Q})\} = \prod_{j=1}^{d} K\{[\mathbf{H}^{-1}(\boldsymbol{x} - \boldsymbol{Q})]_j\} , \tag{3.34}$$

where $\mathbf{H}$ is the bandwidth matrix. A rule-of-thumb bandwidth matrix can be constructed from an estimated covariance matrix $\hat{\boldsymbol{\Sigma}}$ with

$$\hat{\Sigma}_{ij} = \langle (Q_i - \bar{Q}_i)(Q_j - \bar{Q}_j) \rangle . \tag{3.35}$$

Then, an optimal bandwidth matrix can be approximated by [HMSW04],

$$\mathbf{H}_{\mathrm{opt}} \approx \hat{\boldsymbol{\Sigma}}^{1/2} N^{-1/(d+4)} . \tag{3.36}$$

To compute $\hat{\boldsymbol{\Sigma}}^{1/2}$, one has to diagonalize $\hat{\boldsymbol{\Sigma}}$,

$$\hat{\boldsymbol{\Sigma}} = \mathbf{Q}\mathbf{D}_{\Sigma}\mathbf{Q}^{-1} \tag{3.37}$$

$$= \mathbf{Q}\mathbf{D}_{\Sigma}^{1/2}\mathbf{Q}^{-1}\mathbf{Q}\mathbf{D}_{\Sigma}^{1/2}\mathbf{Q}^{-1} . \tag{3.38}$$

Then we have

$$\hat{\boldsymbol{\Sigma}}^{1/2} = \mathbf{Q}\mathbf{D}_{\Sigma}^{1/2}\mathbf{Q}^{-1} , \tag{3.39}$$

where $\mathbf{D}_{\Sigma}^{1/2}$ is a diagonal matrix whose entries are the square roots of the (real and positive) eigenvalues of $\hat{\boldsymbol{\Sigma}}$, and $\mathbf{Q}$ and $\mathbf{Q}^{-1}$ are the transition matrices that are built from the eigenvectors of $\hat{\boldsymbol{\Sigma}}$.

3.2 Kernel regression

The most frequently used kernel-based estimator for conditional expectation values is the *Nadaraya-Watson estimator*. This estimator will be used in later analyses to estimate the conditional moments (2.29). In order to derive the Nadaraya-Watson estimator, we consider two random variables X and Y with a joint PDF $f(x, y)$. We assume that we have a random sample of pairs (X_i, Y_i), $i = 1, \ldots, N$ that were drawn independently from the joint distribution. Now the goal is to estimate the conditional expectation value

$$m(x) = \langle Y \,|\, X = x \rangle = \int y \, p(y \,|\, x) \, \mathrm{d}y = \frac{\int y f(x, y) \mathrm{d}y}{f_X(x)} \, . \tag{3.40}$$

To estimate the joint PDF $f(x, y)$, we employ the product kernel estimator introduced in the previous section,

$$\hat{f}(x, y) = \frac{1}{N h_x h_y} \sum_{i=1}^{N} K\left(\frac{x - X_i}{h_x}\right) K\left(\frac{y - Y_i}{h_y}\right) . \tag{3.41}$$

Then we obtain for the numerator of Eq. (3.40)

$$\int y \hat{f}(x, y) \mathrm{d}y = \frac{1}{N h_x} \sum_{i=1}^{N} K\left(\frac{x - X_i}{h_x}\right) \int \frac{y}{h_y} K\left(\frac{y - Y_i}{h_y}\right) \mathrm{d}y \, . \tag{3.42}$$

For the last integral we introduce the variable $s = \frac{y - Y_i}{h_y}$, which leads to

$$K\left(\frac{y - Y_i}{h_y}\right) \mathrm{d}y = \int (h_y s + Y_i) K(s) \mathrm{d}s \tag{3.43}$$

$$= h_y \underbrace{\int s K(s) \mathrm{d}s}_{=0} + Y_i \underbrace{\int K(s) \mathrm{d}s}_{=1} \tag{3.44}$$

$$= Y_i \tag{3.45}$$

To evaluate the integrals in Eq. (3.44), Eqs. (3.7) and (3.4) have been used. If we plug Eqs. (3.45) and (3.42) into Eq. (3.40), and use the standard univariate kernel estimator (3.6), we obtain the Nadaraya-Watson estimator

$$\hat{m}(x) = \frac{\sum_{i=1}^{N} K\left(\frac{x - X_i}{h_x}\right) Y_i}{\sum_{j=1}^{N} K\left(\frac{x - X_j}{h_x}\right)} \, . \tag{3.46}$$

Just as the kernel estimator for the density estimation problem, also the Nadaraya-Watson estimator depends on a bandwidth. A large (small) bandwidth will decrease (increase) the variance, but increase (decrease) the bias of the estimation. In contrast to the density estimation problem, one cannot derive an easy rule-of-thumb bandwidth for the regression problem. One possibility to compute an optimal bandwidth is the cross-validation algorithm [HMSW04]. The problem with cross-validation is that it is computationally very demanding for large data sets because one has to minimize a function that consists of order N^2 summands, where N is size of the data sample. However, to estimate the conditional moments (2.29), one can yield satisfying results by using the same rule-of-thumb bandwidth as for the density estimation problem. This is on the one hand reasonable because in the derivation of the Nadaraya-Watson estimator, h_x is the bandwidth with which the univariate PDF of X is estimated in the denominator. On the other hand, the bias of the Nadaraya-Watson estimator crucially depends on the derivatives of the desired function $m(x)$, which should influence the choice of the bandwidth. Since a large bandwidth leads to systematically underestimated slopes and curvatures of the function $m(x)$, often the prefactor of Eq. (3.30) is reduced to 0.8 in the analyses presented in this thesis.

To estimate the components of a drift vector (2.18) or a diffusion matrix (2.19) of multivariate process, one needs to determine conditional expectation values, where the random variable $\boldsymbol{X}$ is multivariate,

$$m(\boldsymbol{x}) = \langle Y | \boldsymbol{X} = \boldsymbol{x} \rangle \, . \tag{3.47}$$

Employing the multivariate kernel density estimator (3.33), one can derive the multivariate Nadaraya-Watson estimator

$$\hat{m}(\boldsymbol{x}) = \frac{\sum_{i=1}^{N} \mathcal{K}\{\mathbf{H}^{-1}(\boldsymbol{x} - \boldsymbol{X}_i)\} Y_i}{\sum_{j=1}^{N} \mathcal{K}\{\mathbf{H}^{-1}(\boldsymbol{x} - \boldsymbol{X}_j)\}} \, . \tag{3.48}$$

The Nadaraya-Watson estimator is used in the KM analysis method presented in Chap. 4. A more sophisticated method is local polynomial regression [HMSW04]. This method can significantly reduce bias and variance. Therefore, employing the local polynomial regression method may improve the KM analysis method presented in this thesis.

4 Kramers-Moyal analysis for sparsely sampled time series data

A frequently arising problem in the estimation of drift and diffusion from “real world” time series data consists in a low sampling rate at which the data were recorded. In this case, it is not trivial to perform the limit $\tau \to 0$ in Eq. (2.12). In a naive estimation that ignores the limiting process and just evaluates the conditional moments for the smallest available time increment τ, i. e., the sampling interval of the time series data, dramatic deviations from the true coefficients can occur. Even if one applies low order corrections, the results can be very misleading. The errors that originate in a large sampling interval are referred to as *finite time* or *finite sampling interval effects* in the literature. In a paper from 2009, Lade presents a method that allows one to make exact predictions of finite time effects for arbitrary drift and diffusion coefficients [Lad09]. Within the framework of the current thesis, the inverse problem was solved, namely the deduction of the true drift and diffusion coefficients from estimated finite time coefficients. This method, which is published in Refs. [HF11, HFHD12], is the subject of the present chapter.

The first section of this chapter reviews Lade’s method to predict finite time effects and gives some examples of how these effects can look like. It will be shown that there are two regimes in the time increment τ separated by the relaxation time τ_R. In the regime $\tau \ll \tau_R$ the treatment of finite time effects is not necessary, in the regime $\tau \gg \tau_R$ it is not possible, because the information of the dynamics is lost. The new method is well suited for cases where the sampling interval is approximately of the same order of magnitude as the relaxation time.

In the next sections the method is described, and examples for its functionality are presented. The last section provides some remarks on the numerical integration of the adjoint FPE, which has to be performed in the course of the optimization if no analytical solutions are available.

4.1 Finite time effects

We define the finite time KM coefficients as

$$D_\tau^{(n)}(x) = \frac{1}{n!\tau} M_\tau^{(n)}(x) \tag{4.1}$$

with

$$\begin{aligned} M_\tau^{(n)}(x) &= \langle [X(t+\tau) - X(t)]^n \rangle|_{X(t)=x} &(4.2)\\ &= \int\limits_{-\infty}^{\infty} (x'-x)^n \, p\,(x', t+\tau|x, t)\,\mathrm{d}x' \,. &(4.3) \end{aligned}$$

Thus,

$$\lim_{\tau\to 0} D_\tau^{(n)}(x) = D^{(n)}(x)\,. \tag{4.4}$$

As we have seen in Sect. 2.3, the conditional PDF $p\,(x', t+\tau|x, t)$ is the solution of the FPE at time $t' = t + \tau$ with the initial condition $f\,(x', t' = t) = \delta\,(x' - x)$. Therefore, it can be written as

$$p\,(x', t+\tau|x, t) = \mathrm{e}^{\hat{L}(x')\tau}\delta(x'-x)\,, \tag{4.5}$$

where $\hat{L}(x')$ is the Fokker-Planck operator

$$\hat{L}(x') = -\frac{\partial}{\partial x'} D^{(1)}(x') + \frac{\partial^2}{\partial x'^2} D^{(2)}(x')\,. \tag{4.6}$$

Inserting Eq. (4.5) into (4.3), one obtains

$$M_\tau^{(n)}(x) = \int\limits_{-\infty}^{\infty} (x'-x)^n \, \mathrm{e}^{\hat{L}(x')\tau}\delta(x'-x)\mathrm{d}x' \,. \tag{4.7}$$

If we define the inner product $\langle f|g\rangle = \int f(x)g(x)\mathrm{d}x$, Eq. (4.7) can be written as

$$\begin{aligned} M_\tau^{(n)}(x) &= \left\langle (x'-x)^n \middle| \mathrm{e}^{\hat{L}(x')\tau}\delta(x'-x) \right\rangle \\ &= \left\langle \mathrm{e}^{\hat{L}^\dagger(x')\tau} (x'-x)^n \middle| \delta(x'-x) \right\rangle \\ &= \mathrm{e}^{\hat{L}^\dagger(x')\tau} (x'-x)^n \Big|_{x'=x} \,. &(4.8) \end{aligned}$$

In the second step we have introduced the adjoint Fokker-Planck operator

$$\hat{L}^\dagger(x') = D^{(1)}(x')\frac{\partial}{\partial x'} + D^{(2)}(x')\frac{\partial^2}{\partial x'^2}\,. \tag{4.9}$$

The propagator $\mathrm{e}^{\hat{L}^\dagger(x')\tau}$ in Eq. (4.8) can be expanded into a power series of $\hat{L}^\dagger(x')\tau$, which leads to

$$M_\tau^{(n)}(x) = \left[\sum_{k=0}^{\infty} \frac{\left(\hat{L}^\dagger(x')\right)^k \tau^k}{k!} (x' - x)^n \right] \Bigg|_{x'=x} . \tag{4.10}$$

Equation (4.10) was already stated in [FRSP02]. The central point in Lade's article [Lad09] is a reinterpretation of Eq. (4.8). Namely, the term $\mathrm{e}^{\hat{L}^\dagger(x')\tau}$ can be understood as the propagator of the PDE

$$\frac{\partial W_{n,x}(x',t)}{\partial t} = \hat{L}^\dagger(x') W_{n,x}(x',t) , \tag{4.11}$$

which acts on the initial condition

$$W_{n,x}(x',0) = (x' - x)^n . \tag{4.12}$$

Thus, the conditional moments are given by

$$M_\tau^{(n)}(x) = W_{n,x}(x' = x, t = \tau) . \tag{4.13}$$

The indices n and x of the function W shall emphasize that Eq. (4.11) has to be solved with the initial condition (4.12), which depends on n and x, to obtain the nth moment at position x. Lade calls Eq. (4.11) the *adjoint Fokker-Planck equation* (AFPE)[1].

The advantage of this interpretation over the series expansion (4.10) lies in the fact that the conditional moments can be calculated exactly or at least up to numerical accuracy. On the contrary, the usage of the series expansion is connected to the problem that one does not know in advance how many terms are necessary. This would make an inversion quite intricate. Section 4.8 deals with the numerical integration of the AFPE.

4.1.1 Examples

For simple drift and diffusion coefficients, Eq. (4.11) can be solved analytically. For a linear drift $D^{(1)}(x) = -\gamma x$ and quadratic diffusion $D^{(2)}(x) = \alpha + \beta x^2$, one obtains for $n = 1$

$$W_{1,x}(x',t) = x'\mathrm{e}^{-\gamma t} - x . \tag{4.14}$$

This leads to

$$\begin{aligned} D_\tau^{(1)}(x) &= \frac{1}{\tau} W_{1,x}(x' = x, t = \tau) \\ &= -\frac{x}{\tau}\left(1 - \mathrm{e}^{-\gamma\tau}\right) . \end{aligned} \tag{4.15}$$

---

[1] It differs from the backward Kolmogorov equation which has a negative sign in front of one side of the equation.

For $n = 2$ we get

$$W_{2,x}(x', t) = x^2 - \frac{\alpha}{\beta - \gamma}\left(1 - \mathrm{e}^{2(\beta-\gamma)t}\right) + x'^2 \mathrm{e}^{2(\beta-\gamma)t} - 2xx'\mathrm{e}^{-\gamma t}, \tag{4.16}$$

which yields

$$\begin{aligned} D_\tau^{(2)}(x) &= \frac{1}{2\tau} W_{2,x}(x' = x, t = \tau) \\ &= \frac{1}{2\tau}\left[x^2\left(1 + \mathrm{e}^{2(\beta-\gamma)\tau} - 2\mathrm{e}^{-\gamma\tau}\right) - \frac{\alpha}{\beta-\gamma}\left(1 - \mathrm{e}^{2(\beta-\gamma)\tau}\right)\right]. \end{aligned} \tag{4.17}$$

For $\beta = 0$ we obtain the corresponding result for an Ornstein-Uhlenbeck (OU) process,

$$D_\tau^{(2)}(x) = \frac{1}{2\tau}\left[x^2\left(1 - \mathrm{e}^{-\gamma\tau}\right)^2 + \frac{\alpha}{\gamma}\left(1 - \mathrm{e}^{-2\gamma\tau}\right)\right]. \tag{4.18}$$

The finite time drift for the OU process is the same as Eq. (4.15).

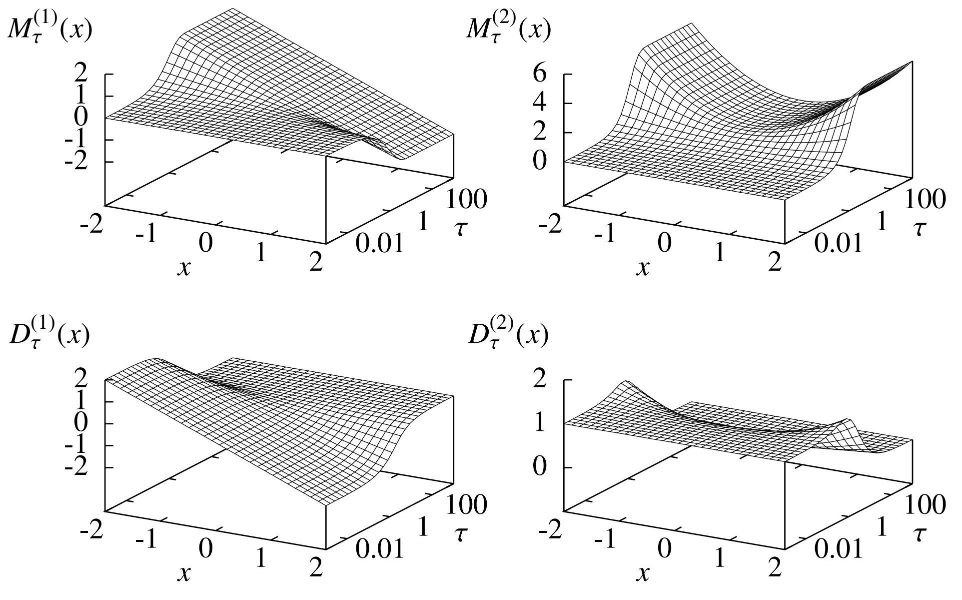

Fig. 4.1 Conditional moments (top) and finite time drift and diffusion coefficients (bottom) for an OU process with $D^{(1)} = -x$ and $D^{(2)} = 1$. The τ axes are in logarithmic scaling. The relaxation time for this process is $\tau_R = 1$. For $\tau \ll \tau_R$, the finite time KM coefficients have converged to the true KM coefficients, whereas the conditional moments vanish. For $\tau \gg \tau_R$, the conditional moments become stationary, whereas the corresponding KM coefficients vanish.

Figure 4.1 shows the finite time drift and diffusion and the corresponding conditional moments for the latter process with $\gamma = \alpha = 1$. As one can clearly see, the relaxation time $\tau_R = 1$ separates two different regimes. In the regime $\tau \ll \tau_R$, the finite time KM coefficients have converged to the true coefficients. Finite time effects can be safely neglected in this case. In the regime $\tau \gg \tau_R$, the first conditional moment becomes linear in x and the second moment becomes quadratic. Both moments become constant with respect to τ. The corresponding KM coefficients have the same dependence on x but, according to Eq. (4.1), decay to zero with τ^{-1}.

As we will see in the next subsection, the behavior in the latter regime is the same for all different kinds of drift and diffusion coefficients, provided that the first two moments of the stationary solution of the corresponding FPE exists. Therefore, any information about the true KM coefficients is lost if one has only access to this regime. A KM analysis is impossible in this case.

4.1.2 Limiting case of statistical independence

Linear drift and quadratic diffusion are the most frequently observed types of KM coefficients in real world time series (see e. g. [FPR00, Sur02, JFG+03, TM04, GPST05, SJA+05, GPTS06, GSPT06, GBSM+06, SP06, TGP+06, FEB+07, CRA07, CAR08, LPF+10, KMKT11]). In this subsection, it shall be shown that such results have to be interpreted with care since this is what one observes if the limit of statistical independence is approached where all information about the true KM coefficients is lost. Especially the diffusion coefficient often appears to be quadratic although it is constant, even if the sampling interval is lower than the relaxation time of the process (cf. examples of Fig. 4.3).

This is the case if the time increment τ is large compared to the relaxation time τ_R of the process, so that the events x at time t and x' at time $t + \tau$ become statistically independent, i. e.,

$$p(x', t + \tau | x, t) \approx f(x', t + \tau) \, . \tag{4.19}$$

As was pointed out in [AQ10], the nth finite time KM coefficient becomes a polynomial of degree n in this case:

$$\begin{aligned} M_\tau^{(n)}(x) &= \int_{-\infty}^{\infty} (x' - x)^n \, p\,(x', t + \tau | x, t) \, \mathrm{d}x' \\ &\xrightarrow{\tau \gg \tau_R} \int_{-\infty}^{\infty} (x' - x)^n \, f(x', t + \tau) \mathrm{d}x' \, . \end{aligned} \tag{4.20}$$

Apparently, the last term is an n-order polynomial in x. For a stationary process, f does not depend on time. In this case, the first two conditional moments yield

$$M^{(1)}_{\tau \gg \tau_R}(x) = \langle X \rangle - x \,, \tag{4.21a}$$

$$M^{(2)}_{\tau \gg \tau_R}(x) = \langle X^2 \rangle - 2\langle X \rangle x + x^2 \,. \tag{4.21b}$$

With Eq. (4.1), the finite time KM coefficients become

$$D^{(1)}_{\tau \gg \tau_R}(x) = \frac{1}{\tau} \left[\langle X \rangle - x \right] \,, \tag{4.22a}$$

$$D^{(2)}_{\tau \gg \tau_R}(x) = \frac{1}{2\tau} \left[\langle X^2 \rangle - 2\langle X \rangle x + x^2 \right] . \tag{4.22b}$$

If the observed conditional moments or finite time coefficients are close to (4.21) or (4.22), respectively, for all available τ, one has to admit that the KM analysis is not possible.

Of course, Eqs. (4.21) and (4.22) are only valid if the first and second moment of the stationary PDF $f(x)$ exist. For example, for a process with $D^{(1)}(x) = -\gamma x$ and $D^{(2)}(x) = \alpha + \beta x^2$, which was discussed in Sect. 4.1.1, the second moment does not exist for $\beta \geq \gamma$ as is shown in Appendix A. Therefore, the finite time diffusion, Eq. (4.17), diverges in this case as τ goes to infinity.

4.1.3 Recommended preinvestigations

The reader should now be convinced that it is important to know whether or not the sampling interval of a given data set is sufficient before one performs a KM analysis. The easiest way to get a feeling for that is to take a look at the autocorrelation function (ACF)

$$C(\tau) = \frac{\langle X(t)X(t+\tau) \rangle_t}{\langle (X(t))^2 \rangle_t} \,. \tag{4.23}$$

To demonstrate this, we consider an OU process with $D^{(1)} = -x$ and $D^{(2)} = 1$, which has a relaxation time $\tau_R = 1$. Employing the Euler-Maruyama scheme, we produce three different synthetic time series with sampling intervals $\tau_s = 0.1, 1, 10$ and 10^5 data points each. For each data set the ACF (see Fig. 4.2) and the finite time drift and diffusion coefficients $D^{(1,2)}_{\tau_s}$ (see Fig. 4.3) are determined. For $\tau_s = 0.1$ the ACF is resolved well; the correlation between two successive measurements is large ($C(\tau_s) > 0.9$). In this case, finite time effects are small, but the diffusion term already appears quadratic (cf. top panels of Fig. 4.3). For $\tau_s = 1.0$ the ACF is not resolved well, but it is still possible to estimate the relaxation time from it. Here, finite time effects are large (cf. middle panels of Fig. 4.3), but, as we will see in Sect. 4.4.1, a reconstruction of the true KM coefficients is still possible since two successive measurements are correlated

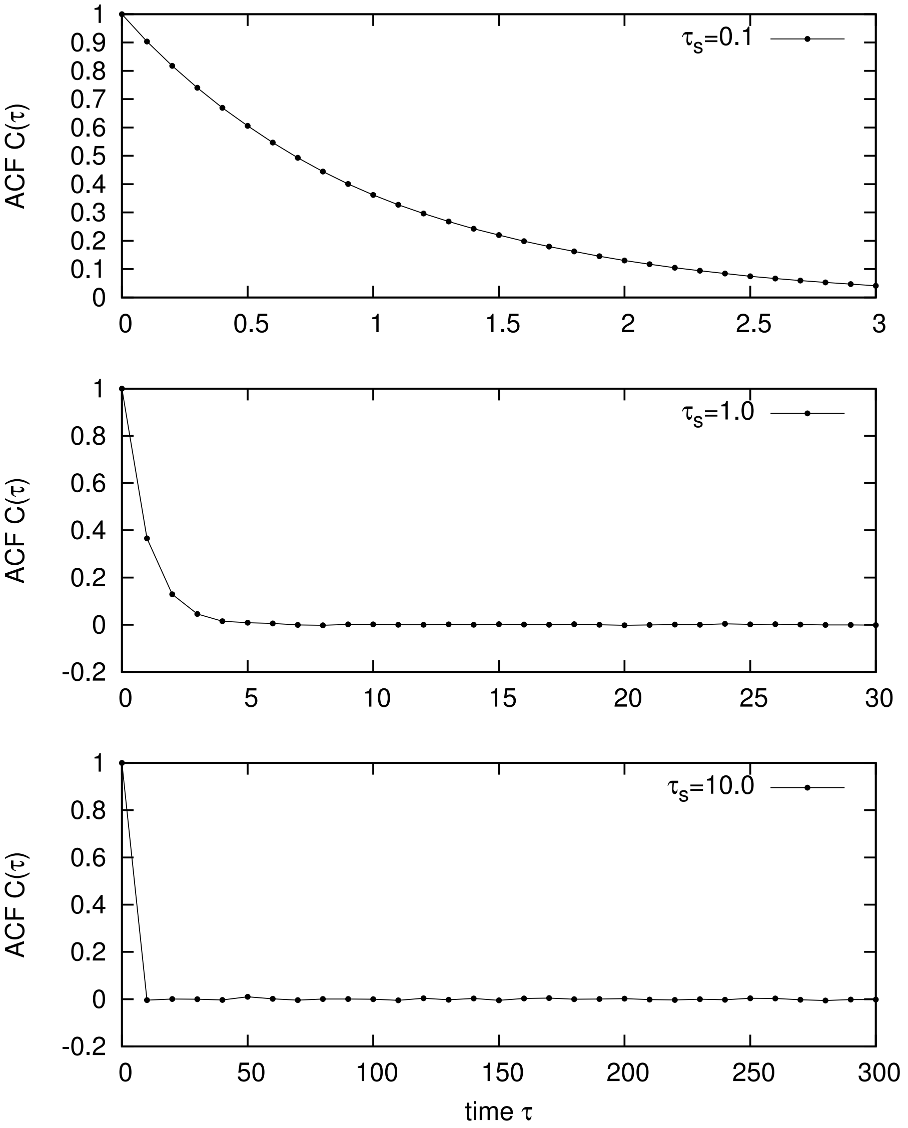

Fig. 4.2 Estimated ACFs for three synthetic OU processes with relaxation time $\tau_R = 1$ and sampling intervals $\tau_s = 0.1, 1.0, 10.0$ from top to bottom. For $\tau_s = 0.1$ finite time effects are small. For $\tau_s = 1.0$ finite time effects are large, but a KM analysis is still possible. For $\tau_s = 10.0$, two successive points are almost uncorrelated; a KM analysis is not possible.

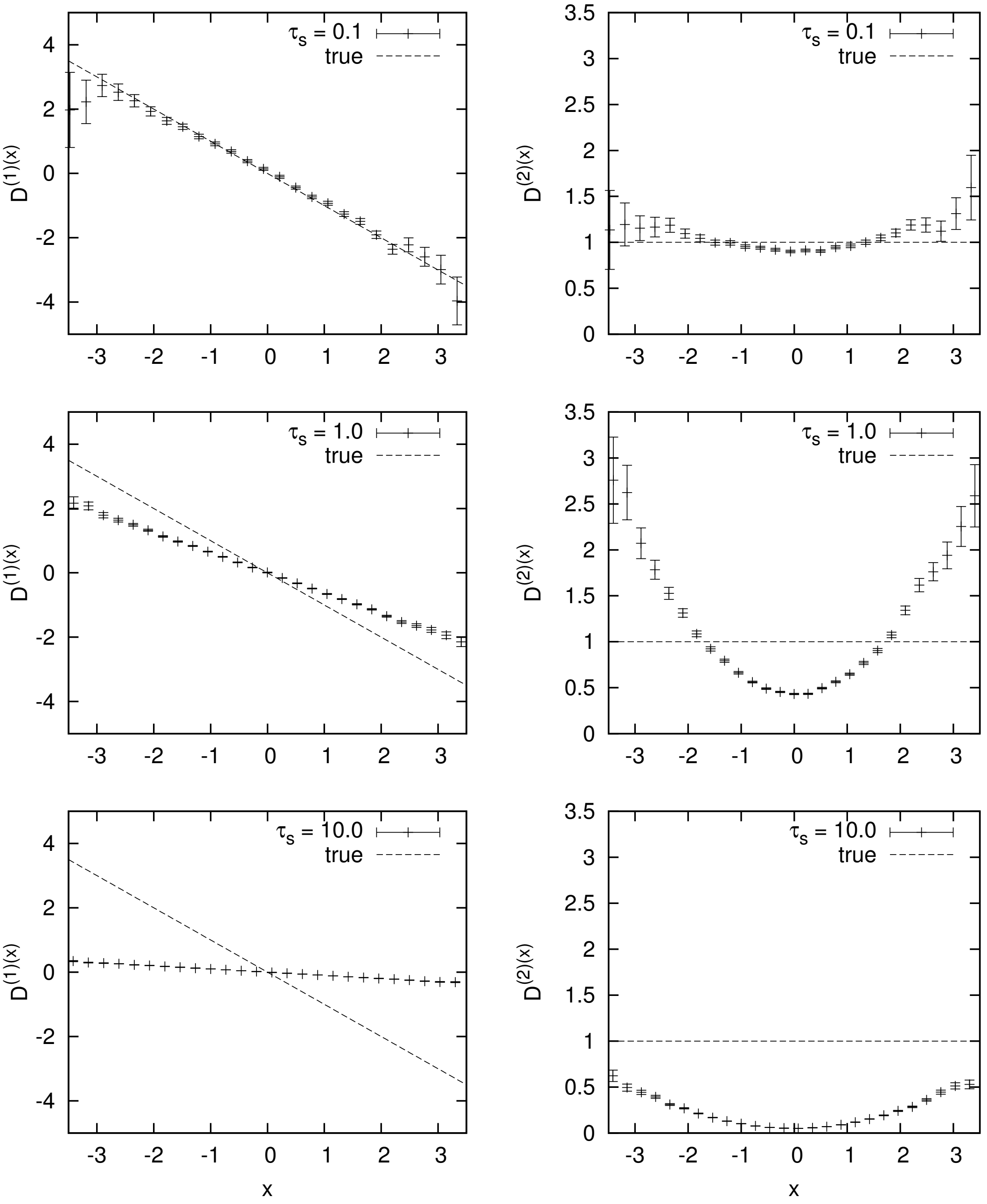

Fig. 4.3 Estimated finite time drift (left column) and diffusion (right column) coefficients $D^{(1,2)}_{\tau_s}(x)$ for three synthetic OU processes with relaxation time $\tau_R = 1$ and sampling intervals $\tau_s = 0.1, 1.0, 10.0$ from top to bottom. The dotted lines show the true coefficients to illustrate the finite time effects. The coefficients are estimated employing the Nadaraya-Watson estimator (3.46) with the kernel (3.29) and the bandwidth (3.30).

($C(\tau_s) \approx 0.37$). For $\tau_s = 10.0$ the correlation between two successive measurements is approximately zero. The information about the dynamics is lost, and a KM analysis is not possible, even if finite time effects are taken into account (cf. discussion is Sect. 4.6).

In Fig. 4.3 one can see that the variance of the estimated coefficients decreases as the sampling interval increases. Therefore, it can be advantageous to use the information of estimated finite time coefficients also for larger sampling intervals as is done in the analysis method introduced in the following section.

4.2 The optimization procedure

This section describes how Lade's method to compute the finite time KM coefficients can be inverted to obtain the true KM coefficients. This leads us to an optimization problem. The idea is as follows. At first, one has to represent the KM coefficients with a set of free parameters σ. For example, one can make a polynomial ansatz like

$$D^{(1)}(x,\sigma) = a_0 + a_1 x + a_2 x^2 + \cdots + a_n x^n\,,$$
$$D^{(2)}(x,\sigma) = b_0 + b_1 x + b_2 x^2 + \cdots + b_m x^m\,,$$

with a set of free parameters

$$\sigma = \{a_0, a_1, \ldots, a_n, b_0, b_1, \ldots, b_m\}\,.$$

Another possibility is a representation in form of spline curves. In this case, one defines a set of sampling points $x_1, x_2, \ldots, x_n$. In the numerical integration of the AFPE, $D^{(1)}$ and $D^{(2)}$ are represented as spline interpolations through these sampling points. The free parameters are then

$$\sigma = \left\{D^{(1)}(x_1), \ldots, D^{(1)}(x_n), D^{(2)}(x_1), \ldots, D^{(2)}(x_n)\right\}\,.$$

For a specific set of parameters σ, one can compute the conditional moments $M_\tau^{(1)}(x,\sigma)$ and $M_\tau^{(2)}(x,\sigma)$, for all x and τ values of interest by solving the AFPE. Some details on the numerics are described in Sect. 4.8.

The aim of the optimization procedure is to find the set of parameters σ^* such that $M_\tau^{(1)}(x,\sigma^*)$ and $M_\tau^{(2)}(x,\sigma^*)$ are as close as possible to the conditional moments $\hat{M}_\tau^{(1)}(x)$ and $\hat{M}_\tau^{(2)}(x)$ one has estimated from the time series data. To this end, one has to define a distance measure. We employ the least square distance

$$V(\sigma) = \sum_{i=1}^{M} \sum_{j=1}^{N} \left\{ \frac{\left[\hat{M}_{\tau_i}^{(1)}(x_j) - M_{\tau_i}^{(1)}(x_j,\sigma)\right]^2}{\left(\hat{\sigma}_{ij}^{(1)}\right)^2} + \frac{\left[\hat{M}_{\tau_i}^{(2)}(x_j) - M_{\tau_i}^{(2)}(x_j,\sigma)\right]^2}{\left(\hat{\sigma}_{ij}^{(2)}\right)^2} \right\}\,, \qquad (4.24)$$

which is weighted by measures of the statistical uncertainty in the estimation of the conditional moments $\hat{\sigma}_{ij}^{(1)}$ and $\hat{\sigma}_{ij}^{(2)}$. Applying an expression from Ref. [HMSW04] for the standard deviation of the Nadaraya-Watson estimator, the statistical uncertainties can be computed as

$$\hat{\sigma}_{ij}^{(1)} = \sqrt{\frac{||K||_2}{h}} \sqrt{\frac{\hat{M}_{\tau_i}^{(2)}(x_j) - \left(\hat{M}_{\tau_i}^{(1)}(x_j)\right)^2}{\sum_{k=1}^{T} \frac{1}{h} K\left(\frac{x_j - X_{t_k}}{h}\right)}}, \tag{4.25a}$$

$$\hat{\sigma}_{ij}^{(2)} = \sqrt{\frac{||K||_2}{h}} \sqrt{\frac{\hat{M}_{\tau_i}^{(4)}(x_j) - \left(\hat{M}_{\tau_i}^{(2)}(x_j)\right)^2}{\sum_{k=1}^{T} \frac{1}{h} K\left(\frac{x_j - X_{t_k}}{h}\right)}}, \tag{4.25b}$$

where $||K||_2^2$ is the L_2 norm of the kernel, thus

$$||K||_2 = \sqrt{\int K^2(x) \mathrm{d}x} \,. \tag{4.26}$$

The parameter set σ^* that minimizes the least square distance corresponds to the maximum likelihood estimation if two conditions are satisfied. First, the estimates $\hat{M}_{\tau_i}^{(k)}(x_j)$ are Gaussian distributed around $M_{\tau_i}^{(k)}(x_j, \sigma^*)$ with standard deviation $\hat{\sigma}_{ij}^{(k)}$. Second, the estimates $\hat{M}_{\tau_i}^{(k)}(x_j)$ are independent for different i, j, k. If one employs kernel regression, this is not the case for "neighboring" coefficients if $|x_j - x_{j\pm1}|$ is larger than the width of the employed kernel. The kernel (3.29) with a bandwidth h for instance, has a width given by $w = 2\sqrt{5}h$. Therefore we sample the x axis with a sampling interval equal to w.

Regarding the optimization, a large variety of methods is available. In the examples presented in the following, an implementation of a trust region algorithm [CGT00] from the Intel Math Kernel Library 10.1 for Linux [MKL] was used.

4.3 Monte Carlo error propagation

The question of how much information about the dynamics is contained in a time series data set depends on both the sampling interval and the amount of data. From the discussion in Sect. 4.1.2, it becomes clear that the larger the sampling interval of the time series data, the less information about the dynamics is contained in the data. The more data we have, the more precisely we can estimate the conditional moments, which allows for a more accurate evaluation of the KM coefficients. If a data set contains only very little information about the dynamics, the introduced optimization procedure might yield wrong or inaccurate results. In order to assess the reliability of the obtained results, it is therefore of great value to estimate uncertainties for the determined model parameters. Since we have to deal with a highly nonlinear optimization problem, this is unfortunately no trivial task. An often applied technique in those situations is the *Monte Carlo error propagation* (MCEP) [ABT05].

To explain the idea of the MCEP technique, it is helpful to introduce two terms often used in the context of inverse problems, namely the *forward problem* and the *backward problem*. Loosely speaking, the forward problem is to use a model to produce data:

$$\text{forward problem:} \quad \boxed{\text{model} \longrightarrow \text{data}}$$

A typical example would be to solve Newton's equation of motion for a specific set of forces (model) to obtain the trajectory of a particle (data). The backward problem is to find a suitable model that describes a given data set, which is in general assumed to be subject to noise sources:

$$\text{backward problem:} \quad \boxed{\text{data} + \text{noise} \rightarrow \text{model}} \tag{4.27}$$

In the above example, the backward problem would be to find the forces that act on a particle from a measured trajectory, which is subject to measurement noise. The backward problem has generally no unique solution but depends on a specific model ansatz with a set of parameters one has to obtain such that the model fits at best to the data.

The first step of the MCEP approach is to solve the backward problem with a specific model ansatz. Then, one has to solve the forward problem for the obtained model to produce a data set, which – provided that the forward problem can be solved with arbitrary accuracy – is not perturbed by noise. In a next step, one generates an ensemble of pseudo data sets, by perturbing the data set obtained from the model with different realizations of noise. For each of these pseudo data sets, one again has to solve the backward problem with the same model ansatz. The standard deviations of the obtained model parameters over the ensemble of pseudo data sets can then be used as error estimates. Thereby it is crucial that the noise one uses to generate the pseudo data sets has similar properties as the noise in the original data sets.

In the actual case, we do not regard the time series data itself as *data* but the measured conditional moments. As the *model* we regard the AFPE with some parameterized drift and diffusion coefficients. The forward problem is then to solve the AFPE to obtain the corresponding conditional moments, whereas the backward problem is to obtain KM coefficients that correspond to the measured conditional moments.

The solution of the backward problem yields the coefficients $M_{\tau_i}^{(1,2)}(x_j, \sigma^*)$. It is assumed that the errors of the estimated conditional moments are Gaussian distributed with standard deviations according to Eqs. (4.25). Therefore the coefficients of a pseudo data set are computed as

$$M_{\tau_i}^{(1,2)}(x_j, \sigma^*) + \hat{\sigma}_{ij}^{(1,2)} \Gamma_{ij} \, , \tag{4.28}$$

where Γ_{ij} are independent standard normal distributed random numbers.

It should be noted that the MCEP method assumes that the estimates $\hat{M}^{(k)}_{\tau_i}(x_j)$ are all independent for different i, j and k. Therefore it is important that the x axis is sampled as described at the end of the previous section.

A practical problem that occurs in connection with the MCEP procedure is that for some pseudo data sets, the optimization procedure can get stuck in a local minimum at a distance from the global minimum. This can lead to a significantly overestimated errors. To overcome this problem, one has to detect these *outliers* and remove them from the calculation of the standard deviation over the ensemble of pseudo data sets. This is demonstrated with the first numerical example in Sect. 4.4.1.

4.4 Parametric examples

In the following, two examples with synthetic time series are presented. In both presented examples, the sampling interval of the constructed time series is approximately of the same order of magnitude as the relaxation time of the underlying process because then it is both necessary and possible to take into account finite time effects as was demonstrated in Sect. 4.1. Using the first example, we also regard the problem of outliers in MCEP approach and the way it is solved.

4.4.1 Ornstein-Uhlenbeck process

As a first example, we consider an OU process, i. e., a Langevin process with linear drift and constant diffusion,

$$\begin{aligned} D^{(1)}(x) &= -\gamma x\,, \\ D^{(2)}(x) &= \alpha\,, \end{aligned}$$

with $\gamma, \alpha > 0$. Such a process can always be rescaled such that

$$D^{(1)}(x) = -x\,, \tag{4.29a}$$

$$D^{(2)}(x) = 1\,, \tag{4.29b}$$

so we take this as a first example.

At first, a synthetic time series is created by a numerical simulation of the corresponding Langevin equation with the Euler-Maruyama scheme. Thereby, a time step $\Delta t = 10^{-3}$ is used, but only every 1000th time step is stored so that the sampling interval is $\tau_1 = 1$. The computed time series consists of 10^6 data points. In the next step, the finite time KM coefficients are estimated for the two smallest available time increments τ_1 and τ_2. This is done via the Nadaraya-Watson estimator (3.46) with a reduced rule-of-thumb bandwidth $h = 0.8\hat{\sigma}N^{-1/5}$ (cf. discussion in Sect. 3.2). The blue crosses in Fig. 4.4 show the results for $D^{(1)}_{\tau_1}(x)$ (left) and $D^{(1)}_{\tau_1}(x)$ (right). The error bars correspond to the error estimates (4.25a) and (4.25b), respectively. As one can see, the finite time drift is clearly linear and the diffusion is quadratic, but the results are far away from Eqs. (4.22) so we are not in the limit of statistical independence. We make the parametric ansatz

$$D^{(1)}(x) = -ax\,, \tag{4.30a}$$

$$D^{(2)}(x) = b + cx^2\,, \tag{4.30b}$$

with the set of optimization parameters $\sigma = \{a, b, c\}$. After making an initial guess for the parameters, the optimization is started. The MCEP errors are determined employing 10^4 pseudo data sets.

The parameter values of the initial guess, the results of the optimization, the obtained errors, and the true parameter values are listed in Tab. 4.1. The initial guess corresponds to the blue dotted curves in Fig. 4.4. The result is depicted by the red solid curve while the true coefficients are represented by the black dots. The agreement between the result and the true coefficients is very good. For the diffusion, we also construct a 1σ-confidence band indicated by the red dashed lines. They correspond to the functions $(b \pm \sigma_{MCEP}(b)) + (c \pm \sigma_{MCEP}(c))x^2$.

Figure 4.5 illustrates the problem of outliers that occurs in connection to the MCEP approach because the optimization does not converge for all generated pseudo data sets. To identify these outliers, we plot the result for the parameter a for each pseudo data set against the residual

$$r = V(\sigma^*)\,. \tag{4.31}$$

One can clearly identify outliers by eye that are correlated with large residuals. To identify them numerically, we define a residual threshold r_{th} and only consider those pseudo data sets that are below this threshold (black dots in Fig. 4.5). The threshold is set to

$$r_{\text{th}} = \langle r \rangle + 2\langle |r - \langle r \rangle| \rangle\,, \tag{4.32}$$

Tab. 4.1 Results for the optimization parameters a, b and c together with the error estimates σ_{MCEP} obtained by the MCEP method and the initial guess for the OU example.

	a	b	c
initial guess	0.63	0.45	0.2
result	1.0016	1.006	0.003
σ_{MCEP}	0.0033	0.012	0.012
true value	1.0000	1.000	0.000

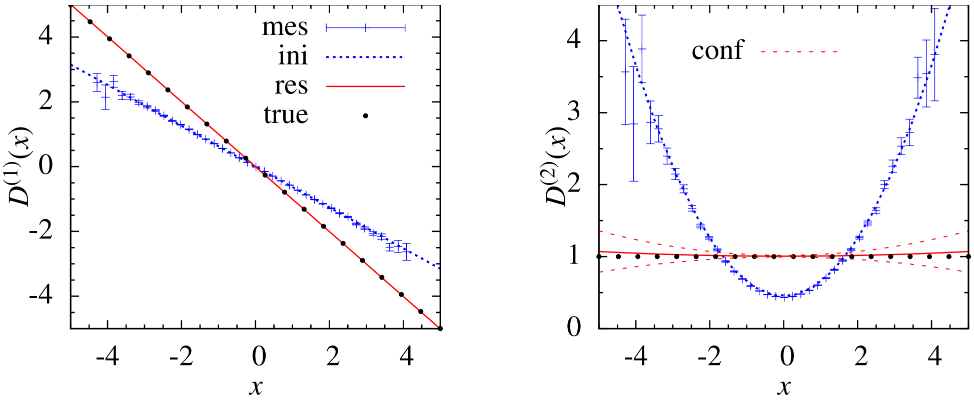

Fig. 4.4 Results of the optimization procedure for an OU process with $D^{(1)}(x) = -x$, $D^{(2)}(x) = 1$. The analyzed time series consists of 10^6 data points with a sampling interval $\tau_1 = 1$. The blue crosses with error bars are the estimated finite time coefficients $D^{(1)}_{\tau_1}$ (left) and $D^{(2)}_{\tau_1}$ (right). The blue dotted curves show the initial guess for the optimization, and the red solid ones show the result in comparison with the true coefficients (black dots). For the diffusion, the red dashed lines indicate a 1σ-confidence band.

where the brackets denote averages over the ensemble of pseudo data sets.

4.4.2 Multiplicative noise

As a second example, we consider a system with multiplicative noise:

$$D^{(1)}(x) = -x\,, \tag{4.33a}$$

$$D^{(2)}(x) = 1 + 0.5x^2\,. \tag{4.33b}$$

In the same manner as in the previous example, a time series consisting of 10^6 data points and a sampling interval of $\tau_1 = 1$ is generated. From finite time coefficients $D^{(1,2)}_{\tau_1}(x)$, we derive the parametric ansatz

$$D^{(1)}(x) = -ax\,,$$

$$D^{(2)}(x) = b + cx^2\,.$$

The initial guess and the result of the optimization are displayed in Fig. 4.6 and Tab. 4.2 analogously to the previous case of the OU process. Again, the resulting coefficients agree very well with the true coefficients.

4.5 Systematic evaluation of MCEP errors

In order to assess whether the MCEP approach really yields realistic error estimates, an ensemble of ten realizations of an OU process with the same properties as the time series

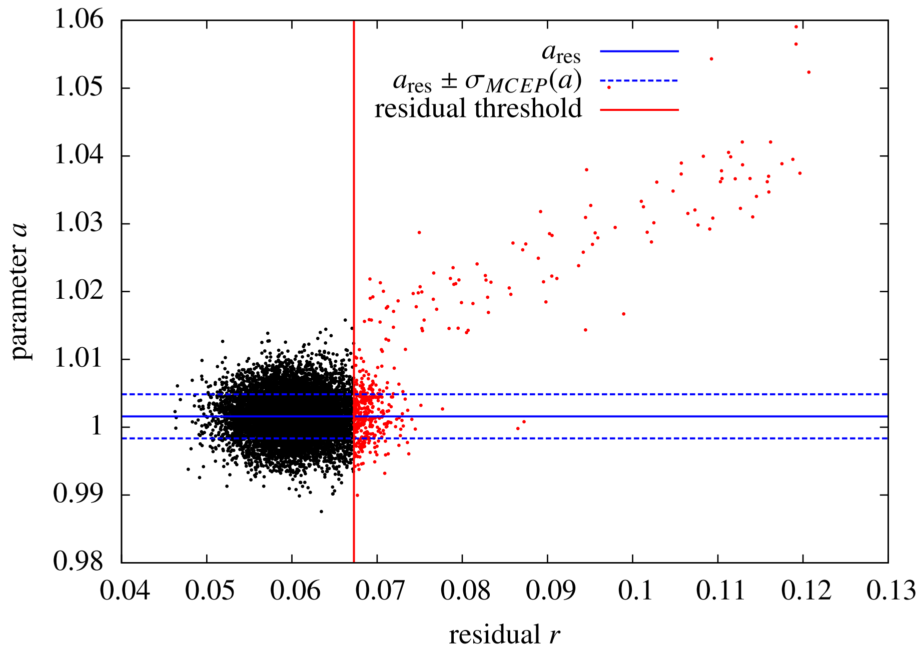

Fig. 4.5 The problem of outliers in the determination of MCEP errors. Each point in the plot represents the optimization result for the parameter a against the final residual of one of 10^4 pseudo data sets. To remove outliers from the evaluation of the MCEP error, a residual threshold is defined (red line). The removed outliers are represented by red dots. From all points below the threshold (black dots), the standard deviation is determined. The blue solid line represents the resulting parameter value, the blue dashed lines the $\pm\sigma$ interval.

Tab. 4.2 Results for the optimization parameters a, b and c together with the error estimates σ_{MCEP} obtained by the MCEP method and the initial guess for the process (4.33).

	a	b	c
initial guess	0.636	0.644	0.296
result	1.016	1.089	0.435
σ_{MCEP}	0.025	0.097	0.054
true value	1.000	1.000	0.500

used in Sect. 4.4.1 is generated. For each time series the whole analysis is performed. Figure 4.7 shows the results for each of the three parameters. By eye one can see that the estimated error bars are of the same order of magnitude as the fluctuations over the ensemble. For a quantitative assessment, the standard deviations of the parameter values over the ensemble are compared to the mean MCEP errors. The results are listed in

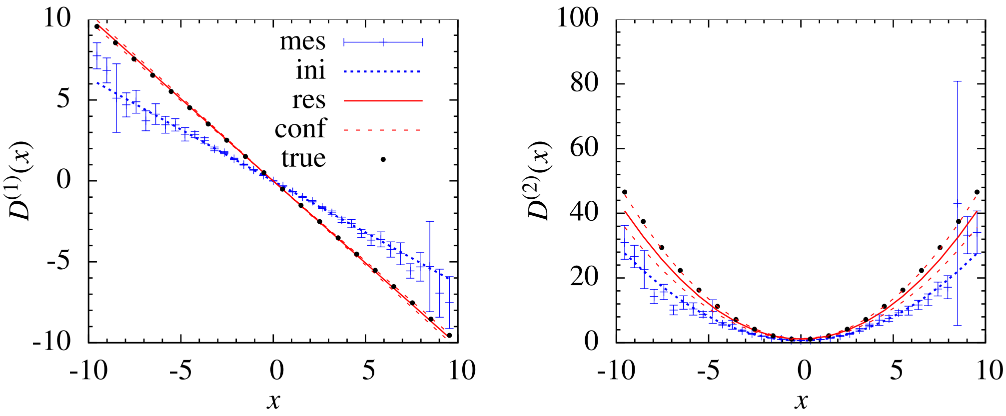

Fig. 4.6 Results of the optimization procedure for a system with multiplicative noise: $D^{(1)}(x) = -x$, $D^{(2)}(x) = 1 + 0.5x^2$. The analyzed time series consists of 10^6 data points with a sampling interval $\tau_1 = 1$. The representation is analogous to Fig. 4.4.

Tab. 4.3 Comparison between the standard deviations σ_E of estimated parameters in the ensemble of ten OU processes and the mean errors $\overline{\sigma_{MCEP}}$ computed by the MCEP approach.

Parameter	average	σ_E	$\overline{\sigma_{MCEP}}$
a	1.0014	0.0035	0.0033
b	1.009	0.012	0.014
c	−0.0006	0.0063	0.0116

Tab. 4.3. While the error of the parameter c is slightly overestimated, the other estimates agree well.

4.6 Limitations of the approach

Now we use the MCEP approach to demonstrate the limitations of the KM analysis caused by finite time effects and limited amount of data. To this end, we compute the error estimates for the parameters a, b and c for synthetic time series with different sampling intervals. The synthetic time series are generated in the same manner as described in Sect. 4.4.1. All data sets consist of 10^6 data points.

The result is shown in Fig. 4.8. One can see that the estimation of the diffusion parameters b and c breaks down around 2.5 relaxation times ($\tau_R = 1$), while the drift parameter a can still be estimated up to about 5 relaxation times. Above these values it is difficult to obtain robust error estimates with the MCEP approach because the afore-mentioned outliers become very frequent. However, using the MCEP approach

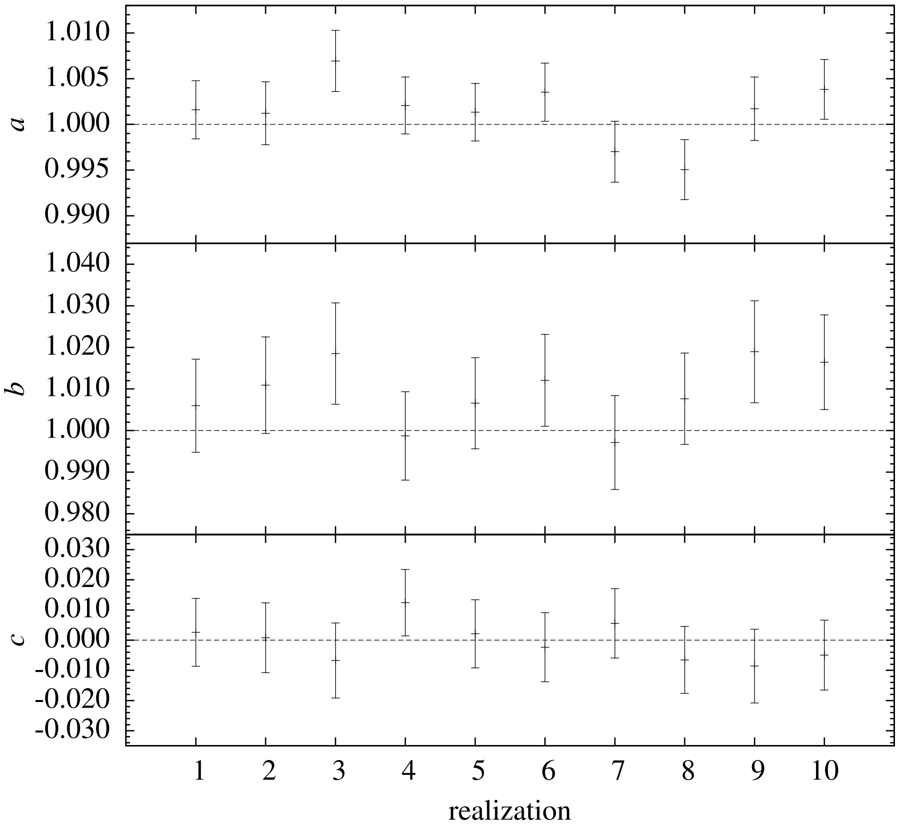

Fig. 4.7 Estimated parameters for an ensemble of ten OU processes according to Eqs. (4.30) with different noise realizations. The error bars are computed via the MCEP method. The horizontal dashed lines indicate the true values of the parameters. The sampling interval τ of the series is equal to the relaxation time $\tau_R = 1$.

for sampling intervals above these values, one will clearly notice that the KM analysis is no longer feasible.

Looking at Fig. 4.8, one further notices that the errors of b and c are strongly correlated, which is not surprising. That the absolute sizes of the errors are almost equal is only the case for the specific selection of parameters $a = b = 1$ and $c = 0$.

4.7 Parameter free examples

In this section we present two examples, where drift and diffusion coefficients are represented as spline curves. The interpolation points of the spline curves serve as optimization parameters. Therefore, the optimization is not really parameter free, but

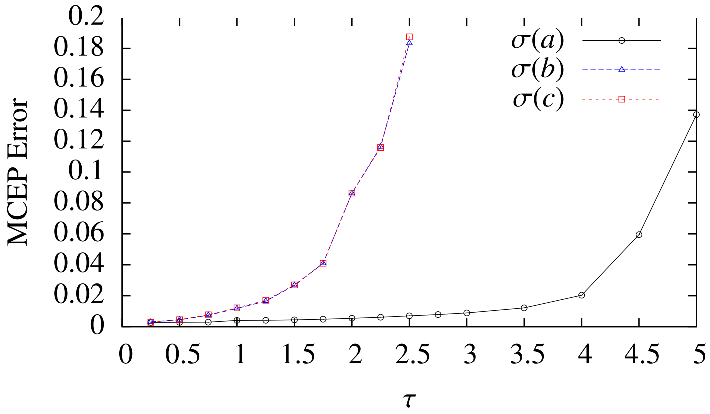

Fig. 4.8 Estimated MCEP errors for synthetic time series according to the model (4.30) with parameters $a = b = 1$ and $c = 0$, as a function of the sampling interval τ.

no assumption about the form of drift and diffusion functions have to be made. The disadvantage of this approach is that the optimization involves much more computational effort because the AFPE has to be solved numerically and because the number of optimization parameters ($\simeq 20$) is larger. Therefore we waive the computation of error estimates via the MCEP approach here because this would involve a large number of optimization runs which would require the use of large parallel computers.

4.7.1 Bistable system

The next example is a bistable system with two symmetric stable fixed points separated by an unstable fixed point:

$$D^{(1)}(x) = x - x^3 \tag{4.34}$$

$$D^{(2)}(x) = 1 \tag{4.35}$$

In contrast to the other presented examples, the sampling interval of the synthetic time series is chosen as $\tau_1 = 0.1$, which is one order of magnitude below the relaxation time. This is done for two reasons. The first reason is to demonstrate that even with such a small sampling interval, finite time effects on the diffusion coefficient can be quite dramatic as one can see from the initial guess in Fig. 4.9. The second reason is that because of the x^3 term in the drift coefficient, it is very intricate to keep the numerical integration of the AFPE stable, which has to be performed at least up to time τ_1. An integration up to a larger time τ would require more sophisticated methods than those described in Sect. 4.8, e. g., an adaptive time-stepping method.

Instead of a polynomial representation of the drift and diffusion coefficients that was used in the previous examples, now a representation via spline curves as described in

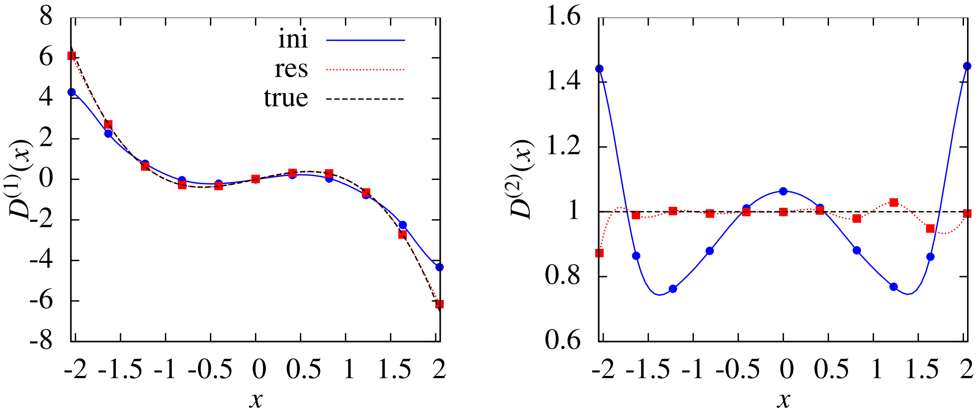

Fig. 4.9 Bistable system with $D^{(1)}(x) = x - x^3$, $D^{(2)}(x) = 1$. The analyzed time series consists of 10^7 data points with a sampling interval $\tau_1 = 0.1$. The blue and red symbols are sampling points, from which the corresponding curves (blue solid and red dotted lines) are computed as spline interpolations, and serve as optimization parameters. The blue dots represent the initial condition derived from the finite time coefficients $D^{(1,2)}_{\tau_1}$. The red squares show the result of the optimization. The black dashed curves show the true coefficients for comparison.

Sect. 4.2 is utilized. The blue dots in Fig. 4.9 show the finite time coefficients $D^{(1)}_{\tau_1}$ (left) and $D^{(2)}_{\tau_1}$ (right) at the selected sampling points. They represent the initial guess for the optimization parameters. The blue solid curves are the corresponding spline interpolations that are used in the numerical integration of the AFPE. As one can see, the deviations to the true coefficients, which are depicted by the black dashed curves, are relatively small in the case of the drift but quite dramatic in the case of diffusion. The red squares represent the resulting optimization parameters, and the red dotted curves depict the corresponding spline interpolations. They agree quite well with the true coefficients.

4.7.2 Phase dynamics

To analyze the synchronization tendency of a pair of coupled noisy phase oscillators ϕ_1 and ϕ_2, one can try to estimate the drift and diffusion coefficients for the phase difference $\phi = \phi_1 - \phi_2$. If one can identify a stable fixed point in the drift term, both oscillators tend to synchronize. This tendency is of course counteracted by the noise, which is why it is not trivial to identify.

In this case, the KM coefficients must be 2π periodic. This knowledge can be exploited by defining the KM coefficients as

$$D^{(n)}(x,t) = \lim_{\tau \to 0} \frac{1}{n!\tau} \langle [\phi(t+\tau) - \phi(t)]^n \rangle |_{\phi(t) \bmod 2\pi = x} . \tag{4.36}$$

This means that the phase ϕ in the data set is defined in a way that it can become

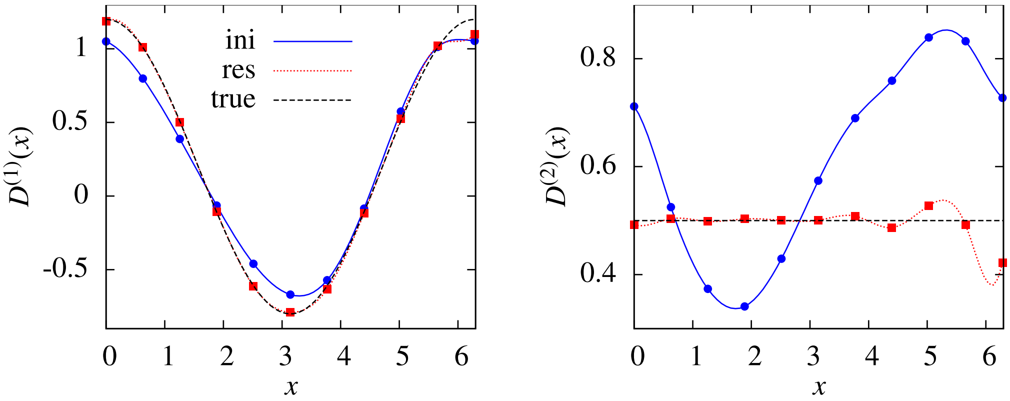

Fig. 4.10 Phase dynamics with $D^{(1)}(x) = 0.2 + \cos(x)$, $D^{(2)}(x) = 0.5$. The analyzed time series consists of 10^7 data points with a sampling interval $\tau_1 = 1$. The representation is analogous to Fig. 4.9.

arbitrarily large over time and is not restricted to the interval $[0, 2\pi)$. This is important to obtain correct phase increments. But since $D^{(n)}(x) = D^{(n)}(x + 2\pi)$, one conditions on phases taken modulo 2π to simplify the estimation of the conditional averages.

As an example, a system with

$$D^{(1)}(x) = 0.2 + \cos(x) \tag{4.37}$$

$$D^{(2)}(x) = 0.5 \tag{4.38}$$

is simulated to construct a time series with 10^7 data points and a sampling interval of $\tau_1 = 1$. As in the previous example, the drift and diffusion coefficients are represented as spline curves in the optimization. Figure 4.10 shows the initial guess, the result, and the true coefficients, in the same manner as in Fig. 4.9. The result agrees quite well with the true coefficients. The largest deviations occur in the diffusion between $x = 4$ and $x = 2\pi$. This is because there is an attractive fixed point at $x \approx 1.8$ and a repelling fixed point at $x \approx 4.5$. Therefore, the data density is very low in the latter region, which affects the optimization.

4.8 A note on the numerics

A problem connected to the numerical integration of the AFPE (4.11) lies in the fact that the integration domain is the whole $\mathbb{R}$ and the functions $W_{n,x}(x', t)$ do not need to fulfill any boundary conditions. It turned out that the numerics work well with a forward time centered space finite difference (FD) scheme with second order forward and backward differences on the boundaries. To be specific, the spatial derivatives in the interior of the integration domain are computed via centered FDs:

$$f'(x_i) \simeq \frac{f(x_{i+1}) - f(x_{i-1})}{2h}\,, \tag{4.39a}$$

$$f''(x_i) \simeq \frac{f(x_{i-1}) - 2f(x_i) + f(x_{i+1})}{h^2}\,. \tag{4.39b}$$

On the left and right boundaries, second order forward and backward FDs, respectively, are employed:

$$f'(x_1) \simeq \frac{-3f(x_1) + 4f(x_2) - f(x_3)}{2h}\,, \tag{4.40a}$$

$$f'(x_n) \simeq \frac{f(x_{n-2}) - 4f(x_{n-1}) + 3f(x_n)}{2h}\,, \tag{4.40b}$$

$$f''(x_1) \simeq \frac{2f(x_1) - 5f(x_2) + 4f(x_3) - f(x_4)}{h^2}\,, \tag{4.40c}$$

$$f''(x_n) \simeq \frac{-f(x_{n-3}) + 4f(x_{n-2}) - 5f(x_{n-1}) + 2f(x_n)}{h^2}\,. \tag{4.40d}$$

The time integration is done via the common fourth order Runge-Kutta method.

To compute the terms $M^{(n)}_{\tau_i}(x_j, \sigma)$ in the least square distance, Eq. (4.24), the AFPE has to be integrated for each n and j individually with a different initial condition $W_{n,x_j}(x', 0) = (x' - x_j)^n$. Therefore, it is very easy and efficient to parallelize these computations. The program written in the course of this thesis is OpenMP parallel [OMP], which speeds up the calculations to a factor close to four on a desktop machine with four CPUs.

5 Application to force measurement of optical tweezers

This chapter presents an application of the method discussed in Chap. 4 to experimental data of an optical trapping experiment. In this experiment, a micrometer-sized Brownian particle is trapped by an optical tweezers system. The data used in this work were measured by Florian Hörner at the Institute for Applied Physics in Münster. The results are published in Ref. [HFHD12].

5.1 Description of the experiment

Figure 5.1 shows the setup of the optical trapping experiment. The sample is a thin liquid water film containing micrometer sized polystyrene particles performing Brownian motion. If the laser beam is focused on such a particle, it becomes trapped by the optical light pressure. The particle is filmed by a CCD camera. From the recorded images,

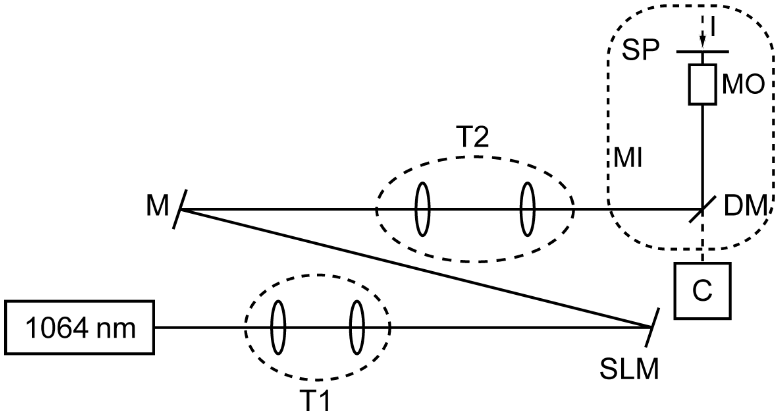

Fig. 5.1 Illustration of the experimental setup. DM: dichroic mirror; C: CMOS camera; I: illumination; MI: microscope; MO: microscope objective; T1, T2: telescope systems; SLM: physe-only spatial light modulator; SP: sample plain. The picture is reproduced from Ref. [HFHD12].

x and y coordinates (perpendicular to the laser beam) of the position of the center of mass of the particle are computed via an image processing algorithm. The sampling frequency of the camera is 3966 Hz. The measured data set consists of 150 samples of a time series of 9998 data points each. This makes a total amount of about 1.5 million data points. For more details about the experiment, the reader is referred to Ref. [HFHD12].

5.2 Modeling

The equation of motion for a Brownian particle in an optical trap reads for one spatial dimension [BM74]

$$m_p\ddot{x}(t) = F_{\mathrm{fr}}(t) + F_{\mathrm{op}}(x(t)) + F_{\mathrm{th}}(t)\,, \tag{5.1}$$

where m_p is the mass of the particle, F_{fr} is the friction force, F_{op} is the force induced by the optical trap and F_{th} denotes the thermal fluctuations. The general form of the friction force reads

$$F_{\mathrm{fr}}(t) = -\int \gamma(t-t')\dot{x}(t')\mathrm{d}t'\,, \tag{5.2}$$

with a memory kernel $\gamma(t)$. According to the fluctuation dissipation theorem [KTH91], $\gamma(t)$ is connected to the correlation function of the thermal fluctuations:

$$\langle F_{\mathrm{th}}(t)F_{\mathrm{th}}(t')\rangle = k_B T\gamma(|t-t'|)\,. \tag{5.3}$$

Here, k_B denotes the Boltzmann constant and T the absolute temperature. Assuming a laminar velocity profile around a spherical particle and no-slip boundary conditions, the kernel is given by

$$\gamma(t-t') = 2\delta(t-t')6\pi\eta r \tag{5.4}$$

where η is the dynamic viscosity of the fluid and r the radius of the particle. This yields the well-known Stokes' law

$$F_{\mathrm{fr}}(t) = -\lambda\dot{x}(t) \tag{5.5}$$

with the friction coefficient $\lambda = 6\pi\eta r$. On time scales $\tau \gg \tau_I = m_p/\lambda$ ($\tau_I \sim 0.05\,\mu\mathrm{s}$ in our experimental setup), inertia can be neglected. With a linear optical force $F_{\mathrm{op}} = -kx$, this yields

$$\dot{x}(t) = -\frac{k}{\lambda}x(t) + \sqrt{2D^{(2)}}\Gamma(t)\,, \tag{5.6}$$

with $\langle \Gamma(t)\Gamma(t')\rangle = \delta(t-t')$ and the diffusion coefficient

$$D^{(2)} = \frac{k_B T}{6\pi\eta(T)r}, \tag{5.7}$$

which is known as the Einstein-Stokes equation. For a constant temperature equal to the room temperature of $T = (294 \pm 2)\,\mathrm{K}$, a particle diameter of $2r = (1.002 \pm 0.043)\,\mu\mathrm{m}$, and a viscosity of $\eta = (1.00 \pm 0.02)\cdot 10^{-3}\,\mathrm{Nsm}^{-2}$, the Einstein-Stokes equation predicts a diffusion constant of

$$D^{(2)}_{\mathrm{ES}} = (0.43 \pm 0.03)\,(\mu\mathrm{m})^2\mathrm{s}^{-1}\,. \tag{5.8}$$

A more realistic treatment goes beyond Stokes' law and also considers the momentum that is transferred from the particle to the fluid. Reference [BM74] gives a derivation of Eqs. (5.1), (5.2), and (5.3) for a macroscopic sphere in an incompressible fluid from linearized stochastic hydrodynamic equations. Thereby the Fourier transform of the memory kernel is computed as

$$\hat{\gamma}(\omega) = 6\pi\eta r\left[1 + (1-\mathrm{i})r\sqrt{\frac{\omega\rho_f}{2\eta}} - \frac{\mathrm{i}\omega\rho_f r^2}{9\eta}\right]. \tag{5.9}$$

Here, ρ_f denotes the mass density of the fluid. This corresponds to a friction force

$$\begin{aligned} F_{\mathrm{fr}}(t) = &- \lambda\dot{x}(t) - \frac{m_f}{2}\ddot{x}(t) \\ &- 6r^2\sqrt{\pi\rho_f\eta}\int_{-\infty}^{t} \mathrm{d}t'\,\frac{\ddot{x}(t')}{\sqrt{t-t'}}\,, \end{aligned} \tag{5.10}$$

where $m_f = (4\pi/3)\rho_f r^3$ is the mass of the displaced fluid. The correlation of the thermal fluctuations shows a negative algebraically decaying tail

$$\langle F_{\mathrm{th}}(t)F_{\mathrm{th}}(t')\rangle = -3r^2 k_B T\sqrt{\pi\rho_f\eta}\,|t-t'|^{-3/2} \tag{5.11}$$

for $|t-t'|^{-3/2} > 0$. The memory term in the friction force (5.10) and the long correlations of the thermal fluctuations clearly obliterate the Markov property of the process. However, it is possible that a finite ME time scale τ_{ME} exists, which means that the process can approximately be described by a Markov process for times larger than τ_{ME}. If such a time scale is found, one can try to find a model in form of Eq. (5.6) with an effective drag coefficient λ and diffusion coefficient $D^{(2)}$ with our data analysis method.

To obtain a rough estimation of the ME time scale, we compare the mean squared displacement $\mathrm{MSD}(t) = \langle(\Delta x(t))^2\rangle$ of the full hydrodynamic model $\mathrm{MSD}_{\mathrm{H}}(t)$, which was computed by Clercx [CS92], with the MSD of the Markov model, Eq. (5.6), $\mathrm{MSD}_{\mathrm{M}}(t)$. Figure 5.2 shows a plot of the MSDs for both models with the parameters according to

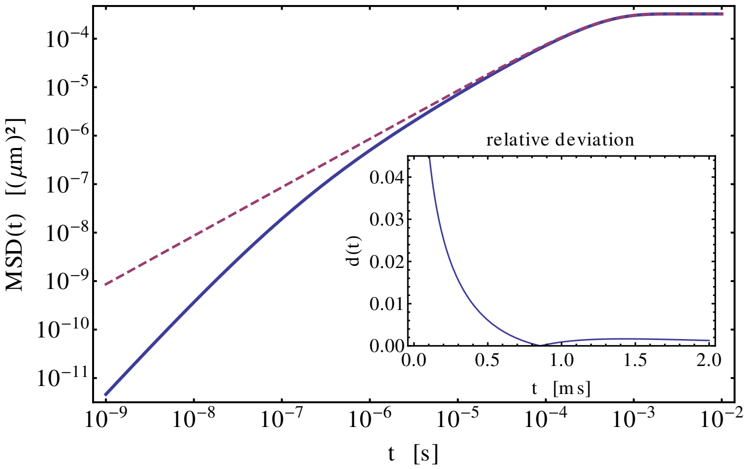

Fig. 5.2 Mean squared displacement against time according to the full hydrodynamic model (blue solid line) and the overdamped Markov model (red dashed line) as a double logarithmic plot. The inset shows the relative deviation, Eq. (5.12), between both curves. Figure reproduced from [HFHD12].

our experiment. In the overdamped Markov model (red dashed curve), there is only one characteristic time scale $\tau_k = \lambda/k \sim 10^{-4}$ s depending on the stiffness k of the optical trap. Below this time scale, there is the so-called diffusive regime in which the MSD grows linear with time, $\mathrm{MSD_M}(t \ll \tau_k) = 2D^{(2)}t$. Above this time scale, the MSD saturates to the constant value $2k_BT/k$.

In the full hydrodynamic model, the smallest characteristic time scale is the inertia time scale $\tau_I \sim 10^{-8}$ s. For times smaller than τ_I, the MSD grows quadratically with time, $\mathrm{MSD}_H(t \ll \tau_I) = (k_BT/m^*)t^2$, where $m^* = m_p + m_f/2$. This corresponds to the so-called ballistic regime[1]. Above the ballistic regime, it takes about four decades until the MSD approaches the diffusive regime and coincides with the overdamped Markov model. These four decades are influenced by hydrodynamic memory effects. The inset of Fig. 5.2 shows the relative deviation

$$d(t) = \frac{|\mathrm{MSD_H}(t) - \mathrm{MSD_M}(t)|}{\mathrm{MSD_H}(t)} \tag{5.12}$$

between the MSDs of the two models. According to this, the influence of the hydrodynamic memory effects is still present at times $t \sim \tau_k$. For times larger than 0.4 ms, the relative deviation becomes smaller than one percent. Therefore, a ME time scale of this

---

[1] Below this regime there is the additional characteristic time scale of sound propagation in which the incompressibility assumption becomes invalid. But this is not covered by the full hydrodynamic model.

order of magnitude is expected. A direct test of our data for Markovianity is presented in Sect. 5.3 yielding a ME time scale of $\tau_{\mathrm{ME}} \approx 0.5\,\mathrm{ms}$ which is in good agreement to the discussion above.

5.3 Preinvestigations

As a first preinvestigation, we take a look at the Markov property. A necessary condition for a process to be Markovian on a specific time scale τ is the validity of the CKE (cf. Eq. (2.8) in Sect. 2.2.2):

$$p_{2\tau}(x'|x) = \int \mathrm{d}x'' p_\tau(x'|x'') p_\tau(x''|x)\,, \tag{5.13}$$

where $p_\tau(x'|x) := p(x', t+\tau|x, t)$ denotes the transition PDF of the process. We further define

$$p_\tau^{\mathrm{CK}}(x'|x) := \int \mathrm{d}x'' p_{\tau/2}(x'|x'') p_{\tau/2}(x''|x)\,, \tag{5.14a}$$

$$f_\tau(x', x) := p_\tau(x'|x) f(x)\,, \tag{5.14b}$$

$$f_\tau^{CK}(x', x) := p_\tau^{CK}(x'|x) f(x)\,. \tag{5.14c}$$

To test our data for Markovianity on a time scale τ, estimates for the joint PDFs $f_{2\tau}$ and $f_{2\tau}^{\mathrm{CK}}$ are compared (cf. Ref. [FPST11]). The estimates are computed employing the multivariate kernel estimator (3.33) with the bandwidth matrix (3.36). Figure 5.3 shows the corresponding contour plots for $\tau = \tau_s$ and $\tau = 2\tau_s$ for the two components of the process. For $\tau = \tau_s$ (upper panels), one can see clear deviations between the contour lines which indicate that the process is not Markovian on this time scale. For $\tau = 2\tau_s$ the deviations vanish. This leads to the conclusion that the process has a ME time scale $\tau_{\mathrm{ME}} \approx 2\tau_s$. Therefore we only include conditional moments with time increments $\tau \geq 2\tau_s$ into the minimization of Eq. (4.24).

As a next step, we take a look at the ACFs

$$C_x(\tau) = \frac{\langle X(t) X(t+\tau)\rangle_t}{\langle (X(t))^2\rangle_t}\,, \tag{5.15a}$$

$$C_y(\tau) = \frac{\langle Y(t) Y(t+\tau)\rangle_t}{\langle (Y(t))^2\rangle_t}\,, \tag{5.15b}$$

to get an impression of the typical time scales of the system and to decide whether the sampling interval τ_s is sufficiently small for a reliable KM analysis. The ACFs are shown in Fig. 5.4. To evaluate the relaxation time as a typical time scale of the system, an exponential, $\mathrm{e}^{-c\tau}$, is fitted to the first points of the ACF and $\tau_R \approx c^{-1}$ is taken as a rough estimate. According to this estimate, $\tau_R \approx 2\tau_s$. This means that the relaxation

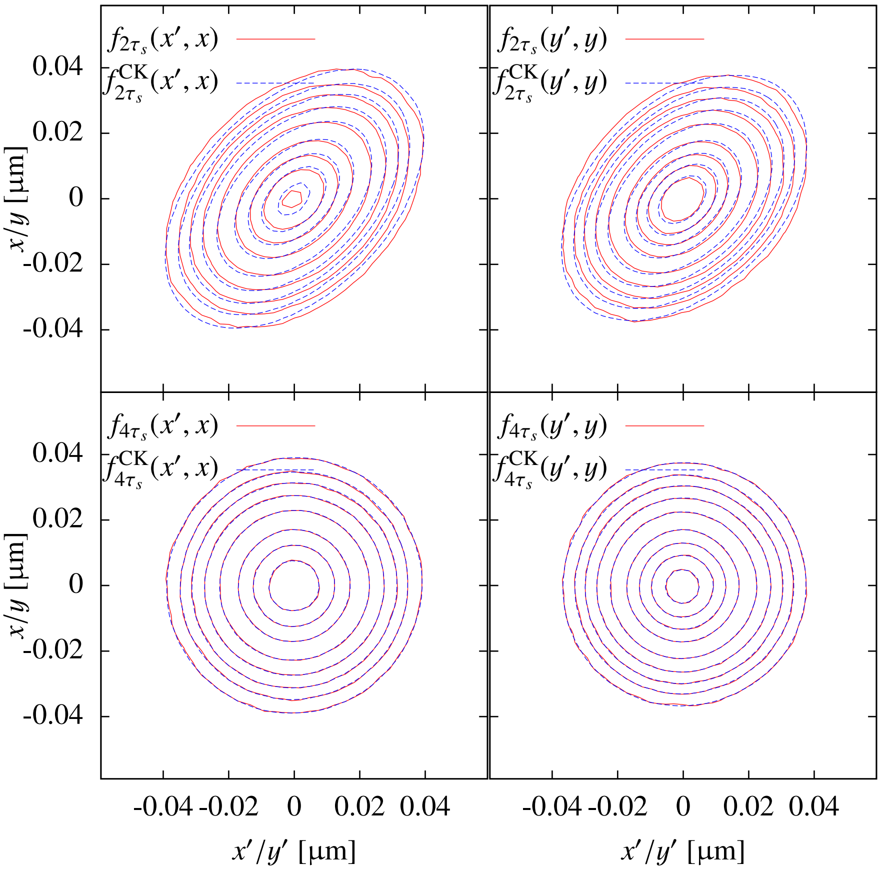

Fig. 5.3 Test of the validity of the CKE for a time scale equal to the sampling interval (upper panels) and twice the sampling interval (lower panels) of the x component (left panels) and y component (right panels) of the data set. The plots show contour lines of estimated joint PDFs, according to Eqs. (5.14). In the lower panels the contour lines match well in contrast to the upper panels indicating a ME time scale of $\tau_{\rm ME} \approx 2\tau_s$.

time of the process is approximately equal to the ME time scale. Therefore, according to the discussion in Sect. 4.6, the KM analysis should be possible.

The last step is to check whether it is possible or not to regard the x and y components of the particle motion as two independent processes. To this end, the finite time drift

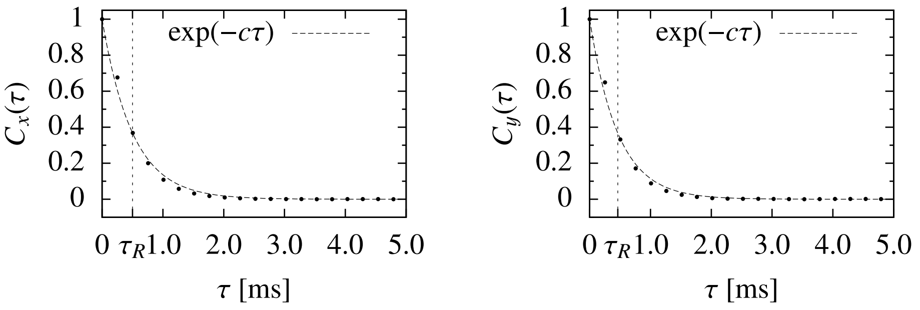

Fig. 5.4 ACFs for the x (top) and y (bottom) component of the particle motion. To obtain a rough estimation of the relaxation time τ_R, we fit an exponential $\exp(-c\tau)$ to the first points of the correlation function. This leads to the estimate $\tau_R \approx c^{-1}$.

vector field $\boldsymbol{D}^{(1)}(x, y, \tau) = (D_x^{(1)}(x, y, \tau), D_y^{(1)}(x, y, \tau))^\top$ with

$$D_x^{(1)}(x, y, \tau) = \frac{1}{\tau}\langle X(t+\tau) - X(t)|X(t) = x; Y(t) = y\rangle$$

$$D_y^{(1)}(x, y, \tau) = \frac{1}{\tau}\langle Y(t+\tau) - Y(t)|X(t) = x; Y(t) = y\rangle$$

is measured for $\tau = \tau_s$ employing the multivariate Nadaraya-Watson estimator (3.48), where the bandwidth matrix is calculated as described in Sect. 3.1.3. It is assumed that the qualitative form of the drift vector field is not affected that much from finite time effects and deviations from the Markov property. In Fig. 5.5 we show contour plots of $D_x^{(1)}(x, y, \tau)$ (left) and $D_y^{(1)}(x, y, \tau)$ (right). In a region with a radius of about 0.04 μm around the origin of the coordinate system, where most of the data points are, the contour lines of $D_x^{(1)}(x, y, \tau)$ and $D_y^{(1)}(x, y, \tau)$ are approximately linear and parallel to the y axis and x axis, respectively. Hence,

$$D_x^{(1)}(x, y, \tau) = D_x^{(1)}(x, \tau)\,, \tag{5.16a}$$

$$D_y^{(1)}(x, y, \tau) = D_y^{(1)}(y, \tau)\,. \tag{5.16b}$$

Therefore, we treat the two components of the particle motion as independent processes.

5.4 Analysis results

To estimate the drift and diffusion coefficients for each of the two processes, we first make a parametric ansatz in form of an OU process,

$$D^{(1)}(x) = -\gamma x \tag{5.17}$$

$$D^{(2)}(x) = \alpha \tag{5.18}$$

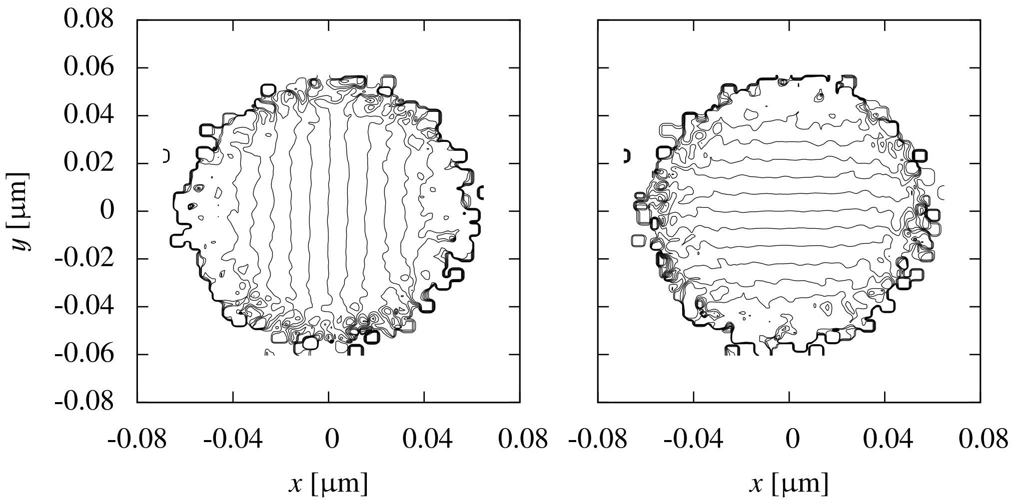

Fig. 5.5 Contour plot of the x component (left) and the y component (right) of the measured drift vector field. As one can see, the x component does not significantly depend on y and vice versa.

with optimization parameters γ and α. The experience from synthetic time series data is that the best results are achieved if one includes the finite time coefficients of the n smallest time increments $\tau_i = i\tau_s$, such that τ_n is between one and two relaxation times. Because of the finite ME time scale of $2\tau_s$, the conditional moments with $\tau = i\tau_s$, $i = 2, 3, 4$ are included into the least squares potential, Eq. (4.24). The conditional moments are estimated employing the Nadaraya-Watson estimator (3.46) with a reduced rule-of-thumb bandwidth $h = 0.8\hat{\sigma}N^{-1/5}$ (cf. discussion in Sect. 3.2).

Tab. 5.1 Results for the optimization parameters γ and α for the x and y components of the process together with the error estimates σ_{MCEP} obtained by the MCEP method.

	γ [s^{-1}]	α [(μm)^{2}s^{-1}]
x comp.		
result	2004.6	0.32910
σ_{MCEP}	4.2	0.00064
y comp.		
result	2212.4	0.32240
σ_{MCEP}	4.8	0.00067

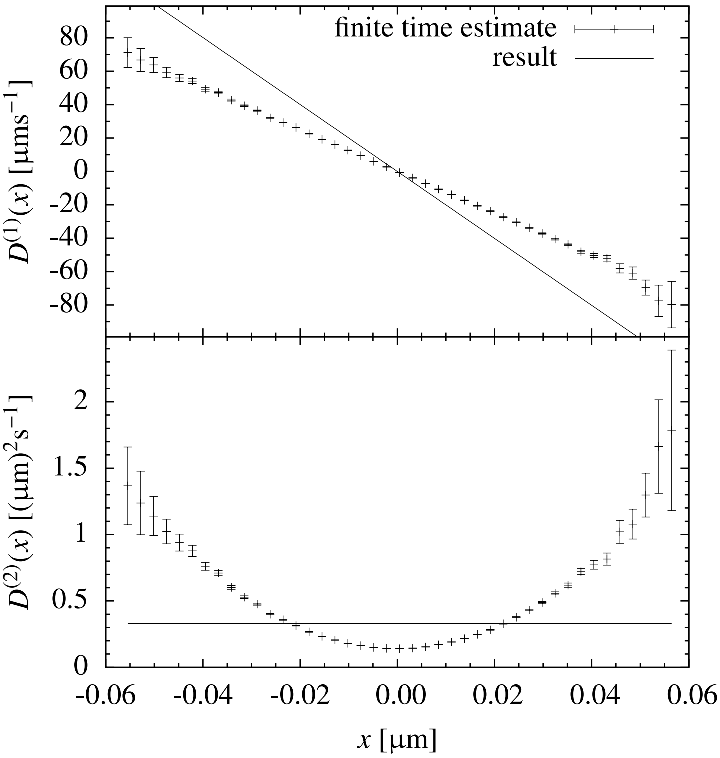

Fig. 5.6 Result of the optimization for drift (top) and diffusion (bottom) coefficients of the x coordinate of the particle motion. The symbols with the error bars are the estimated finite time coefficients for the smallest available time increment above the ME time scale, i. e. $\tau = 2\tau_s$. The optimized coefficients are represented by the solid lines.

Table 5.1 shows the results of the optimization as well as the estimated errors by the MCEP method for the x and y components of the process. A graphical representation is depicted in Figures 5.6 and 5.7, respectively. A possible spatial dependence of the temperature due to the heating of the laser cannot be resolved on the basis of the experimental data. If one includes a quadratic term in the diffusion ansatz, $D^{(2)}(x) = \alpha + \beta x^2$, the error estimate for the parameter β is of the same size as the estimated value. However, the model with linear drift and constant diffusion describes the process very well, as we will see in Sect. 5.6.

The diffusion coefficients deviate by a factor of approximately 1.3 from the result that was expected from the Stokes-Einstein equation (see Sect. 5.2). To understand this deviation, also the diffusion coefficients of different freely diffusing particles are measured. The results are presented in the following section. The stiffness of the trap

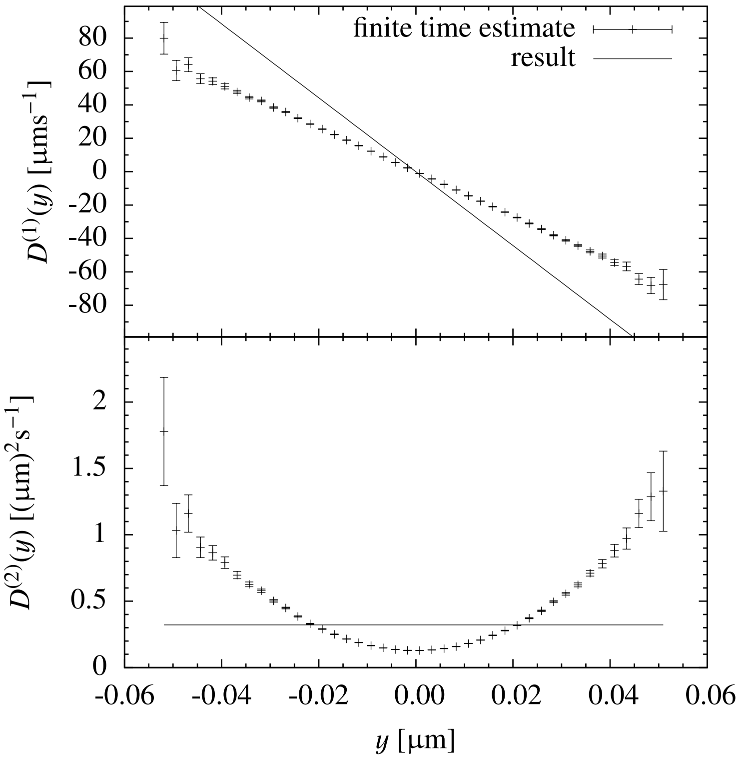

Fig. 5.7 Result of the optimization for drift (top) and diffusion (bottom) coefficients of the y coordinate of the particle motion. The representation is analogous to Fig. 5.6.

can nevertheless be calculated by

$$k = k_B T \frac{\gamma}{\alpha} \, . \tag{5.19}$$

Assuming a temperature of (294±2) K, one obtains

$$k_x = (24.72 \pm 0.27) \frac{\text{pN}}{\mu\text{m}} \, , \tag{5.20}$$

$$k_y = (27.85 \pm 0.31) \frac{\text{pN}}{\mu\text{m}} \, . \tag{5.21}$$

5.5 Diffusion coefficient of freely diffusing particles

In order to understand the deviations from the Einstein-Stokes equation, the diffusion coefficients for freely diffusing particles are determined. In the same manner as described in Sect. 5.1, the positions of seven different particles that are not trapped by optical tweezers are measured. For each particle, one time series with approximately 10^4 time steps at a sampling frequency of 3873 Hz is recorded. For these data we consider the mean squared displacement (MSD) for which the relation

$$\mathrm{MSD}(t) := \langle (x(t) - x(0))^2 \rangle = 2D^{(2)} t \tag{5.22}$$

holds. Figure 5.8 shows the obtained MSDs for the x components of the seven particles. The diffusion coefficients can be determined by linear fits. If one averages the determined coefficients over all particles and both coordinate directions, one obtains

$$D^{(2)} = (0.44 \pm 0.06)\ (\mu\mathrm{m})^2 \mathrm{s}^{-1}\,, \tag{5.23}$$

which is in good agreement to the expected result according to the Einstein-Stokes equation, Eq. (5.8). The reason for the higher standard deviation of $0.06\,(\mu\mathrm{m})^2\mathrm{s}^{-1}$ might be that the fluctuations among the particle radii are larger than indicated by the manufacturer. However, the low diffusion coefficient found in the optical trapping experiment is inside the range of fluctuations of diffusion coefficients among different particles.

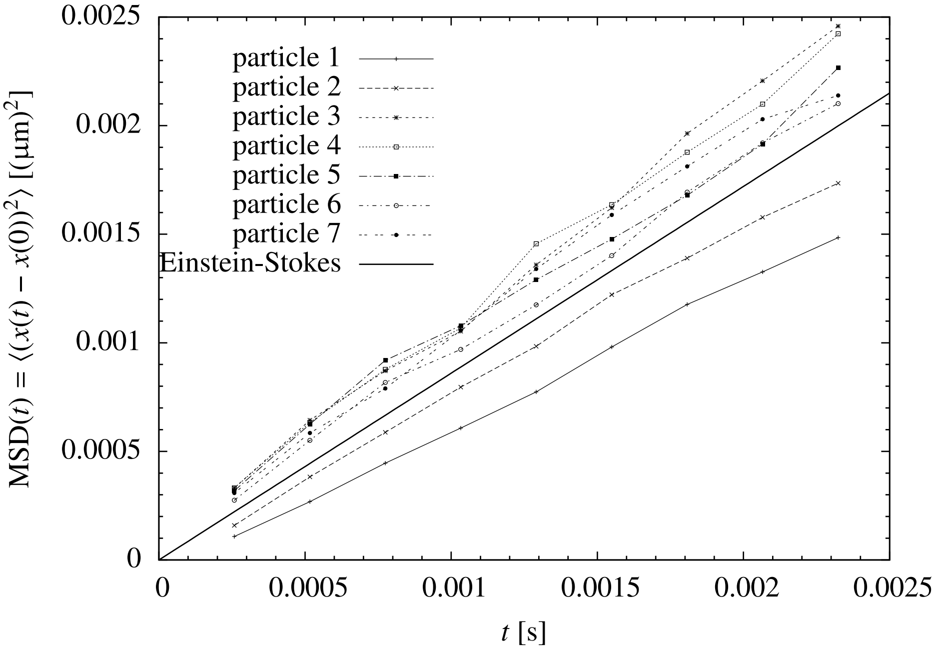

Fig. 5.8 Mean squared displacement of the x coordinate as a function of time for seven freely diffusing particles. The diffusion coefficient can be determined by a linear fit for each particle. The solid straight line shows the MSD that is expected according to the Einstein-Stokes equation, Eq. (5.8).

5.6 Comparison between model and data

In this section, a comparison between the estimated models and the experimental data is presented. At first we consider the single point PDFs. The PDFs of the experimental trajectories are estimated employing the Epanechnikov kernel (3.29) and a bandwidth according to (3.30). The PDFs according to the OU model are given by

$$f(x) = \sqrt{\frac{\gamma}{2\pi\alpha}} \exp\left(-\frac{\gamma}{2\alpha} x^2\right) . \tag{5.24}$$

Figure 5.9 shows the estimated PDFs from the experimental data in comparison to the ones from the model time series for the two processes. In both cases, the PDFs agree very well.

The second quantity under consideration is the ACF, Eqs. (5.15). Figure 5.10 shows the ACF of the experimental time series for the x and y components of the particle motion, together with the ACFs of our model that are given by

$$C(\tau) = \exp(-\gamma\tau) . \tag{5.25}$$

As one can also see in Fig. 5.4, the experimental ACFs are not exactly exponentially shaped. The reason for this small deviation lies probably in the hydrodynamic memory effects discussed in Sect. 5.2. However, one can see that the relaxation times of the models and the experimental data sets coincide very well.

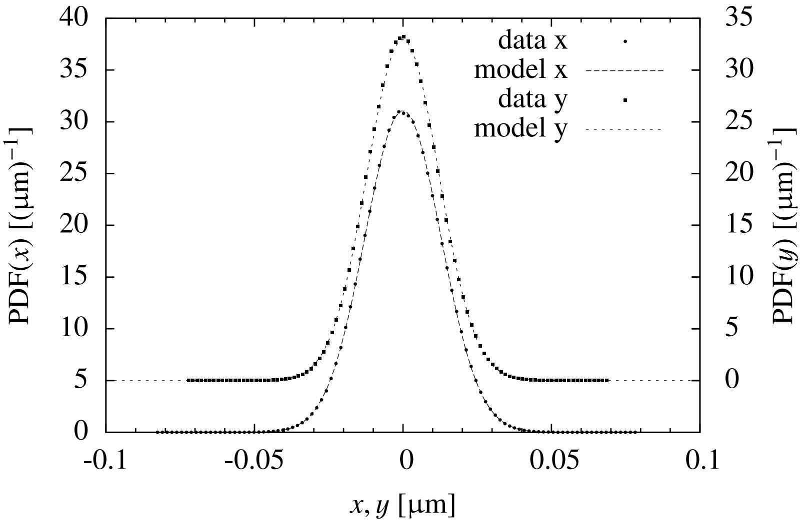

Fig. 5.9 Comparison between the PDFs of the experimental data set (kernel density estimate) and our model (Eq. (5.24)), for the x component (points and solid line, left vertical axis) and y component (squares and dashed line, right vertical axis) of the particle motion.

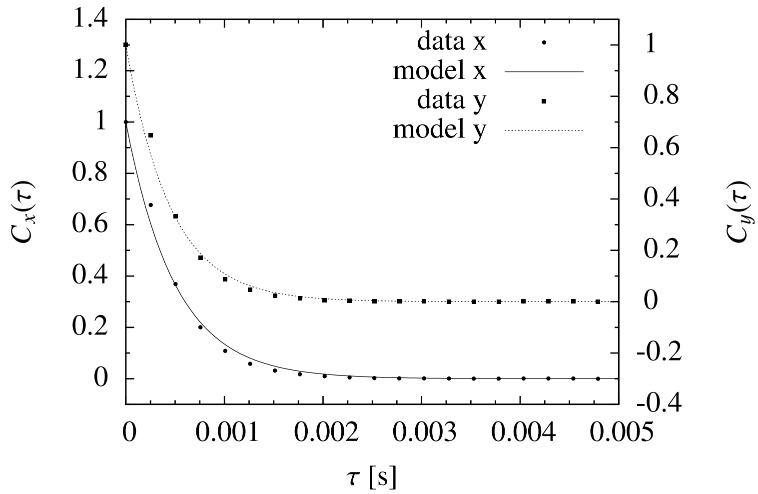

Fig. 5.10 Comparison between the measured ACFs of the data set and the ACF of the OU model, Eq. (5.25) for the x component (points and solid line, left vertical axis) and y component (squares and dashed line, right vertical axis) of the particle motion.

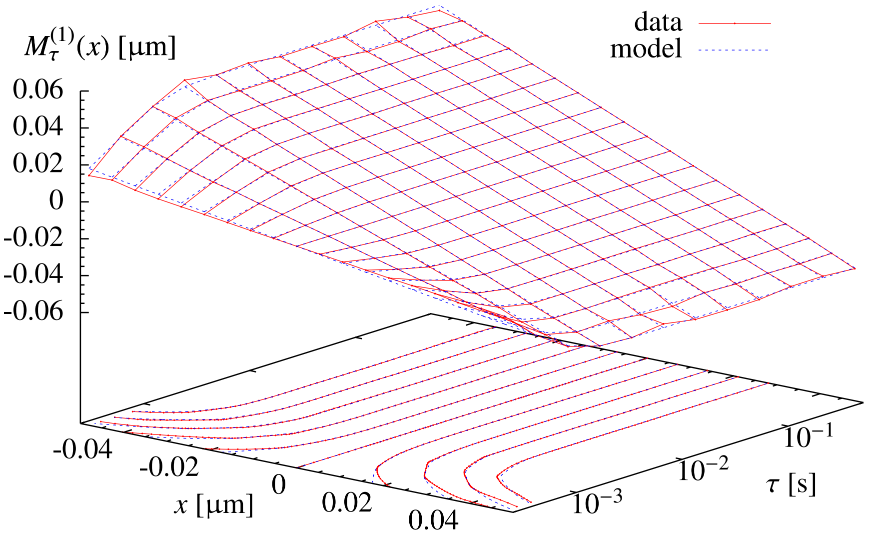

Fig. 5.11 Comparison between the first finite time conditional moment of the experimental data set (red solid lines) and the model reconstruction (blue dashed lines) for the x component of the particle motion.

As a next step, the first and second finite time conditional moments are compared. They are depicted in Figs. 5.11 and 5.12, respectively for the x component. The

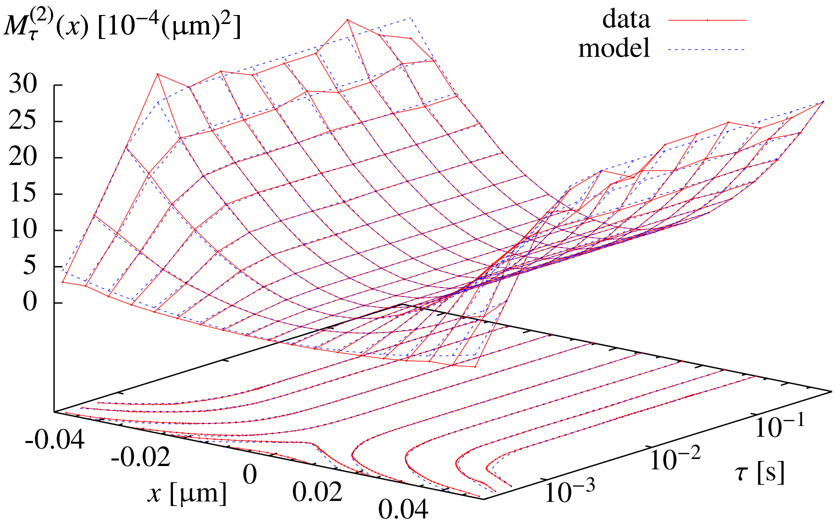

Fig. 5.12 Comparison between the second finite time conditional moment of the experimental data set (red solid lines) and the model reconstruction (blue dashed lines) for the x component of the particle motion.

corresponding figures for the y component are not shown, but they are qualitatively equal. The conditional moments of the OU model are given by

$$M_\tau^{(1)}(x) = -x\,(1 - \mathrm{e}^{-\gamma\tau})\ , \tag{5.26a}$$

$$M_\tau^{(2)}(x) = x^2\,(1 - \mathrm{e}^{-\gamma\tau})^2 + \frac{\alpha}{\gamma}\left(1 - \mathrm{e}^{-2\gamma\tau}\right)\ . \tag{5.26b}$$

Apparently, the model fits very well to the data. Significant deviations do only occur for the smallest $\tau = \tau_s$, which is below the ME time scale and was not included in the optimization. Here the slope (with respect to x) of the first moment and the second moment (for all x) of the data are smaller compared to the model. An inclusion of time increments below the ME time scale would therefore lead to underestimated drift and diffusion coefficients.

Instead of the fourth conditional moments, we regard the fourth finite time KM coefficient, which for our model reads

$$D_\tau^{(4)}(x) = \frac{1}{24\tau}\left[(1 - z_\tau)^4\,x^4 + 6\frac{\alpha}{\gamma}\left(1 - 2z_\tau + 2z_\tau^3 - z_\tau^4\right)x^2 + 3\left(\frac{\alpha}{\gamma}\right)^2\left(1 - z_\tau^2\right)^2\right]. \tag{5.27}$$

Here we have used the abbreviation $z_\tau = \mathrm{e}^{-\gamma\tau}$. Figure 5.13 shows the estimated fourth KM coefficient together with Eq. (5.27). As in the two previous plots, significant

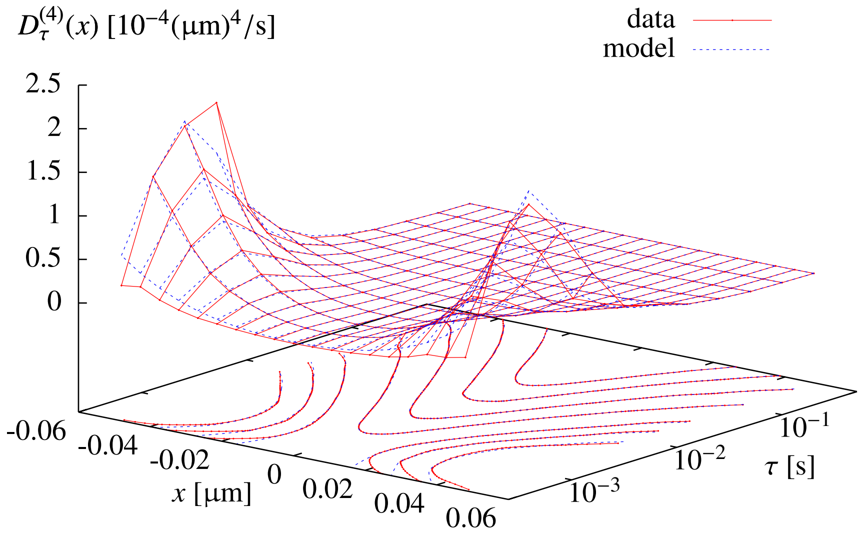

Fig. 5.13 Comparison between the fourth finite time KM coefficient of the data set (red solid lines) and the model reconstruction (blue dashed lines) for the x component of the particle motion.

deviations are only visible for the smallest $\tau = \tau_s$, where the coefficient estimated from data is smaller than in the model. However, one can see that $D_\tau^{(4)}(x)$ vanishes as τ approaches zero. This is the requirement for the Pawula theorem that guarantees that also the third and all higher KM coefficients vanish [Ris89].

6 Conclusion

The focus of the first part of this thesis is the problem of finite sampling interval effects in the KM analysis of stochastic time series. In Chap. 4, a method developed by Lade [Lad09] was presented that allows to make exact predictions of these effects for given drift and diffusion coefficients. With help of this method it was demonstrated that there are two limiting regimes in the space of the time increment τ separated by the relaxation time τ_R of the process. For $\tau \ll \tau_R$, finite time effects can be safely neglected; for $\tau \gg \tau_R$, all information about the true drift and diffusion coefficients is lost, and the KM analysis is impossible.

Furthermore, an optimization procedure was presented that was developed in the course of the current thesis [HF11, HFHD12]. It can be seen as an inversion of the method of Lade as its purpose is to deduce the correct KM coefficients from measured coefficients that suffer from finite time effects. In four examples with synthetic time series, which cover many important applications, it was demonstrated that the method works very well if the sampling interval is approximately of the same order of magnitude as the relaxation time. Even optimizations with more than 20 parameters were proven to be feasible.

In cases were analytic solutions of the AFPE are available, it is possible to calculate error estimates for the optimized parameters employing a MCEP approach, which increases the reliability of the obtained results. With help of these error estimates it is demonstrated how the KM analysis fails when the sampling interval approaches the limit of statistical independence discussed in Sect. 4.1.2. Unfortunately, the numerical effort of th MCEP approach becomes very large if the AFPE has to be solved numerically. Therefore, it has not been tested for those cases.

Chapter 5 describes an application of the method discussed in Chap. 4 to real-world stochastic data of an experiment where trajectories of Brownian particles trapped by an optical tweezers system were measured. The measured time series has a sampling interval of about half its relaxation time which leads to relevant finite time effects influencing the KM analysis. Furthermore, a ME time scale was found that is approximately equal to the relaxation time of the process. This can be explained by hydrodynamic memory effects that are still present on this time scale. The large ME time has the consequence that even if the trajectories of the particle were measured with a higher sampling frequency, finite time effects could not be reduced because time increments below the ME time scale must not be regarded in the KM analysis.

On time scales above the ME time scale, the process can almost perfectly be reconstructed by an OU process according to the classical overdamped Markov model of Brownian motion. The data quality does not allow to detect deviations from linearity in the drift term, which corresponds to the optical forces acting on the particle, or a spatial dependence of the diffusion one could expect because the laser heats up the fluid.

The size of the measured diffusion coefficient was found to be about 1.3 times smaller than the diffusion predicted by the Einstein-Stokes equation. For comparison, also trajectories of different freely diffusing particles were measured with a similar experimental setup. Averaged over all particles, the Einstein-Stokes equation was found to be valid. The fluctuations of diffusion constants among different particles, which can probably be traced back to fluctuations among particle radii, are large enough to explain the low diffusion found for the trapped particle.

From a technical point of view, the new method presented in Chap. 4 could be improved by employing a more sophisticated regression technique like local polynomial regression [HMSW04]. This technique can significantly reduce the bias at a given variance. It would also be worthwhile to pay more attention to the bandwidth selection problem, no matter whether the Nadaraya-Watson estimator or some other estimator is employed. This is especially important since the selected bandwidth influences the estimated MCEP errors: The larger the variance of the estimator, the larger the MCEP error. Since a bandwidth that is larger than optimal reduces the variance, it will lead to an underestimated MCEP error, which makes the results appear more reliable than they actually are, which of course is the general problem of too large bandwidths. Thus, as long as the bandwidth-selection problem is not solved in a satisfying manner, it is safer to use a rather smaller bandwidth.

In the method of Lade [Lad09], moments of the conditional PDF are calculated by solving the AFPE. Alternatively, one can compute the complete conditional PDF by solving the normal FPE. The problem is that this would involve a Dirac δ function as an initial condition, which is expected to cause numerical intricacies. A third way consists in simulating Langevin equations and measuring the conditional PDF from the resulting time series. An optimization based on the third way was presented by Kleinhans *et al.* [KFNP05, KF07]. A fourth way was recently introduced by Tang *et al.* [TAY13], who employ the short time propagator, Eq. (2.16), as an approximation for the conditional PDF instead. The advantage of the methods of Kleinhans and Tang as compared to the method presented here is that the information of the whole conditional PDF is used instead of only the first two moments. On the other hand, the method presented here uses information of conditional PDFs for several time increments, while the other two methods use only one. All three methods could be improved accordingly. In the method presented here one could also include higher moments in the least square potential (4.24). In the methods of Kleinhans and Tang the corresponding distance measures (the Kullback-Leibler divergence) that are minimized could be augmented by several conditional PDFs for different time increments.

A direct comparison between the performances of the different methods has not been drawn yet. Since the performances depend on many technical aspects, such as the employed density estimation or regression techniques as well as the bandwidth selection, an objective comparison is not trivial.

Since many interesting applications involve multivariate processes, a corresponding extension of the method would be of great value. However, this imposes two major problems. First, a multivariate extension requires the solution of several coupled AFPEs, which increases the computational complexity significantly. Second, multivariate regression requires a very good data quality. Therefore it is an open question whether or not such an extension would be worth the effort.

Part II

Pattern formation of microscopic fluid layers

7 Introduction

The second part of this thesis deals with a theoretical description of experiments [WDW$^+$11, WC12] in the field of organic semiconductors. Since researchers had first successes in producing conductive organic molecules and discovered electroluminescence in organic compounds in the 1950's [Ber55], organic semiconductors have become a large field of academic as well as industrial research [For04]. The interest in organic semiconductors stems from potential applications in organic light emitting diodes (OLEDs), solar cells, transistors, sensors, memories and so on. While the conductivity of the employed organic molecules is orders of magnitude below their inorganic counterparts (e. g., silicon), advantages are the lower costs, an enhanced flexibility and a reduced weight of the organic material. This allows one to create devices that one is not able to build with inorganic conductors. One example that is currently under development is a flexible full color display made of OLEDs that can be rolled up when not in use.

The technological challenges connected to the development of organic opto- and microelectronic devices are the chemical design of organic molecules for a specific purpose (e. g., charge transfer or emission of light) and the preparation of a (structured) thin film of this material on a substrate [For04]. While the former challenge is mainly a task for chemists, many physicists are concerned with the latter one. For inorganic conductors, photolithography is the most common technique for the device preparation allowing for the creation of patterns with minimal feature sizes of a few tens of nanometers [Del10]. Unfortunately, the various processing steps involved in photolithography would deteriorate the functionalities of complex organic molecules. Concerning the available methods for film preparation of organic devices, one has to distinguish between small molecules and polymers [For04].

For the preparation of a homogeneous polymer film, one usually uses a solution of the polymer in a volatile solvent. The solution can be transferred onto the substrate, e. g., by spraying techniques or spin coating. After or during the deposition of the solution, the solvent evaporates leaving a uniform layer of the polymer. For the preparation of structured films, the most common technique is ink-jet printing. Thereby, the substrate is prestructured with polymer walls that enclose a specific area that is afterwards filled with a polymer solution by a micrometer-scale nozzle. Employing this technique, full color polymer displays have already been manufactured, which are used in mobile phones and other small electronic devices. There is also a first OLED TV on the market that is produced by Sony [Son].

Regarding the preparation of thin films of small molecules, the most common technique is vacuum thermal evaporation (VTE), also referred to as organic molecular beam deposition (OMBD). Here, a probe of the organic substance is sublimed in an oven under ultrahigh vacuum conditions. The vaporized molecules are then deposited onto a cooled substrate via condensation. To create patterns of small organic molecules, one can put a shadow mask closely in front of the substrate [TBB+99]. Alternative methods include stamping [KBF00] and printing [AMFL08].

The experiments that are modeled in this thesis use another strategy, namely area-selective growth [WDZ+09]. Here, the deposition of small organic molecules is performed via OMBD, but the substrate is chemically structured before the deposition in such a way that the deposited molecules prefer to accumulate at specific sites. In the experiments described in [WDZ+09, WDB+10, WDW+11, WC12], SiO_2 substrates are prestructured with Au stripes or dots. For the deposited molecules it is energetically favorable to accumulate on the gold sites.

Since the experiments are conducted under ultra-high vacuum conditions, most of the organic molecules sublimate in the oven and resublimate on the cooled substrate surface without transition to the liquid phase. Only one employed molecule type, N,N'–di[(*N*-(3,6-di-*tert*-butyl-carbazyl))-*n*-decyl] quinacridone (DtCDQA), which is an orange light-emitting dye molecule [WDB+10], shows a liquid-like behavior on the substrate [WDW+11].

The aim of this part of the thesis is to provide a theoretical model that can reproduce the various structures (see Sect. 8.1) that are observed in experiments with DtCDQA and to understand which structures develop under which conditions.

Basically, there are three fundamentally different ways to model the system. One possibility is a description on the molecular scale. This means that one treats every single molecule of the substrate and the deposited material as one particle and establishes a specific form of interaction between these particles. A numerical simulation of such a model can either be done via Molecular Dynamics, i. e., integrating the equations of motion for every single molecule, or by kinetic Monte Carlo methods. In the latter, one starts with a specific configuration of the system and computes the total energy of all relevant interactions. Then one randomly chooses another test configuration and compares its energy with the energy of the previous configuration. If the new energy is lower than the old energy, the new configuration is typically accepted, otherwise it is only accepted with a specific probability, which depends on the temperature of the system and the energy difference. Repeating these steps, one slowly approaches an energetically optimal configuration of the system. This method has already been employed to model the experiments described above [LMW+12].

The other two approaches describe the layer of the deposited organic molecules as a continuum. In the case of a liquid film, a final configuration can be determined by minimizing the surface energy under specific constraints. Experiments with water [GHLL99] that show similar structures as observed in [WDW+11] were modeled employing this approach [LBD+05]. Similar systems were also studied in [BDP99, BD00, LL00, BL02, BHYM03].

A disadvantage of surface minimization techniques is that they are limited to the investigation of equilibrium configurations. Here, we choose a dynamical approach that is based on a thin film equation [ODB97, Thi10], which describes the temporal evolution of the height profile of a thin liquid film. On the one hand, the stability of equilibrium solutions of this equation is investigated employing continuation techniques, and on the other hand, the time evolution is studied by direct numerical simulations (DNSs). Similar stability analyses have been presented before in Refs. [TBBB03, MRD08], direct numerical simulations of similar systems are described in Refs. [KS01, SBK+12]. The relation of the analysis presented here to these articles is discussed in the concluding chapter at the end of this part of the thesis.

The overall outline of the second part is as follows. The next chapter presents a detailed description of the experimental findings and formulates the aims of the following investigation. Chapter 9 gives a summary of the derivation of the thin film equation followed by a chapter describing the employed numerical methods, namely DNS and numerical steady state continuation. The stability analysis is the topic of Chap. 11, results of the performed DNSs are presented in Chap. 12. The last chapter presents a summary and discussion of the results.

8 Experiments and motivation for theoretical modeling

This chapter provides a description of some results of the experiments conducted by Wang and coworkers [WDW⁺11, WC12]. Based on these experiments, the motivation and goals for a theoretical description are outlined.

8.1 Description of experimental results

The top left panel of Fig. 8.1 shows an atomic force microscopy (AFM) image of DtCDQA molecules deposited by OMBD on a SiO_2 surface prepatterned with Au stripes. The width of the stripes varies from 0.3 to 2.3 µm. One can identify three different morphologies that the DtCDQA film develops. On the bare substrate without gold stripes one can see small circular droplets with a diameter of 2 to 3 µm. Cross-sectional profiles (cf. top right and bottom panels of Fig. 8.1) reveal a spherical cap shape of the droplets. The second type of morphologies are cylindrical ridges centered on the gold stripes. At some positions the ridges break up and form bulges that also partly cover the SiO_2 substrate. These bulges are the third type of morphologies.

By evaluating cross-sectional profiles of AFM images, one can measure the contact angles that are assumed by the different morphologies (cf. Fig 8.1). This yields $\Theta_{\mathrm{drop}} = 20.6°$, $\Theta_{\mathrm{rid}} = 12.3°$ and $\Theta_{\mathrm{bulg}} = 20.0°$ for drops, ridges and bulges, respectively . The latter two contact angles were measured in a direction perpendicular to the Au lines.

Figure 8.2 (c) shows sketches of different equilibrium morphologies that are observed when different amounts of molecules are deposited. Panels (a) and (b) show examples of AFM images for very small amounts of deposited molecules. In this case small droplets form on the Au stripes. With increasing amount of molecules on the substrate, the droplets grow until they reach the boundaries of the stripe and elongate afterwards until the whole stripe is covered with a cylindrical ridge. If more molecules are added, at some point bulges form that enter the bare SiO_2 substrate. Under some conditions that were not studied experimentally in detail, bulges can also form while the gold stripe is not entirely covered with DtCDQA. A corresponding AFM image is shown in panel (d).

The height of the ridges seen in Fig. 8.1 is found to increase with the width of the

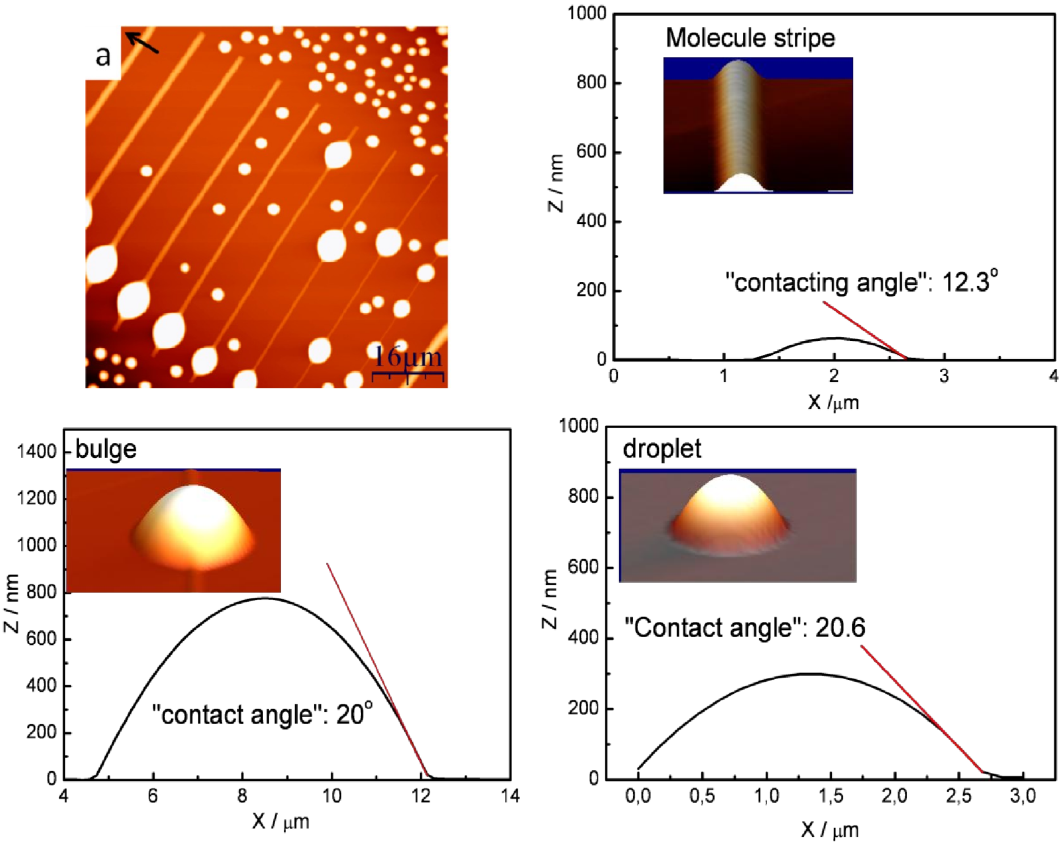

Fig. 8.1 Top left: AFM image of DtCDQA molecules deposited on a SiO_2 substrate patterned with Au stripes. The width of the Au stripes is increasing from right to left from 0.3 µm to 2.3 µm. The mean film thickness is 50 nm. Since the diameter of one molecule is about 1 nm, this corresponds to roughly 50 monolayers. Picture reproduced from [WC12]. The other panels show cross-sectional profiles of the three different morphologies. The inlets show corresponding three-dimensional AFM images. The latter three pictures are reproduced from [WDW^{+}11].

Au stripes. This is a typical capillarity effect that is also seen in other experiments with liquids on chemically striped surfaces [GHLL99, DTMW00]. The opposite behavior is observed if instead of DtCDQA, *N*, *N*′-bis(1-naphyl)-*N*, *N*′-diphenyl-1,1′-biphenyl-4,4′-diamine (NPB), a blue-light-emitting small organic molecule, is deposited. As can be seen in Fig. 8.3, the height of NPB ridges on Au stripes is decreasing with increasing stripe width.

Another evidence that DtCDQA is melted and NPB is sublimated is given by photographies of the materials before and after heating in the crucibles. Before the heating, both materials are in the powder state, after the heating only NPB is. For DtCDQA one has a clear indication that it was evaporated from the liquid state as one observes droplets of condensating material on the wall of the crucible.

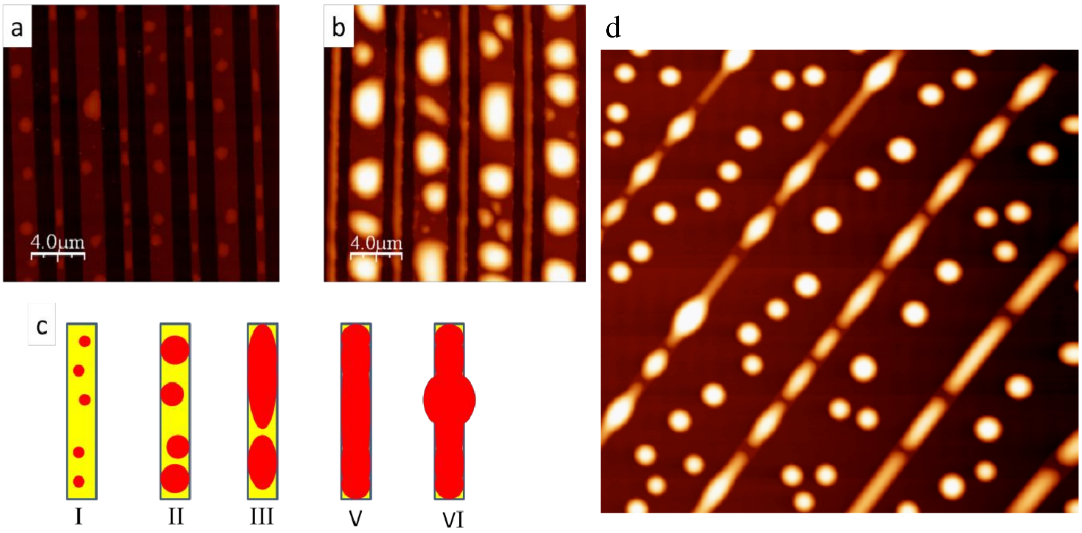

Fig. 8.2 Different equilibrium morphologies that develop after deposition of DtCDQA molecules on SiO_2 substrates patterned with Au stripes. Panels (a) and (b) show AFM images of 3 nm and 10 nm mean deposit height of DtCDQA, respectively. Panel (c) shows sketches of the different equilibrium morphologies. For small amounts of deposited molecules, small droplets form on the Au lines (I). With increasing amount, the droplets grow until they reach the borders of the stripe (II) and elongate afterwards (III). Finally, the whole stripe is covered with a cylindrical ridge (V). At a certain amount of molecules, bulges form that also cover the bare SiO_2 substrate (VI). Panel (d) shows an AFM image of 200 nm DtCDQA on a substrate with gold stripes of widths from 1.1 to 1.9 μm. Here, bulges form whereas the gold stripes are not entirely covered, which corresponds to another growth regime not sketched in panel (c). Pictures (a), (b) and (c) are reproduced from [WDW⁺11], picture (d) is reproduced from [Mue12].

8.2 Motivation

The purpose of the experiments is to create patterns of the deposited small organic molecules that image the prestructure of the substrate. The desired morphologies are therefore regular ridges centered on the Au stripes without any bulges. There are two, in this sense unwanted, instabilities that destroy the regular ridges. One is the formation of bulges that is observed to occur when too much material is deposited for a given stripe geometry. The second instability is the formation of droplets on the Au stripe such that not the entire stripe is covered with the deposited material. This instability occurs if not enough material is deposited for a given stripe geometry.

Reference [LMW⁺12] provides a theoretical description of the experiments on the molecular level employing kinetic Monte Carlo simulations. In this work, the different morphologies that are observed in the experiments can be reproduced by varying the interaction strength of the involved molecules. This is in some sense not satisfying

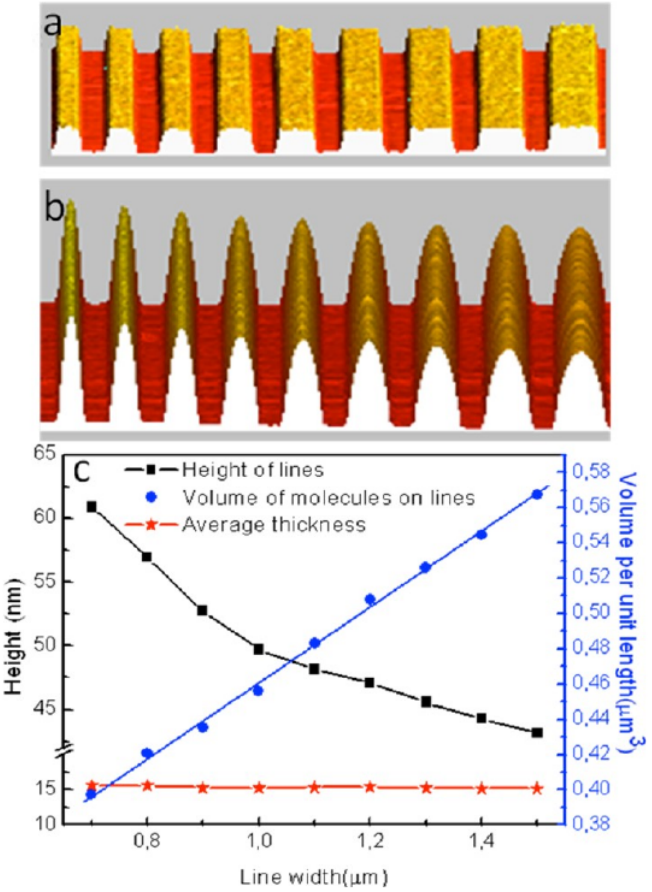

Fig. 8.3 a) AFM image of Au stripes with increasing width from left to right from 700 nm to 1.5 μm. (b) Same figure after deposition of NPB. (c) Height of the ridges, volume per unit length and average film thickness against the width of the Au stripes. Picture taken from [WC12].

because in the experiments all morphologies are observed for the same interactions. Only the geometry of the chemical pattern and the amount of deposited molecules is altered.

In this part of the thesis we set up a continuum model in form of a PDE (see Sect. 9.1) that allows for the study of the two instabilities mentioned above. For a PDE more mathematical analysis methods can be employed than for an agent-based model as the one used in Ref. [LMW$^+$12]. One of these methods, numerical continuation (cf. Chap. 10), allows us to investigate the dependence of the instability thresholds on the various system parameters in an elegant way, without the need of tremendous computational efforts.

9 Theoretical description of the dynamics of microscopic fluid layers

9.1 The thin film equation

We consider a two-dimensional layer of a Newtonian, incompressible, non-volatile fluid bounded below by an impermeable wall at $z = 0$ and above by an interface between the fluid and a gas at $z = h(x, t)$ (cf. Fig. 9.1). In the x direction the system is considered to be infinitely large. We denote the horizontal component of the velocity field by u and the vertical component by w. The dynamics of the velocity field is given by the Navier-Stokes equation and the continuity condition for an incompressible fluid [Dav04]:

$$\rho(\partial_t u + u\partial_x u + w\partial_z u) = -\partial_x p + \eta\Delta u \tag{9.1a}$$

$$\rho(\partial_t w + u\partial_x w + w\partial_z w) = -\partial_z p + \eta\Delta w \tag{9.1b}$$

$$\partial_x u + \partial_z w = 0 \tag{9.1c}$$

with $\Delta = \partial_x^2 + \partial_z^2$. Here, ρ denotes the fluid density, p is the local pressure, and η is the viscosity. Since we are interested in systems with typical mean film heights below 100 nm on horizontal substrates, we can safely neglect gravity [BEI$^+$09].

At the bottom, the typical boundary conditions are no slip and no penetration, i. e., $u(z = 0) = 0$, $w(z = 0) = 0$. The former boundary condition is sometimes replaced by allowing for a microscopic slip length to deal with the problem of the contact line singularity, which is discussed in Sect. 9.2. The boundary conditions at the fluid-gas interface at $z = h(x, t)$ are

$$\partial_t h = w - u\partial_x h \qquad \text{kinematic boundary condition,} \tag{9.2}$$

$$\mathbf{T} \cdot \hat{\boldsymbol{n}} = (\Pi + \gamma\kappa)\hat{\boldsymbol{n}} \qquad \text{force equilibrium.} \tag{9.3}$$

In the last equation,

$$\hat{\boldsymbol{n}} = \frac{1}{\sqrt{1 + (\partial_x h)^2}} \begin{pmatrix} -\partial_x h \\ 1 \end{pmatrix} \tag{9.4}$$

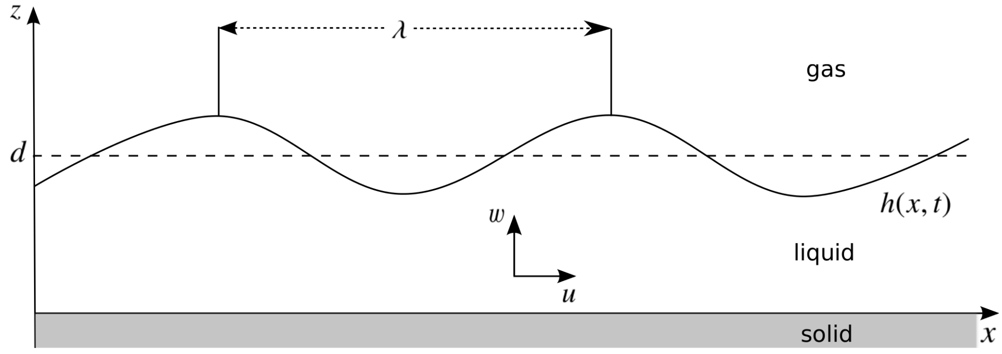

Fig. 9.1 Sketch of a two-dimensional liquid film with height profile $h(x,t)$ bounded below by an impermeable wall and above by a gas. u and w denote the horizontal and vertical components of the fluid velocity field, respectively. The long-wave approximation requires that a typical lateral length λ of the height profile pattern is large as compared to the characteristic film height d.

is the unit vector normal to the interface (pointing outward of the fluid), $\mathbf{T}$ is the stress tensor of the fluid, γ is its surface tension, and κ is the mean curvature of the interface. Π denotes the *disjoining pressure* (DP) and models the intermolecular interactions between fluid and substrate molecules, which determine the wettability. It is described in more detail in Sect. 9.3. Equation (9.2) identifies the vertical velocity of the interface with the fluid velocity at the interface. This relation has to be modified for volatile fluids. Equation (9.4) states that stresses at the interface are balanced.

The next step is to perform the *long-wave approximation*. The latter requires that the ratio $\varepsilon = \lambda/d$ between the characteristic lateral length λ of a pattern of the height profile and the characteristic film height d is small, i. e., $\varepsilon \ll 1$. Expanding the non-dimensionalized equations w. r. t. ε keeping only the lowest order and performing some further calculations described in [ODB97] and [GMR06], one can derive the thin film equation (in dimensional variables)

$$\partial_t h = \partial_x[Q\partial_x P]\,. \tag{9.5}$$

For a two-dimensional surface, the thin film equation reads

$$\partial_t h = \nabla\cdot[Q\nabla P]\,, \tag{9.6}$$

with $\nabla = (\partial_x, \partial_y)^T$. Here, $Q(h)$ is the mobility term with

$$Q(h) = h^3/(3\eta)\,, \tag{9.7}$$

and P is the generalized pressure which is given by the sum of the Laplace pressure and the DP:

$$P = -\gamma\Delta h - \Pi\,. \tag{9.8}$$

Now, $\Delta = \partial_x^2 + \partial_y^2$ in contrast to the definition used in Eq. (9.1). The DP depends on h and can also depend explicitly on x and y if the substrate is chemically or topographically inhomogeneous[1]. Its explicit form is discussed in the next section.

The thin film equation is a PDE of fourth order in space. It is nonlinear in h because of the nonlinear mobility term and the nonlinear dependence of the DP on h (cf. Sect. 9.3). These properties result in some difficulties concerning numerical simulations, which are discussed in Sect. 10.2.

With the free energy functional

$$F[h] = \int \mathrm{d}A \left[\frac{\gamma}{2}(\nabla h)^2 + \phi(h)\right] \tag{9.9}$$

the thin film equation (9.6) can also be expressed as a gradient dynamics [Thi11]

$$\partial_t h = \nabla \cdot \left[Q\,\nabla \frac{\delta F}{\delta h}\right]. \tag{9.10}$$

The first term of the integrand in Eq. (9.9) is derived from the energy of the free surface

$$F_S = \gamma \int \mathrm{d}S\,, \tag{9.11}$$

where S denotes curved surface coordinates. Transformation to Cartesian coordinates yields

$$F_S = \gamma \int \sqrt{1 + |\nabla h|^2}\,\mathrm{d}A \tag{9.12}$$

$$\approx \gamma \int (1 + \tfrac{1}{2}|\nabla h|^2)\,\mathrm{d}A\,. \tag{9.13}$$

The constant term can be ignored since only derivatives of the energy enter the dynamic equation. The second term in the integrand of Eq. (9.9) corresponds to the wettability of the substrate. It is related to the DP as shown in Sect. 9.3. The free energy functional does also play the role of a Lyapunov functional as we will demonstrate in the following.

The total time derivative of the free energy is given by

$$\frac{\mathrm{d}F}{\mathrm{d}t} = \int \mathrm{d}A\, \frac{\delta F}{\delta h}\,\frac{\mathrm{d}h}{\mathrm{d}t}\,. \tag{9.14}$$

Insertion of Eq. (9.10) and a subsequent partial integration yields

$$\frac{\mathrm{d}F}{\mathrm{d}t} = \int \mathrm{d}A\, \frac{\delta F}{\delta h}\,\nabla \cdot \left[Q\,\nabla \frac{\delta F}{\delta h}\right] \tag{9.15}$$

$$= -\int \mathrm{d}A\, Q \left(\nabla \frac{\delta F}{\delta h}\right)^2\,. \tag{9.16}$$

As Q is always positive, the final expression is negative, i. e., F is a Lyapunov functional. As a consequence, equilibrium solutions of the thin film equation correspond to local extrema or saddle points of the free energy functional F.

---

[1] A topographical inhomogeneity would also enter the mobility term Q.

9.2 The contact line singularity

The introduced hydrodynamic model with the no-slip boundary condition at the substrate leads to a singularity in the case of a moving three-phase contact line, where the three phases vapor, liquid and solid meet. This problem was pointed out for the first time by Huh and Scriven in [HS71]. As outlined in [BEI⁺09], the singularity can be demonstrated as follows.

Consider the contact line of a drop that moves with a velocity U to the left along a surface. For the purpose of an easier imagination we can also consider the contact line as stationary and the substrate moving with velocity U to the right, as illustrated in Fig. 9.2. If the fluid obeys the no-slip boundary condition, the horizontal velocity u of the fluid at the boundary is also U, i. e., $u(x, z = 0) = U$. At a position x close to the contact line, the velocity gradient can be approximated by $\mathrm{d}u/\mathrm{d}z \approx U/h(x)$ and $h(x) \approx \Theta x$ for a small contact angle Θ. The viscous dissipation rate per unit volume can be approximated by

$$\varepsilon_{\mathrm{visc}} \approx \eta \left(\frac{\mathrm{d}u}{\mathrm{d}z}\right)^2 \approx \eta \left(\frac{U}{h}\right)^2 \approx \eta \left(\frac{U}{\Theta x}\right)^2 \tag{9.17}$$

Next, we can estimate the dissipation per unit time and unit length of the contact line by

$$D_{\mathrm{visc}} \approx \int_0^L \varepsilon_{\mathrm{visc}} h \, \mathrm{d}x \propto \int_0^L \frac{1}{x} \, \mathrm{d}x\,, \tag{9.18}$$

which diverges logarithmically.

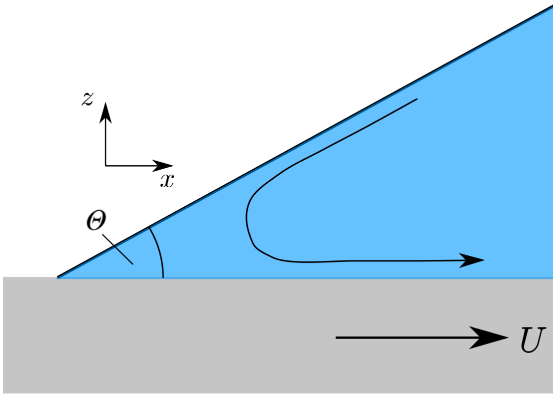

Fig. 9.2 Sketch for the illustration of the contact line singularity. A static contact line with contact angle Θ is considered on top of a substrate that moves with velocity U in positive x direction. The arrow in the fluid illustrates a typical stream line.

The difficulty in the modeling of the contact line region stems from the fact that microscopic influences on the molecular scale play a role, but one still needs a description based on macroscopic hydrodynamics. There are different possibilities to overcome this problem. One is to replace the no-slip boundary condition by the Navier boundary condition $u(z = 0) = b\partial_z u|_{z=0}$ [RD08] that takes into account that the fluid molecules can move along the substrate surface. Here, the parameter b has the physical dimension of a length and is called the slip length. This boundary condition leads to an amended mobility coefficient

$$Q(h) = \frac{1}{\eta}\left(h^3/3 - bh^2\right) . \tag{9.19}$$

The no-slip boundary condition corresponds to $b = 0$.

Depending on the interactions between fluid and substrate molecules, sometimes a thin precursor film exists in front of the contact line, which has a typical thickness between one molecular monolayer and 10 nm [BEI$^+$09]. In this case one can circumvent the contact line problem by only considering regions that are covered either by the precursor film or by a macroscopic fluid layer. This is the approach we choose in this work. In our model based on the lubrication approximation and an effective DP, the height of a precursor film coexisting with a macroscopic drop corresponds to the zero in the DP, which is discussed in the next section.

9.3 The disjoining pressure

The DP was introduced in 1940 by Derjaguin [Der40] and is therefore also referred to as the *Derjaguin pressure*. Modeling the intermolecular interactions among the molecules of the liquid as well as between liquid and substrate molecules, it becomes relevant for films with typical film heights below 100 nm [SV09, Isr11, dG85]. The DP is related to the *effective interface potential* (EIP) ϕ by

$$\Pi(h) = -\frac{\partial\phi(h)}{\partial h} \tag{9.20}$$

The EIP is the energy per unit area that is necessary to maintain a wetting film of height h [RD08]. Figure 9.3 shows a typical form of an EIP together with the corresponding DP. The qualitative form stems from the sum of long-range repulsive forces that have a destabilizing effect on flat films and short-range attractive forces that tend to stabilize a flat film. The position of the minimum of the EIP (the zero of the DP) corresponds to the precursor film height h_p which is assumed between droplets of a partially wetting liquid. The value of the minimum of the EIP ϕ_{min} is connected to the equilibrium contact angle Θ_{eq} via the Young-Laplace equation [RD08]

$$\cos\Theta_{\mathrm{eq}} = 1 + \frac{\phi_{\mathrm{min}}}{\gamma} . \tag{9.21}$$

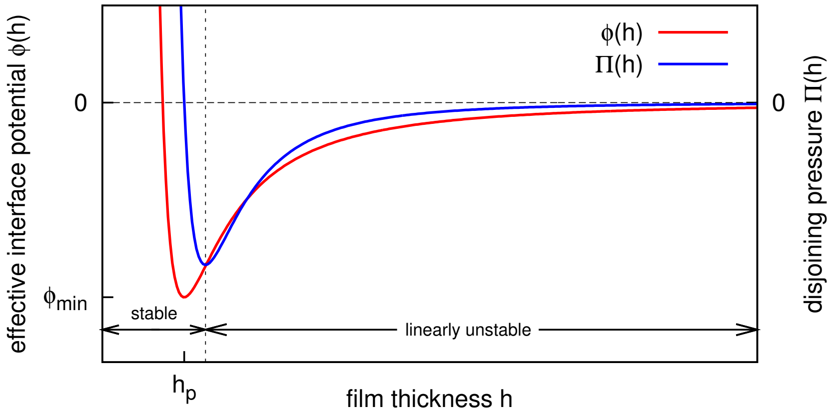

Fig. 9.3 Sketch of a typical EIP $\phi(h)$ and the corresponding DP $\Pi(h) = -\phi'(h)$. The position of the minimum of the EIP corresponds to the precursor film height h_p, its value ϕ_{min} determines the equilibrium contact angle (cf. Eq. (9.21)). A linear stability analysis of the thin film equation (9.6) reveals that a flat film solution of height $\bar{h}$ is stable if $\phi''(\bar{h}) > 0$ or, equivalently, $\Pi'(\bar{h}) < 0$. Otherwise it is unstable and subject to spinodal dewetting. At larger film heights the influence of the DP vanishes. Finally, thicker flat films are stabilized again by gravity.

Here, γ is again the surface tension.

A linear stability analysis of Eq. (9.6) (cf. Sect. 9.5) reveals that a flat film of height $\bar{h}$ is linearly stable (unstable) if $\phi''(\bar{h}) > 0$ ($\phi''(\bar{h}) < 0$), or, equivalently, $\Pi'(\bar{h}) < 0$ ($\Pi'(\bar{h}) > 0$). A linearly unstable flat film will break up and form droplets in the case of low film heights or holes in the case of larger film heights [SK98]. This instability is referred to as *spinodal dewetting* because of its mathematical resemblance to the spinodal decomposition of a mixture of two solids or fluids [Mit93]. For further increasing film heights, the influence of the DP becomes negligible and flat films are eventually stabilized by gravity.

Concerning the concrete form of the DP, many different functions are discussed in the literature [ODB97, dG85, SV09, Isr11]. However, for the qualitative behavior of a thin film, the exact form of the DP is not crucial.

9.4 The specific model

In this work we use the DP

$$\Pi(h,x) = \left(-\frac{A}{h^3} + \frac{B}{h^6}\right)(1 + \rho g(x)), \tag{9.22}$$

which corresponds to the EIP

$$\phi(h,x) = \left(-\frac{A}{2h^2} + \frac{B}{5h^5}\right)(1 + \rho g(x)). \tag{9.23}$$

The first, h-dependent factor is the one proposed in [Pis02]. The second, x-dependent factor takes into account the chemical stripe pattern of the substrate in the experiments. With this kind of spatial modulation, the height of the precursor film h_p is kept constant, and only the equilibrium contact angle, i. e. the wettability, is x-dependent. The dimensionless parameter ρ models the strength of the wettability contrast. The function $g(x)$ is periodic in x and describes the geometry of the stripe pattern.

For the numerical treatment we further non-dimensionalize Eq. (9.6) with Eqs. (9.7), (9.8) and (9.22) by introducing non-dimensional variables $\tilde{h}$, $\tilde{x}$, $\tilde{y}$, $\tilde{t}$ and $\tilde{\phi}$ with

$$\begin{aligned} t &= \tau\tilde{t}\,, & x &= L\tilde{x}\,, & y &= L\tilde{y}\,, \\ h &= d\tilde{h}\,, & \phi &= \kappa\tilde{\phi}\,. \end{aligned}$$

The scaling coefficients are chosen as

$$\begin{aligned} d &= h_p = \left(\frac{B}{A}\right)^{1/3}\,, & L &= \sqrt{\frac{\gamma}{A}}d^2\,, \\ \kappa &= \frac{A}{d^2}\,, & \tau &= \frac{3\eta L^2}{\kappa d}\,. \end{aligned}$$

The chosen scaling coefficient d corresponds to the precursor film height h_p, i. e., in non-dimensional units we have $h_p = 1$. Dropping the tilde, our final equation in non-dimensional units reads

$$\partial_t h = -\nabla\cdot\left\{Q(h)\nabla\left[\Delta h + \underbrace{\left(\frac{1}{h^6}-\frac{1}{h^3}\right)(1+\rho g(x))}_{\Pi(h,x)}\right]\right\}, \tag{9.24}$$

with $Q(h) = h^3$ (in Chaps. 11 and 12 also a mobility coefficients $Q(h) = h$ is considered). In the later analyses we use periodic boundary conditions in x and y direction.

In our model we ignore the process of condensation and assume that all material is deposited instantaneously, forming an initial homogeneous layer. The effect of continuing condensation has to be studied in the future.

In the next section we perform a linear stability analysis of the steady flat film solution of Eq. (9.24) for the homogeneous case with $\rho = 0$. Chapter 11 presents an analysis of the stability of steady ridge solutions for the inhomogeneous case. Finally, Chap. 12 provides results of DNSs of Eq. (9.24).

9.5 Linear stability analysis of a flat film on a homogeneous substrate

In this section we study the linear stability of the steady flat film solution of height $\bar{h}$ of the one-dimensional version of Eq. (9.24) for a homogeneous substrate ($\rho = 0$). The analyzed equation reads

$$\partial_t h = -\partial_x[h^3\partial_x(\partial_x^2 h + \Pi(h))]\,. \tag{9.25}$$

We plug in the ansatz

$$h(x,t) = \bar{h} + \eta(x,t) \tag{9.26}$$

where $\eta(x,t)$ is a small perturbation of a flat film of height $\bar{h}$. This leads to

$$\begin{aligned}\partial_t\eta &= -\,\partial_x\,[(\bar{h}+\eta)^3\,\partial_x\,(\eta_{xx} + \Pi(\bar{h}+\eta))]\\ &= -\,\partial_x\,[(\bar{h}+\eta)^3\,(\eta_{xxx} + \Pi'(\bar{h}+\eta)\,\eta_x)]\\ &= -\,3(\bar{h}+\eta)^2\,\eta_x\,[\eta_{xxx} + \Pi'(\bar{h}+\eta)\,\eta_x]\\ &\quad -(\bar{h}+\eta)^3\left[\eta_{xxxx} + \Pi''(\bar{h}+\eta)(\eta_x)^2 + \Pi'(\bar{h}+\eta)\eta_{xx}\right],\end{aligned} \tag{9.27}$$

where the indices of η denote derivatives with respect to the index and the primes of the DP denote derivatives with respect to its argument keeping x constant. Next, we expand the right hand side (RHS) of (9.27) w. r. t. η, keeping only the linear terms. For this, we need the expansions of the derivatives of the DP,

$$\Pi'(\bar{h}+\eta) = \Pi'(\bar{h}) + \eta\Pi''(\bar{h}) + O(\eta^2)\,, \tag{9.28}$$

$$\Pi''(\bar{h}+\eta) = \Pi''(\bar{h}) + \eta\Pi'''(\bar{h}) + O(\eta^2)\,, \tag{9.29}$$

and end up with

$$\partial_t\eta \simeq -\bar{h}^3[\eta_{xxxx} + \Pi'(\bar{h})\eta_{xx}]\,. \tag{9.30}$$

As perturbations, we allow for harmonic modulations in x with a wavenumber k that may grow or decay exponentially with a growth rate β:

$$\eta(x,t) = \mathrm{e}^{\beta t + \mathrm{i}kx}\,. \tag{9.31}$$

Since the thin film equation can be represented as a gradient dynamics (cf. Sect. 9.1), the growth rate β has to be real-valued. This can also be seen from the operator of the RHS of Eq. (9.30). It only consists of even derivatives and is therefore self-adjoint. Inserting (9.31) into (9.30), we obtain the dispersion relation

$$\beta(k) = -\bar{h}^3[k^4 - \Pi'(\bar{h})k^2]\,. \tag{9.32}$$

We notice that β can become positive if and only if $\Pi'(\bar{h}) > 0$. In this case, there exists a band of wavenumbers $0 < k < k_c = \sqrt{\Pi'(\bar{h})}$ with $\beta(k) > 0$. The fastest growing wavenumber is given by

$$k_{\max} = \sqrt{\frac{1}{2}\Pi'(\bar{h})} = \frac{1}{\sqrt{2}}k_c \tag{9.33}$$

and the corresponding maximal growth rate reads

$$\beta_{\max} = \beta(k_{\max}) = \frac{1}{4}\bar{h}^3(\Pi'(\bar{h}))^2 \,. \tag{9.34}$$

For $k = 0$, the growth rate β is always zero corresponding to volume conservation. Figure 9.4 shows a sketch of the dispersion relation for the unstable (solid curve) and stable (dashed curve) case.

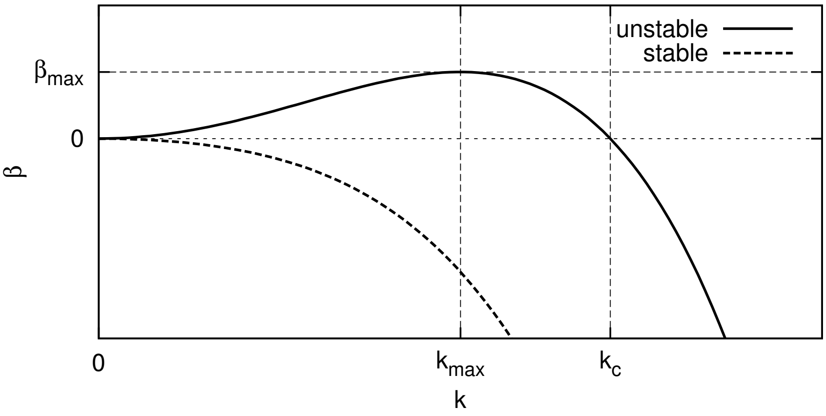

Fig. 9.4 Sketch of the dispersion relation, Eq. (9.32). For $\Pi'(\bar{h}) > 0$ a band of unstable wavenumbers $0 < k < k_c$ with $\beta(k) > 0$ exists (solid curve). For $\Pi'(\bar{h}) < 0, \beta(k) \leq 0\ \forall k$ (dashed curve) and the flat film is linearly stable.

For $\rho = 0$ the DP employed in this work reads

$$\Pi(h) = \left(\frac{1}{h^6} - \frac{1}{h^3}\right) \tag{9.35}$$

$$\Rightarrow \Pi'(h) = \left(-\frac{6}{h^7} + \frac{3}{h^4}\right) . \tag{9.36}$$

Therefore, spinodal dewetting occurs for mean film heights

$$\bar{h} > \bar{h}_c = 2^{1/3} \approx 1.26 \,. \tag{9.37}$$

For an inhomogeneous DP ($\rho \neq 0$), a flat film is no longer a steady solution of the thin film equation because then the RHS of Eq. (9.25) reads for $h = \bar{h}$

$$\mathrm{RHS} = -\bar{h}^3 \partial_x^2 \Pi(\bar{h}, x) \tag{9.38}$$

$$= -\bar{h}^3 \left(\frac{1}{\bar{h}^6} - \frac{1}{\bar{h}^3}\right) \rho g''(x) \neq 0 \,. \tag{9.39}$$

Therefore, chemical inhomogeneities can lead to dewetting even if an initial flat film is spinodally stable on every point of the substrate. This instability called *heterogeneous dewetting* was studied both experimentally and theoretically, e. g., in Refs. [HFS$^+$00] and [KKS00a, KKS00b], respectively. It is found that the time scales of heterogeneous dewetting are usually much smaller as compared to spinodal dewetting. Depending on the geometry of chemical inhomogeneities, very regular structures can emerge.

10 Numerical Approach

In this chapter we briefly illustrate two numerical methods that are employed in our analysis, namely steady state continuation and DNSs of a PDE. The first method is a powerful tool to perform bifurcation analyses, i. e., to study equilibrium solutions of nonlinear dynamical systems. The latter is used to compute concrete trajectories in time, i. e., to study the dynamics.

10.1 Continuation

In the analysis presented in Chap. 11, we employ the continuation software package AUTO-07p. In this section we confine ourselves to illustrate only the basic concept of continuation (Sect. 10.1.1) and to mention some features of AUTO-07p that are important for our applications (Sect. 10.1.2), without explaining the underlying mathematics in detail. For a more comprehensive description we refer the reader to the manual of the software [DO13] and to the lecture notes of Eusebius Doedel [Doe], who is one of the main developers of AUTO-07p.

10.1.1 Basic concept

To introduce the basic concept of continuation, we consider a dynamical system

$$\dot{\boldsymbol{x}} = \boldsymbol{F}(\boldsymbol{x}, \boldsymbol{\alpha}) \tag{10.1}$$

with $\boldsymbol{x}, \boldsymbol{F} \in \mathbb{R}^n$. The vector $\boldsymbol{\alpha} \in \mathbb{R}^p$ contains some constant parameters of the system. Let us assume that we know that $\boldsymbol{x}_0$ is a fixed point for a specific set of parameters $\boldsymbol{\alpha}_0$, i. e.

$$\boldsymbol{F}(\boldsymbol{x}_0, \boldsymbol{\alpha}_0) = 0\,. \tag{10.2}$$

Let us further assume that the Jacobian of the vector field $\boldsymbol{F}$ at $\boldsymbol{x}_0$, i. e. $\left\{\frac{\partial F_i}{\partial x_j}(\boldsymbol{x}_0, \boldsymbol{\alpha}_0)\right\}$, is invertible. Then the implicit function theorem (see any basic calculus textbook like

[CJ08]) guarantees that there exists a vicinity $U \in \mathbb{R}^n$ of $\boldsymbol{x}_0$, a vicinity $V \in \mathbb{R}^p$ of $\boldsymbol{\alpha}_0$, and a (continuously differentiable) function $\boldsymbol{x} : V \to U$ such that

$$\boldsymbol{F}(\boldsymbol{x}(\boldsymbol{\alpha}), \boldsymbol{\alpha}) = 0\,. \tag{10.3}$$

We call $\boldsymbol{x}(\boldsymbol{\alpha})$ a solution branch or family. That means that if we vary $\boldsymbol{\alpha}_0$ slightly to $\boldsymbol{\alpha} = \boldsymbol{\alpha}_0 + \delta\boldsymbol{\alpha}$, there will exist another fixed point $\boldsymbol{x} = \boldsymbol{x}_0 + \delta\boldsymbol{x}$. The basic principle of continuation is to compute the solution branch $\boldsymbol{x}(\boldsymbol{\alpha})$ by incremently varying $\boldsymbol{\alpha}$ and finding the new fixed point, e. g., by a Newton method. This procedure is illustrated in Fig. 10.1 (a). But with this simple method it is, e. g., not possible to follow a solution branch around a fold at a saddle node bifurcation. At such a fold the solution branch can no longer be parameterized by the parameters $\boldsymbol{\alpha}$. An enhancement of the method is *pseudo-arclength continuation*, which is illustrated in Fig. 10.1 (b). Here, the "test step" is not done in the $\boldsymbol{\alpha}$ direction for constant $\boldsymbol{x}$ as in the basic continuation, but tangential to the solution branch in the $(\boldsymbol{x}, \boldsymbol{\alpha})$ space. The next point of the branch is then searched in a direction perpendicular to the test step. In this way it is possible to follow a solution branch around a fold because the branch is then parameterized by its arclength. This type of continuation is implemented in the software package AUTO-07p.

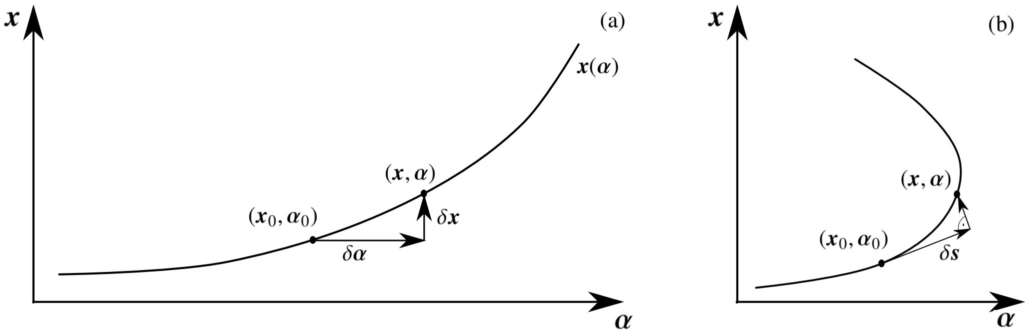

Fig. 10.1 (a) Illustration of a basic continuation procedure. The test step is done in $\boldsymbol{\alpha}$ direction keeping $\boldsymbol{x}$ constant, and the corrector step in $\boldsymbol{x}$ direction keeping $\boldsymbol{\alpha}$ constant. (b) Pseudo-arclength continuation. Here, the test step is performed tangentially to the branch. The corrector step is done in a direction orthogonal to the predictor step. This way it is possible to follow a branch around a saddle node bifurcation point. Often also in basic continuation the predictor step is tangentially to the branch, but as long as the corrector step is performed keeping $\boldsymbol{\alpha}$ constant it is not possible to follow a branch around a saddle node bifurcation point.

10.1.2 Important features of AUTO-07p

Branch point detection

With AUTO-07p it is possible to detect branch points of solution branches that occur, e. g., at a pitchfork bifurcation. At the detected branch points one can tell the software to switch branches and to follow the intersecting solution branch.

Boundary value problems

The software can also handle boundary value problems. That means that in addition to Eq. (10.1), one can set up boundary conditions for $\boldsymbol{x}(0)$ and $\boldsymbol{x}(1)$ and compute solutions $\boldsymbol{x}(t)$ on the interval $t \in [0, 1]$ (by rescaling the independent variable t, one can of course compute solutions on an arbitrary interval). In this case AUTO-07p will automatically discretize the problem with an adaptive grid in t. Starting from an analytic solution for a specific set of parameters $\boldsymbol{\alpha}_0$, which has to be provided by the user, the software can again compute solution branches, where each point of the branch does no longer correspond to a fixed point but to a specific solution $\boldsymbol{x}(t)$, $t \in [0, 1]$, i. e. a fixed point in function space. It is also possible to require that the determined solutions satisfy integral conditions as further constraints.

Fold continuation

When AUTO-07p detects a fold w. r. t. one parameter, it can follow this saddle-node bifurcation point as other parameters are varied. This is very useful to determine phase diagrams as we will see in Chap. 11.

10.2 Time simulations

In this section we describe the DNS of Eq. (9.24). As we will see in the following, the equation is *stiff* and therefore requires the use of an implicit time stepping algorithm. In the next subsection we explain the property of stiffness and why this property requires implicit time stepping schemes. In Sect. 10.2.2, we illustrate why the thin film equation is stiff. In Sect. 10.2.3 we present the backward differentiation formulae, which are a class of implicit time stepping methods that are employed in our time simulations.

10.2.1 Stiff ODEs

A linear ordinary differential equation (ODE)

$$\dot{\boldsymbol{x}} = \mathbf{A}\boldsymbol{x} \tag{10.4}$$

is called *stiff*, if all eigenvalues λ_i of the matrix $\mathbf{A}$ have negative real parts and [Joh]

$$\frac{\max_i |\mathrm{Re}\,\lambda_i|}{\min_i |\mathrm{Re}\,\lambda_i|} \gg 1\,. \tag{10.5}$$

A nonlinear ODE $\dot{\boldsymbol{x}} = \boldsymbol{f}(\boldsymbol{x})$ can be regarded as *locally stiff* if the Jacobian of $\boldsymbol{f}$ has the same properties as $\mathbf{A}$. The solution of (10.4) can be expressed as

$$x_j(t) = \sum_i \alpha_{ij} \mathrm{e}^{\lambda_i t} . \tag{10.6}$$

For large t, only the terms with small absolute values of $\mathrm{Re}\,\lambda_i$ will contribute significantly to the solution. However, an explicit time stepping method is only stable if the time step

$$\delta t \lesssim \frac{1}{\max_i |\mathrm{Re}\,\lambda_i|} . \tag{10.7}$$

The exact relation depends on the specific time stepping method. This means that although the fast time scales play no role for the long time solution, they require a very small time step in explicit time stepping schemes. Since the interesting dynamics typically takes place on the slow time scales, one needs to calculate a very large number of iterations to see the relevant dynamics.

In order to provide an intuitive understanding for the stability criterion (10.7), let us consider the simplest example

$$\dot{x} = -cx \tag{10.8}$$

with $c > 0$ and $x(0) = 1$, the solution of which is given by $x(t) = \mathrm{e}^{-ct}$. The simplest explicit time stepping scheme is the explicit Euler scheme,

$$\begin{aligned} x_{n+1} &= x_n - \delta t\, c\, x_n \\ &= (1 - \delta t\, c) x_n . \end{aligned} \tag{10.9}$$

This stability criterion of this method is

$$\delta t < \frac{2}{c} . \tag{10.10}$$

For $\delta t > 2/c$, $|x_n| \to \infty$ for $n \to \infty$.

If one employs an implicit time stepping scheme, one has no such strong stability constraints as we demonstrate now with the same example and the implicit Euler scheme

$$\begin{aligned} x_{n+1} &= x_n - \delta t\, c\, x_{n+1} \\ \Leftrightarrow x_{n+1} &= \frac{x_n}{1 + \delta t\, c} . \end{aligned} \tag{10.11}$$

We see that x_n will go to zero for $n \to \infty$, no matter how large we choose δt. But of course, the larger δt, the less accurate is the computed solution. However, since the fast time scales of a stiff problem are not relevant for the accuracy of the solution in the long time limit, δt only has to be small compared to the slow time scales for accuracy reasons. Therefore implicit time stepping schemes are the solution of the stiffness dilemma.

10.2.2 Why is the thin film equation stiff?

The stiffness of the thin film equation stems from the fourth order derivatives. This can be illustrated approximating the height profile as a truncated Fourier series,

$$h(x,t) = \sum_{k=-N}^{N} \tilde{h}_k(t)\mathrm{e}^{\mathrm{i}kx}, \tag{10.12}$$

leading to a set of ODEs for the Fourier coefficients $\tilde{h}_k(t)$. The fourth derivative w. r. t. x corresponds to a multiplication with k^4 in Fourier space:

$$\partial_t\, h(x,t) = -\partial_x^4\, h(x,t) \quad \longleftrightarrow \quad \partial_t\, \tilde{h}_k(t) = -k^4\, \tilde{h}_k(t) \tag{10.13}$$

Therefore, the modes with large k are damped away much more quickly than the modes with small k. Although the former modes play no role in the long term solution of the thin film equation, they enforce an extremely small time step if an explicit time stepping algorithm is employed.

10.2.3 Backward differentiation formulae

Backward differentiation formulae (BDF) are a class of implicit time stepping methods that are based on backward FDs. Since FD formulas exist in different orders of accuracy, so do BDF methods. The afore-mentioned implicit Euler scheme is the simplest BDF method of order one. It is based on the first order backward FD

$$g'(y_i) = \frac{g(y_i) - g(y_{i-1})}{\delta y} \tag{10.14}$$

with $\delta y = y_i - y_{i-1}$. Applied to the time derivative of a set of ODEs $\dot{\boldsymbol{x}} = \boldsymbol{f}(\boldsymbol{x})$, this yields

$$\boldsymbol{x}_n = \boldsymbol{x}_{n-1} + \delta t \boldsymbol{f}(\boldsymbol{x}_n) \tag{10.15}$$

with $\boldsymbol{x}_n = \boldsymbol{x}(t_n)$ and $\delta t = t_n - t_{n-1}$. Analogously, the second order BDF method is derived from

$$g'(y_i) = \frac{\frac{3}{2}g(y_i) - 2g(y_{i-1}) + \frac{1}{2}g(y_{i-2})}{\delta y} \tag{10.16}$$

which yields

$$\boldsymbol{x}_n = \tfrac{4}{3}\boldsymbol{x}_{n-1} - \tfrac{1}{3}\boldsymbol{x}_{n-2} + \tfrac{3}{2}\delta t \boldsymbol{f}(\boldsymbol{x}_n)\,. \tag{10.17}$$

We see, that the general BDF method of order k takes the form

$$\boldsymbol{x}_n = \sum_{i=1}^{k} \alpha_i \boldsymbol{x}_{n-i} + \beta_0\, \delta t\, \boldsymbol{f}(\boldsymbol{x}_n)\,. \tag{10.18}$$

The problem of this equation, which arises in *every* implicit method, is that the function $\boldsymbol{f}$ has to be evaluated at the point $\boldsymbol{x}_n$, which is not known in advance. Therefore one has to solve a set of nonlinear algebraic equations for $\boldsymbol{x}_n$. This is usually done by a Newton method, which we will briefly illustrate in the following section.

10.2.4 Solving the nonlinear algebraic equations

Finding a solution of a set of algebraic equations is analogous to finding a zero of a vector field, i. e., we search for a vector $\boldsymbol{y}$ that satisfies

$$\boldsymbol{F}(\boldsymbol{y}) = \mathbf{0}\,. \tag{10.19}$$

The Newton method can be derived from the Taylor series of the vector field,

$$\boldsymbol{F}(\boldsymbol{x} + \delta\boldsymbol{x}) = \boldsymbol{F}(\boldsymbol{x}) + \mathbf{J}\delta\boldsymbol{x} + O(||\delta\boldsymbol{x}||^2)\,, \tag{10.20}$$

where $\mathbf{J}$ is the Jacobian of $\boldsymbol{F}$. Starting at some point $\boldsymbol{x}$, we seek to find an appropriate $\delta\boldsymbol{x}$, such that $\boldsymbol{F}(\boldsymbol{x} + \delta\boldsymbol{x}) \approx 0$. This leads to

$$\mathbf{J}\delta\boldsymbol{x} = -\boldsymbol{F}(\boldsymbol{x})\,. \tag{10.21}$$

The last equation is a linear algebraic equation that has to be solved for $\delta\boldsymbol{x}$. Instead of computing the inverse of the Jacobian, it is more efficient to solve this equation by an LU-decomposition. That means, one decomposes the Jacobian into a product of a lower triangular matrix $\mathbf{L}$ and an upper triangular matrix $\mathbf{U}$. Then, one has

$$\begin{aligned} &\mathbf{J}\delta\boldsymbol{x} = -\boldsymbol{F}(\boldsymbol{x}) && (10.22)\\ \Leftrightarrow\ &\mathbf{LU}\delta\boldsymbol{x} = -\boldsymbol{F}(\boldsymbol{x}) && (10.23)\\ \Leftrightarrow\ &\mathbf{L}\boldsymbol{y} = -\boldsymbol{F}(\boldsymbol{x}) \quad \text{and} \quad \mathbf{U}\delta\boldsymbol{x} = \boldsymbol{y} && (10.24) \end{aligned}$$

The last two equations can be solved simply by forward and backward substitution, respectively. After $\delta\boldsymbol{x}$ has been computed, the process is iterated starting from a new point $\boldsymbol{x}_{\text{new}} = \boldsymbol{x} + \delta\boldsymbol{x}$, until some predefined convergence criterion is satisfied.

Eq. (10.21) applied to the BDF scheme (10.18) yields

$$(\mathbf{1} - \beta_0\,\delta t\,\mathbf{f}'(\tilde{\boldsymbol{x}}_n))\,\delta\boldsymbol{x} = -\tilde{\boldsymbol{x}}_n + \beta_0\,\delta t\,\boldsymbol{f}(\tilde{\boldsymbol{x}}_n) + \sum_{i=1}^{k} \alpha_i \boldsymbol{x}_{n-i}\,. \tag{10.25}$$

Here $\mathbf{1}$ is the unit matrix, $\mathbf{f}'$ is the Jacobian of $\boldsymbol{f}$, and $\tilde{\boldsymbol{x}}_n$ is the trial point that is iterated. The LU-decomposition has to be applied to the matrix $\mathbf{1} - \beta_0\,\delta t\,\mathbf{f}'(\tilde{\boldsymbol{x}}_n)$.

For two-dimensional thin film equations on a grid with N^2 grid points, the latter matrix is an $N^2 \times N^2$ matrix with N^4 components. This can cause serious memory (and computation time) problems. For example, for $N = 400$ the matrix consists of $25.6 \cdot 10^9$ numbers. If the numbers are stored as 8-byte floating-point numbers, this requires roughly 200 GB of memory, only to save the Jacobian!

However, if one uses a spatial discretization employing FDs, most of the entries of the Jacobian are zero, i. e., the Jacobian is a sparse matrix. This results from the coupling between the grid points via the spatial derivatives. For pseudo-spectral methods, on the contrary, a spatial derivative depends on all grid points, which is why the Jacobian is dense in this case. There are efficient algorithms for the LU-decomposition, where the zero entries do not have to be stored and where also the computation time is highly reduced by taking advantage of the sparsity of the matrix.

Another common method used for the linear algebra are *Krylov subspace methods* [LS03]. The problem of the latter is that they are only efficient if a suitable preconditioner matrix can be supplied, which is difficult in the case of the two-dimensional thin film equation. A more detailed discussion about this issue can be found in Ref. [BT10].

10.2.5 Why we employ library routines

The introduced BDF scheme (10.18) is only valid for a constant size of the time step δt. Schemes with a variable step size, which can be adapted to maintain a predefined accuracy, are much more complicated in multistep methods such as BDF because then the coefficients α_i and β_0 depend on the previous step sizes. However, adaptive time stepping is extremely important for an efficient DNS.

The reader is now probably convinced that it would be very intricate to implement all the different steps that are necessary for an efficient time simulation by hand. That is why we use a library routine from the NAG Fortran library [NAG] for the time stepping. It employs BDF methods of variable order and variable step sizes, and does also take advantage of the sparsity of the Jacobian. The user of this library routine has to supply the spatial discretization, the RHS of the equation, the initial condition and the output routines for the results.

It turns out that the included linear algebra routines run into problems if two many grid points are used. To be able to perform time simulations with the required accuracy anyway, we employ finite differences with higher orders as described in the next section.

10.2.6 Spatial discretization

As we discussed in Sect. 10.2.4 implicit methods are only beneficial if the Jacobian of the RHS of the PDE is sparse. Therefore, spectral or pseudo-spectral methods are not suited for our problem. We employ FDs instead.

FD formulas, which approximate the spatial derivatives, exist in different orders of accuracy. The higher the order, the more grid points are involved. For example, the central difference formula for the first derivative with second order accuracy reads

$$f'(x_i) = \frac{1}{2\delta x}(f(x_{i+1}) - f(x_{i-1})) + O\left(\delta x^2\right) , \tag{10.26}$$

and involves the two neighboring grid points. With fourth order accuracy, the same derivative reads

$$f'(x_i) = \frac{1}{\delta x}\left(\tfrac{1}{12}f(x_{i-2}) - \tfrac{2}{3}f(x_{i-1}) + \tfrac{2}{3}f(x_{i+1}) - \tfrac{1}{12}f(x_{i+2})\right) + O\left(\delta x^4\right) , \tag{10.27}$$

involving the four neighboring grid points.

FD formulas can either be derived from the Taylor series or be approximating the function through a polynomial of the same order as the derivative that is needed. For high orders of accuracy, these derivations become quite cumbersome and are also hard to find in the literature. However, there is a useful command for the symbolic mathematics software Mathematica [Mat] that calculates central FD formulas on a homogeneous grid for arbitrary order of the derivative and accuracy from polynomial interpolations. It reads:

```
  Simplify[ D[ InterpolatingPolynomial[ Table[ {Subscript[x,
i] + k h, f[Subscript[x, i + k]]}, {k, -n_g, n_g, 1}] , z ],
{z, n_o} ] /.  z -> Subscript[x, i]]
```

Here, n_g has to be replaced by a positive integer number such that the formula incorporates $2n_g + 1$ grid points, and n_o has to be replaced by the order of the desired derivative. For example, $n_g = 2$ and $n_o = 4$ yields a formula for the fourth derivative including five grid points, which is of second order accuracy.

A higher accuracy of the FDs brings along more non-zero elements of the Jacobian, which requires more memory and computation time to perform the LU-decomposition. On the other hand, a large accuracy allows us to decrease the number of grid points, which lowers the memory and computation time costs. And, furthermore, a reduced spatial resolution allows for larger time increments. However, since the numerical problems of the NAG library restrict us to a relatively small number of grid points anyway (cf. Sec. 10.2.5), we are forced to use finite differences of very high order. In the simulations presented in Chap. 12 we employ formulas including 9 and 15 grid points for the simulations with smaller and larger mean film heights, respectively. The coefficients of the formulas are listed in Tabs. 10.1 and 10.2, respectively. To clarify the notation, we give as an example the first derivative of the 15-point stencil:

$$\begin{aligned} f'(x_i) = \frac{1}{\delta x}\Big[&- \tfrac{1}{24024}f(x_{i-7}) + \tfrac{7}{10296}f(x_{i-6}) - \tfrac{7}{1320}f(x_{i-5}) + \tfrac{7}{264}f(x_{i-4}) \\ &- \tfrac{7}{72}f(x_{i-3}) + \tfrac{7}{24}f(x_{i-2}) - \tfrac{7}{8}f(x_{i-1}) + \tfrac{7}{8}f(x_{i+1}) - \tfrac{7}{24}f(x_{i+2}) \\ &+ \tfrac{7}{72}f(x_{i+3}) - \tfrac{7}{264}f(x_{i+4}) + \tfrac{7}{1320}f(x_{i+5}) - \tfrac{7}{10296}f(x_{i+6}) \\ &+ \tfrac{1}{24024}f(x_{i+7})\Big] + O\left(\delta x^{14}\right) . \end{aligned} \tag{10.28}$$

Tab. 10.1 Coefficients of finite difference formulas including nine grid points.

	-4	-3	-2	-1	0	1	2	3	4	order
f'	1/280	-4/105	1/5	-4/5	0	4/5	-1/5	4/105	-1/280	δx^8
f''	-1/560	8/315	-1/5	8/5	-205/72	8/5	-1/5	8/315	-1/560	δx^8
f'''	-7/240	3/10	-169/120	61/30	0	-61/30	169/120	-3/10	7/240	δx^6
f''''	7/240	-2/5	169/60	-122/15	91/8	-122/15	169/60	-2/5	7/240	δx^6

Tab. 10.2 Coefficients of finite difference formulas including 15 grid points. Only the half stencil is shown, because the formulas for the first and third derivative are odd, and the formulas for the second and fourth derivative are even. To clarify the notation, Eq. (10.28) gives the formula of the first derivative as an example.

	0	1	2	3	4	5	6	7	order
f'	0	$\frac{7}{8}$	$-\frac{7}{24}$	$\frac{7}{72}$	$-\frac{7}{264}$	$\frac{7}{1320}$	$-\frac{7}{10296}$	$\frac{1}{24024}$	δx^{14}
f''	$-\frac{266681}{88200}$	$\frac{7}{4}$	$-\frac{7}{24}$	$\frac{7}{108}$	$-\frac{7}{528}$	$\frac{7}{3300}$	$-\frac{7}{30888}$	$\frac{1}{84084}$	δx^{14}
f'''	0	$-\frac{90281}{33600}$	$\frac{222581}{100800}$	$-\frac{247081}{302400}$	$\frac{31957}{138600}$	$-\frac{2077}{44352}$	$\frac{20137}{3326400}$	$-\frac{59}{158400}$	δx^{12}
f''''	$\frac{54613}{3780}$	$-\frac{90281}{8400}$	$\frac{222581}{50400}$	$-\frac{247081}{226800}$	$\frac{31957}{138600}$	$-\frac{2077}{55440}$	$\frac{20137}{4989600}$	$-\frac{59}{277200}$	δx^{12}

11 Transversal linear stability analysis

The scope of this chapter is to analyze the stability of solutions with a ridge centered on a more wettable stripe as various system parameters are varied. The relevant system parameters include the mean film height $\bar{h}$, which corresponds to the amount of material that is deposited in the experiments, the strength of the wettability contrast ρ, and the parameters for the geometry of the stripe pattern.

First, we outline the general procedure of the transversal linear stability analysis and describe how it is implemented in the continuation software package AUTO-07p. Subsequently, in Sect. 11.2 we illustrate the analysis with the most simple case of a sinusoidal wettability modulation. In Sect. 11.3 we consider a more complex and more realistic stripe geometry.

11.1 Description of the procedure and implementation in AUTO-07p

First, we determine steady solutions with a ridge centered on a more wettable stripe. To this end, it is sufficient to consider only the spatial dimension of the substrate plane perpendicular to the chemical stripes (the x direction) and to look for stationary drop solutions of the corresponding one-dimensional thin film equation that are centered on the more wettable site. Such a solution can be extended homogeneously in the dimension parallel to the stripe pattern (the y direction) corresponding to a stationary solution of the two-dimensional thin film equation, where all y derivatives vanish. Then one can perform a linear stability analysis about such a ridge solution.

To obtain one-dimensional stationary drop solutions $h_0(x)$, we regard Eq. (9.24) and set $\partial_t h_0 = 0$. Integrating twice in x leads to

$$\partial_x^2 h_0(x) + \Pi(h_0, x) + C = 0 \,. \tag{11.1}$$

The first integration constant corresponds to a net flux out of or into the integration domain, which is zero in our case. The second integration constant C is the pressure, which in mechanical equilibrium is constant along the drop profile.

Note that Eq. (11.1) can also be derived by a variation of the dimensionless free energy functional

$$F[h_0] = \int_0^L \mathrm{d}x \left[\frac{1}{2}(\partial_x h_0)^2 + f(h_0, x)\right] \tag{11.2}$$

under the constraint

$$\int_0^L \mathrm{d}x\, h_0 = L\bar{h}\,, \tag{11.3}$$

where L is the physical domain size. Then we see that the parameter C can also be interpreted as a Lagrange multiplier that fixes the volume.

For the implementation in AUTO-07p we first have to transform Eq. (11.1), a second-order ODE, into two first-order ODEs. Second, we introduce a rescaled space coordinate $\xi = x/L$, such that $\xi \in [0, 1]$. We define the new variables

$$u_1(\xi) = h_0(L\xi) - \bar{h} \tag{11.4}$$

$$u_2(\xi) = \left.\frac{\mathrm{d}h_0}{\mathrm{d}x}\right|_{x=L\xi}\,. \tag{11.5}$$

Since AUTO-07p only allows for autonomous ODEs, we need a third dependent variable for space,

$$u_7(\xi) = L\xi\,, \tag{11.6}$$

and obtain the three ODEs

$$\dot{u}_1 = L u_2 \tag{11.7}$$

$$\dot{u}_2 = -L[\Pi(\bar{h} + u_1, u_7) + C] \tag{11.8}$$

$$\dot{u}_7 = L\,, \tag{11.9}$$

where the dot denotes a derivative w. r. t. ξ. Later we will introduce the variables u_3 to u_6 in the context of the transversal linear stability analysis.

To compute a solution branch with continuation, one first needs a starting solution for a specific set of parameters. In our case we choose the trivial solution $u_1(\xi) = u_2(\xi) = 0\ \forall\, \xi \in [0, 1]$ (and of course $u_7(\xi) = L\xi$ by definition) at $\rho = 0$ and $C = -\Pi(\bar{h})$, which corresponds to a flat film on a homogeneous substrate. From this trivial solution one obtains by continuation a solution branch of non-trivial solutions as one changes ρ.

Starting from such a non-trivial, one-dimensional drop solution $h_0(x)$, we can perform the transversal linear stability analysis of the corresponding two-dimensional ridge solution. To this end, we make the ansatz

$$h(x, y, t) = h_0(x) + \varepsilon h_1(x) \exp(\beta t + \mathrm{i}qy)\,, \tag{11.10}$$

where ε is a smallness parameter and β is the growth rate of a harmonic perturbation in y direction with a wavenumber q. Inserting this ansatz into (9.24) and linearizing in ε yields

$$\begin{aligned}\beta h_1 =& -Q(h_0)\,(\partial_x^2 - q^2)\left[(\partial_x^2 - q^2)h_1 + (\partial_h \Pi(h_0, x))h_1\right]\\ & - (\partial_x Q(h_0))\partial_x\left[(\partial_x^2 - q^2)h_1 + (\partial_h \Pi(h_0, x))h_1\right]. \qquad (11.11)\end{aligned}$$

This eigenvalue equation has to be solved simultaneously with (11.1). To implement this equation in AUTO-07p we introduce further variables:

$$u_3(\xi) = h_1(L\xi) \qquad (11.12)$$

$$u_4(\xi) = \left.\frac{\mathrm{d}h_1}{\mathrm{d}x}\right|_{x=L\xi} \qquad (11.13)$$

$$u_5(\xi) = \left.\frac{\mathrm{d}^2h_1}{\mathrm{d}x^2}\right|_{x=L\xi} \qquad (11.14)$$

$$u_6(\xi) = \left.\frac{\mathrm{d}^3h_1}{\mathrm{d}x^3}\right|_{x=L\xi}. \qquad (11.15)$$

This leads to the additional ODEs

$$\dot{u}_3 = Lu_4 \qquad (11.16)$$

$$\dot{u}_4 = Lu_5 \qquad (11.17)$$

$$\dot{u}_5 = Lu_6 \qquad (11.18)$$

$$\begin{aligned}\dot{u}_6 =& L\Big\{-\frac{\beta u_3}{Q_0} + q^2u_5 - \partial_x^2(h_1\partial_h\Pi_0) - \frac{\partial_x Q_0}{Q_0}\left[(u_6 - q^2u_4 + \partial_x(h_1\partial_h\Pi_0)\right]\\ & + q^2\left[u_5 - q^2u_3 + \Pi'(\bar{h} + u_1, u_7)u_3\right]\Big\} \qquad (11.19)\end{aligned}$$

with $Q_0 = Q(u_1 + \bar{h})$ and

$$\partial_x(h_1\partial_h\Pi_0) = \Pi''(\bar{h} + u_1, u_7)u_2u_3 + \Pi'(\bar{h} + u_1, u_7)u_4 + \Pi'_x(\bar{h} + u_1, u_7)u_3 \qquad (11.20)$$

$$\begin{aligned}\partial_x^2(h_1\partial_h\Pi_0) =& \Pi'''(\bar{h} + u_1, u_7)u_2^2u_3 + \Pi''(\bar{h} + u_1, u_7)(\partial_x^2h_0)u_3\\ & + 2\Pi''(\bar{h} + u_1, u_7)u_2u_4 + \Pi'(\bar{h} + u_1, u_7)u_5\\ & + 2\Pi'_x(\bar{h} + u_1, u_7)u_4 + 2\Pi''_x(\bar{h} + u_1, u_7)u_2u_3\\ & + \Pi'_{xx}(\bar{h} + u_1, u_7)u_3\,. \qquad (11.21)\end{aligned}$$

Here, primes denote derivatives w. r. t. h, and the index x indicates a derivative w. r. t. x while keeping h constant.

Now we have derived the complete dynamical system that has to be implemented in AUTO-07p together with the boundary conditions

$$u_i(0) = u_i(1) \quad \text{for } i = 1, \ldots, 6 \qquad (11.22)$$

$$u_7(0) = 0\,, \qquad (11.23)$$

and the integral condition for mass conservation, Eq. (11.3), which reads in the new variables

$$\int_0^1 u_1 \mathrm{d}\xi = 0\,. \tag{11.24}$$

It should be noted that all eigenvalues β are real in our case because the thin film equation can be interpreted as a gradient dynamics (cf. Sect. 9.1). A complex eigenvalue would complicate the numerical treatment dramatically.

In the next section we will demonstrate the various continuation runs that are necessary for our analysis, employing a simple sinusoidal wettability modulation.

11.2 Sinusoidal wettability modulation

We start with a simple harmonic form of the wettability modulation

$$g(x) = \sin(2\pi x/L_{\mathrm{per}})\,, \tag{11.25}$$

where L_{per} is the periodicity of the stripe pattern. We choose the domain size L equal to L_{per}, i. e., we only investigate a single stripe. Starting from the trivial solution described in the previous section, we use ρ as the main continuation parameter in the first run. This yields the solution branches shown in Fig. 11.1. Each point of a branch corresponds to one stationary height profile. Figure 11.2 shows three examples of solutions for $\rho = 0.5$ according to the labels in Fig. 11.1. Solutions 1 and 2 are unstable and correspond to profiles with maxima located on the less wettable stripe (LWS). Solution 3 is stable and corresponds to a drop centered on the more wettable stripe (MWS).

For the next continuation run, we start at the stable drop solution. We fix ρ and select the growth rate β as the main continuation parameter (which was fixed at $\beta = 0$ before). For a fixed value of the wavelength $q \neq 0$, we expect a discrete spectrum of eigenvalues β. At each discrete eigenvalue, a new solution branch which consists of solutions with $h_1(x) \neq 0$ is detected to branch off the trivial $h_1(x) = 0$ branch. At a detected branch point, one can tell AUTO-07p to follow the bifurcating branch. Adding as a new integral condition the definition of the L_2 norm of $h_1(x)$, we select $||h_1||$ as a new continuation parameter, and follow the new branch until $||h_1|| = 1$, and hence "blow up" the eigenfunction $h_1(x)$. With this procedure we obtain the two eigenfunctions depicted in Fig. 11.3. One is a symmetric varicose mode, the other one an antisymmetric zigzag mode.

In order to make a statement about the stability of the ridge solutions, we have to compute the dispersion relations $\beta(q)$ for the detected eigenfunctions. This is done by a subsequent continuation run fixing $||h_1|| = 1$ and choosing β and q as continuation

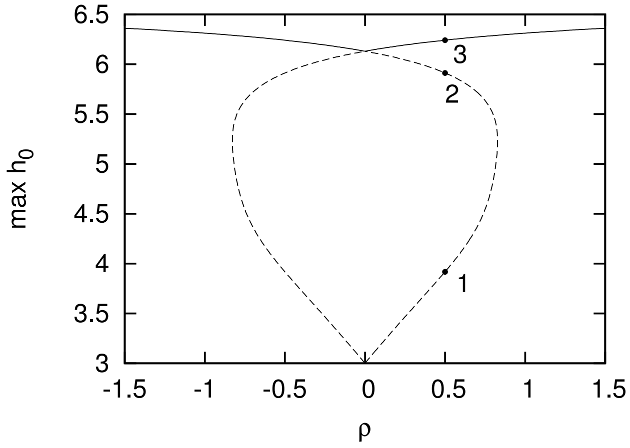

Fig. 11.1 Solution branches obtained by a first continuation in the wettability contrast ρ. As a measure of the obtained solutions we select the maximum values of the height profiles $\max_x h_0(x)$. The solid and dashed parts of the branches represent stable and unstable solutions, respectively. The parameters are $\bar{h} = 3$ and $L_{\text{per}} = 50$. The solutions according to the three labels are depicted in Fig. 11.2. The solution at $\max h_0 = \bar{h}$ corresponds to the trivial flat film solution.

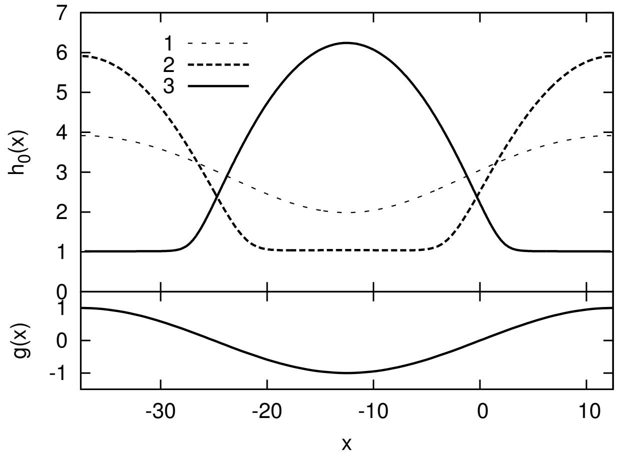

Fig. 11.2 Top: Three solutions according to the labels in Fig. 11.1. Bottom: The inhomogeneity function $g(x)$ (cf. Eq. (11.25)). The more (less) wettable area corresponds to $g(x) \approx -1$ ($g(x) \approx 1$). Solutions 1 and 2 are unstable. In those cases, more liquid is on the LWS. Solution 3 represents a stable drop on the MWS. The solutions are calculated with periodic boundary conditions. The plotted x domain is chosen such that the MWS is in the center of the plot.

parameters. Figure 11.4 shows the corresponding dispersion relations for the two eigenmodes of Fig. 11.3. One can see that for the varicose mode there exists a finite band of wavenumbers $0 < q < q_c$ with positive growth rate β. For $q = 0, \beta$ must be zero

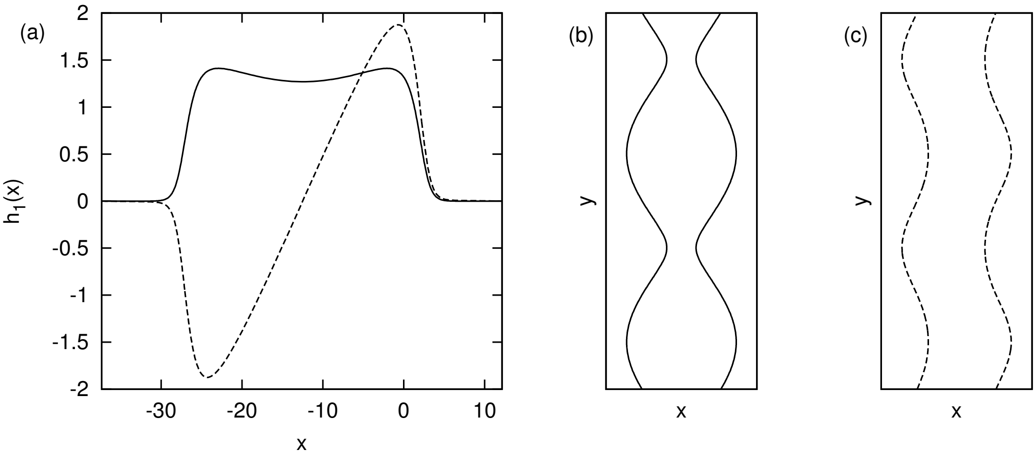

Fig. 11.3 (a) The two most important eigenmodes $h_1(x)$. The solid curve is a symmetric varicose mode, the dashed curve is an antisymmetric zigzag mode. Panels (b) and (c) show contour lines of $h_0(x) + \varepsilon h_1(x)\sin(qy)$ for the varicose and zigzag mode, respectively. The corresponding dispersion relations are plotted in Fig. 11.4. ($\rho = 0.5$, $\bar{h} = 3$).

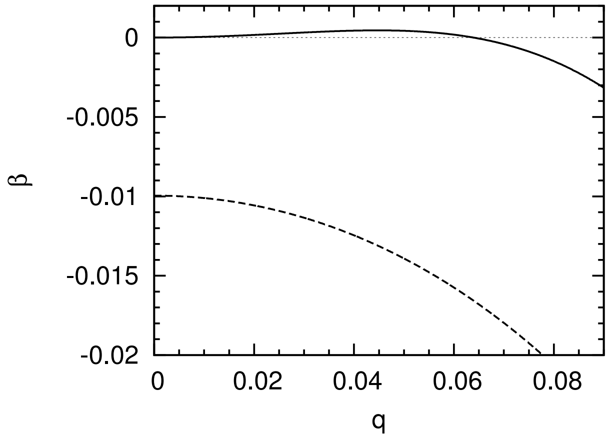

Fig. 11.4 Dispersion relations of the two eigenmodes shown in Fig. 11.3. Shown is the growth rate β as a function of the transversal wave number q. The solid curve and the dashed curve correspond to the varicose and zigzag mode, respectively.

due to mass conservation as long as the integral of the eigenmode is not zero. For the zigzag mode, $\beta(q) < 0$ for all q.

As a next step, we compute the stability threshold for the transversal instability of the ridge w. r. t. one system parameter, e. g., the mean film height $\bar{h}$. To this end, we employ the fold continuation feature of AUTO-07p. The maximum of the dispersion relation $\beta(q)$ corresponds to a fold in the corresponding function $q(\beta)$. Via the fold continuation feature, we can follow this fold as several system parameters are varied. As we expect the ridge to be stable for smaller film thicknesses $\bar{h}$, we follow this fold as we vary $\bar{h}$ until β and q become almost[1] zero. In this way we approximate the stability threshold w. r. t. $\bar{h}$. In a subsequent fold continuation run, we fix $\beta \approx 0$ and allow another system parameter to vary, e. g., the wettability contrast ρ. This yields a curve in the $[\bar{h}, \rho]$ plane that marks the linear stability threshold. This curve is plotted in Fig. 11.5. For each

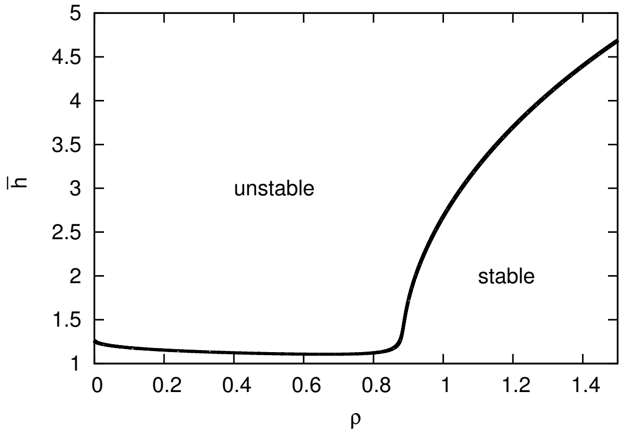

Fig. 11.5 Linear stability diagram for the transversal instability of a ridge in the $[\rho, \bar{h}]$ plane.

value of ρ there is a threshold $\bar{h}_c(\rho)$, such that a ridge is linearly stable for $\bar{h} < \bar{h}_c(\rho)$ and unstable for $\bar{h} > \bar{h}_c(\rho)$. If the ridge is unstable, perturbations in the form of the varicose mode will grow. Therefore, we call the varicose mode the *critical* eigenmode.

In the main part of the plot, the function $\bar{h}_c(\rho)$ is monotonously increasing, which is in agreement with our intuition and the experimental findings. For small ρ this is not the case. The reason for this will be discussed in Sect. 11.3.

11.3 Smoothed step-like wettability profile

Now we switch to a more realistic non-sinusoidal wettability modulation,

$$g(x) = \tanh\left[\frac{1}{l_s}\left(-\mathrm{frac}\left(\frac{x}{L_{\mathrm{per}}}\right) + x_A\right)\right] \cdot \tanh\left[\frac{1}{l_s}\left(-\mathrm{frac}\left(\frac{x}{L_{\mathrm{per}}}\right) + (1 - x_A)\right)\right], \quad (11.26)$$

where frac denotes the fractional function $\mathrm{frac}(y) = y - \mathrm{floor}(y)$. Here, the floor function returns the largest integer value that is smaller as or equal to its argument. The function $g(x)$ is plotted in Fig. 11.6. As the sinusoidal wettability modulation of the last section,

---

[1] For numerical reasons, we can not detect the zero with arbitrary accuracy.

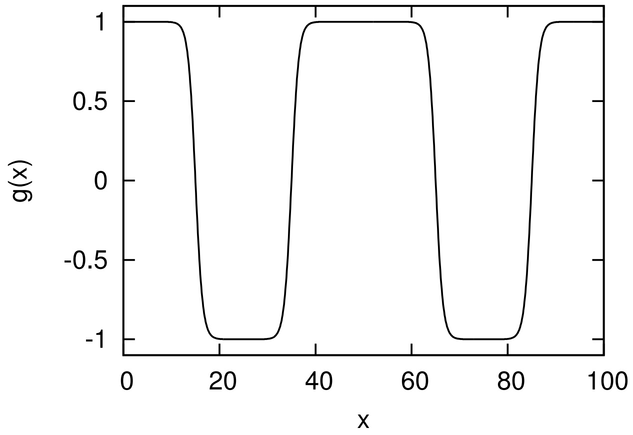

Fig. 11.6 The wettability modulation $g(x)$, Eq. (11.26), for the parameters $L_{\mathrm{per}} = 50$, $l_s = 0.03$ and $x_A = 0.3$, where L_{per} is the period length; for $\rho > 0$ the lengths of the MWS ($g(x) \approx -1$) and the LWS ($g(x) \approx 1$) are given by $(1 - 2x_A)L_{\mathrm{per}}$ and $2x_A L_{\mathrm{per}}$, respectively, and $l_s L_{\mathrm{per}}$ is the width of the transition region between the MWS and the LWS.

it is periodic with a period L_{per}, but now the MWS and the LWS can have different widths, which are determined by the parameter $0 < x_A < 0.5$. The widths of the LWS and the MWS are given by $2x_A L_{\mathrm{per}}$ and $(1 - 2x_A)L_{\mathrm{per}}$, respectively. The parameter l_s governs the sharpness of the wettability contrast: The width of the transition region between the MWS and LWS is given by $l_s L_{\mathrm{per}}$.

11.3.1 Stationary ridge profiles

As in the previous section, we set $L = L_{\mathrm{per}} = 50$ and start with the trivial solution for $\rho = 0$ and use ρ as the main continuation parameter in the first runs. We select $x_A = 0.3$, which means that (for positive ρ) the MWS is thinner than the LWS. We obtain the solution branches plotted in Fig. 11.7. In contrast to the case of the sinusoidal wettability modulation (cf. Fig. 11.1), we do no longer have a symmetry between positive and negative ρ values due to the difference in the width of the LWS and the MWS. For positive ρ, we obtain a larger variety of unstable configurations. The different stable and unstable solutions are plotted in Figures 11.8 and 11.9 for $\rho = 0.5$ and $\rho = -0.5$, respectively.

The bifurcation diagram, Fig. 11.7, might not be complete. For symmetry reasons one expects additional branches consisting of further unstable steady solutions. However, for the following analysis these solutions are not important.

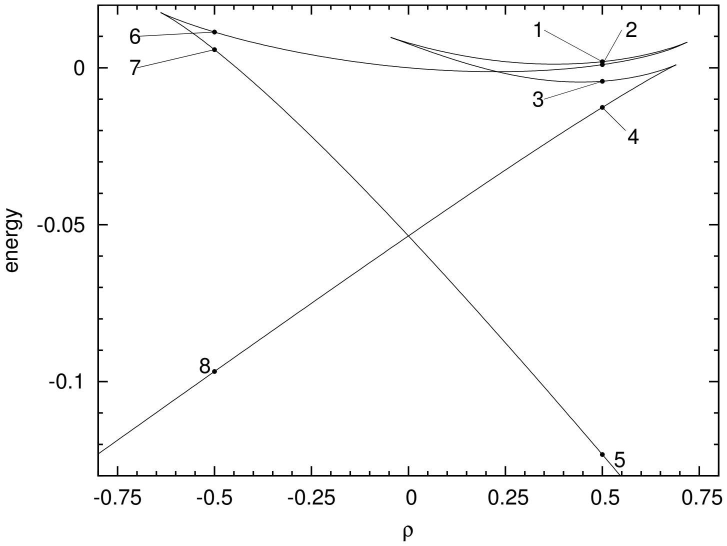

Fig. 11.7 Solution branches obtained by a first continuation in the wettability contrast ρ. In contrast to Fig. 11.1, we use the energy (Eq. (9.9)) as a solution measure in order to assess the stability of the solutions. Since $x_A = 0.3$, the MWS is thinner than the LWS for positive ρ and vice versa for negative ρ, which breaks the reflection symmetry in ρ. The solutions corresponding to the labels one to five and six to eight are shown in Figs. 11.8 and 11.9 for $\rho = 0.5$ and $\rho = -0.5$, respectively. The parameters are $L_{\text{per}} = 50$, $l_s = 0.03$, $\bar{h} = 3$ and $x_A = 0.3$.

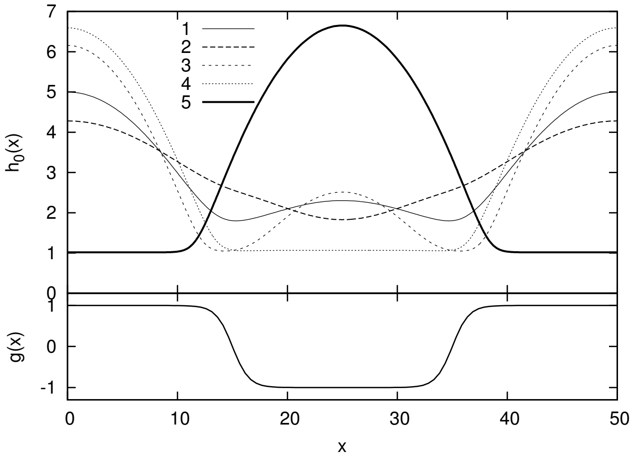

Fig. 11.8 Solutions corresponding to the labels one to five of Fig. 11.7 for $\rho = 0.5$. $L_{\text{per}} = 50$, $l_s = 0.03$, $\bar{h} = 3$ and $x_A = 0.3$. As ρ is positive, the more wettable area corresponds to the region where $g(x) \approx -1$. Solution five, the one with the lowest energy, is the only stable solution.

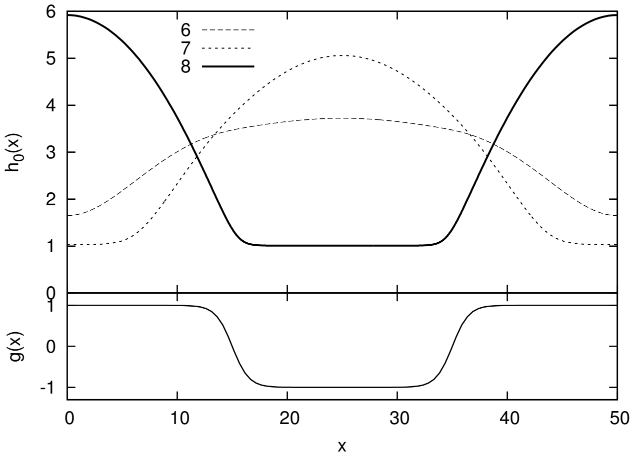

Fig. 11.9 Solutions corresponding to the labels six to eight of Fig. 11.7 for $\rho = -0.5$. $L_{\text{per}} = 50$, $l_s = 0.03$, $\bar{h} = 3$ and $x_A = 0.3$. Since ρ is negative, the more wettable area corresponds to the region where $g(x) \approx 1$. Here, solution eight is the only stable solution.

11.3.2 The linear stability diagram

Starting at the stable solution for $\rho = 0.5$ (label 5 in Figs. 11.7 and 11.8), we repeat the steps presented in the previous section and obtain again a linear stability diagram in the $[\rho, \bar{h}]$ plane (cf. Fig. 11.10). In contrast to the case of the sinusoidal wettability

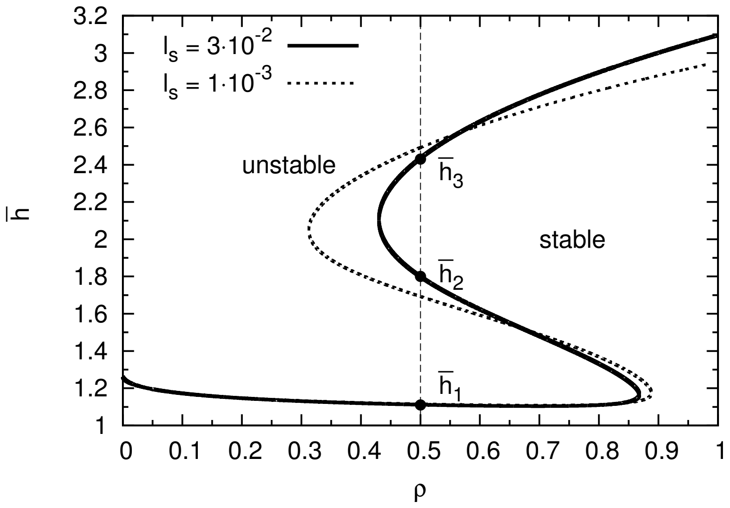

Fig. 11.10 Linear stability diagram for the transversal instability of a ridge in the $[\rho, \bar{h}]$ plane for $l_s = 0.03$ (solid line) and $l_s = 0.001$ (dotted line). For $\rho = 0.5$ there are three stability thresholds $\bar{h}_1, \bar{h}_2, \bar{h}_3$.

modulation (Fig. 11.5), the curve is non-monotonous. In the region $0.43 \lesssim \rho \lesssim 0.87$ there are four different stability regions that deserve further investigation.

11.3.3 Detailed analysis for $\rho = 0.5$

To this end, we consider a constant $\rho = 0.5$, where we observe three critical values of $\bar{h}$, $\bar{h}_1 \approx 1.1$, $\bar{h}_2 \approx 1.8$ and $\bar{h}_3 \approx 2.4$ (cf. Fig. 11.10). We continue the stable 1d solution $h_0(x)$ and its critical eigenfunction $h_1(x)$ in the mean film thickness $\bar{h}$. Figures 11.11 and 11.12 show the obtained functions $h_0(x)$ and $h_1(x)$, respectively. In Fig. 11.13 (a), we plot the corresponding maximal growth rates

$$\beta_{\max} = \max_q \beta(q) = \beta(q_{\max}) \tag{11.27}$$

and the corresponding $q_{\max}$ in the unstable regions $\bar{h}_1 < \bar{h} < \bar{h}_2$ and $\bar{h} > \bar{h}_3$. In the stable regions $\bar{h} < \bar{h}_1$ and $\bar{h}_2 < \bar{h} < \bar{h}_3$, $\beta_{\max} = q_{\max} = 0$.

For very thin films ($\bar{h} < \bar{h}_1$), the 1d solutions are not yet droplets. They are better described as piecewise flat films with a higher thickness on the MWS (cf. solution for $\bar{h} = 1.05$ in Fig. 11.11). The film height is everywhere below the critical film height where spinodal dewetting would occur on a homogeneous substrate (cf. Eq. (9.37) in Sect. 9.5). Therefore, the piecewise flat film solutions are stable, also in two dimensions.

For $\bar{h}_1 < \bar{h} < \bar{h}_2$, the 1d solutions have a pronounced droplet shape (cf. solution for $\bar{h} = 1.5$ in Fig. 11.11). The corresponding 2d ridge solutions are not stable, but this instability is not the one that leads to the formation of bulges. This can be inferred from the shape of the critical eigenfunction $h_1(x)$, which is depicted in Fig. 11.12 for different $\bar{h}$. It undergoes a shape transition from unimodal to bimodal with increasing film height. The top panel of Fig. 11.14 shows the steady ridge profile $h_0(x)$ for $\bar{h} = 1.5$ together

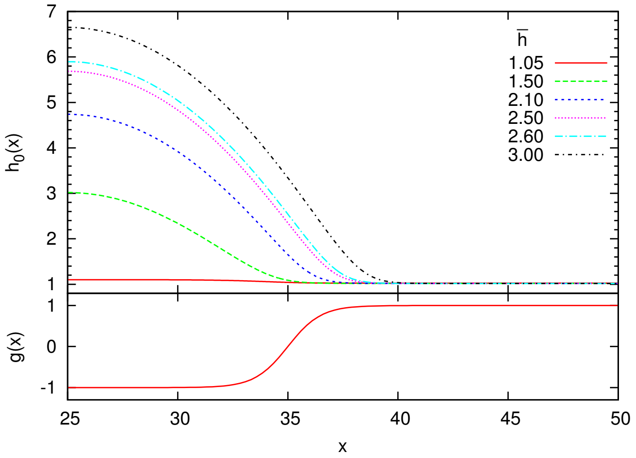

Fig. 11.11 Stationary solutions $h_0(x)$ for $\rho = 0.5$ and different mean film heights $\bar{h}$.

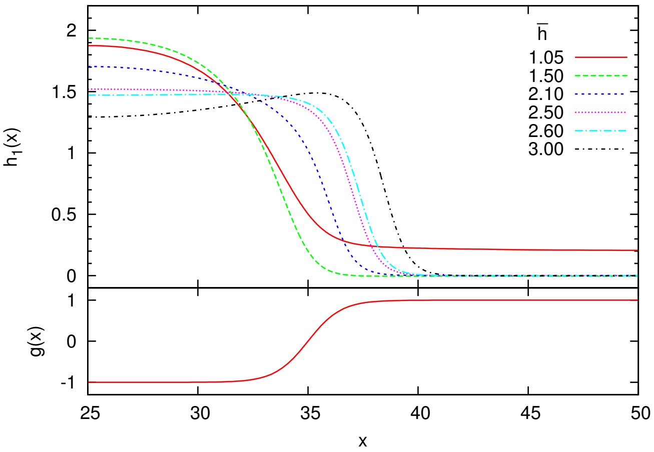

Fig. 11.12 Critical eigenfunction $h_1(x)$ for $\rho = 0.5$ and different mean film heights $\bar{h}$. At $2.5 < \bar{h} < 2.6$, the transition between a unimodal and a bimodal shape occurs.

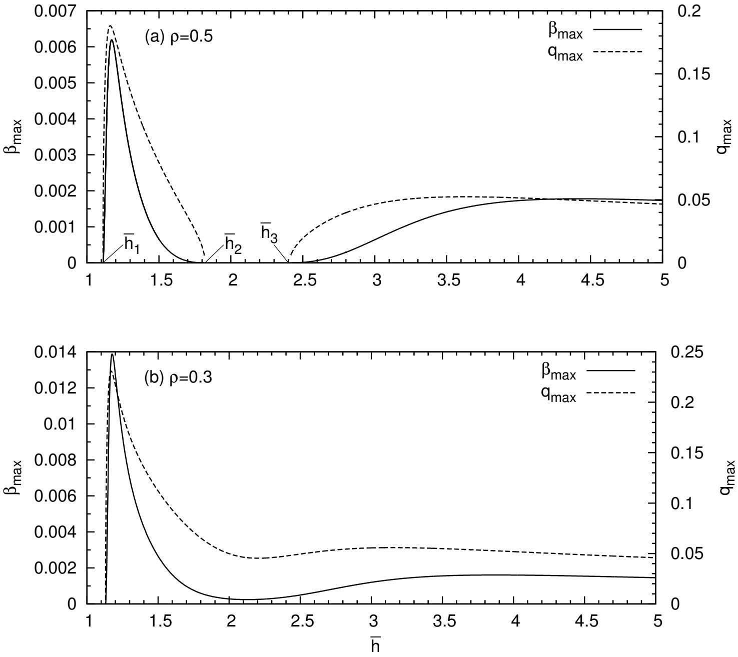

Fig. 11.13 Maximal growth rates $\beta_{\max}$ and the corresponding $q_{\max}$, which are defined in Eq. (11.27), against $\bar{h}$ for (a) $\rho = 0.5$ and (b) $\rho = 0.3$. In the regions $\bar{h} < \bar{h}_1$ and $\bar{h}_2 < \bar{h} < \bar{h}_3$, $\beta_{\max}$ and $q_{\max}$ are zero for $\rho = 0.5$; a ridge is stable in these cases.

with a sum of the ridge profile and a multiple of the corresponding eigenfunction $h_1(x)$. One can see that the contact region is not shifted by the influence of the unimodal

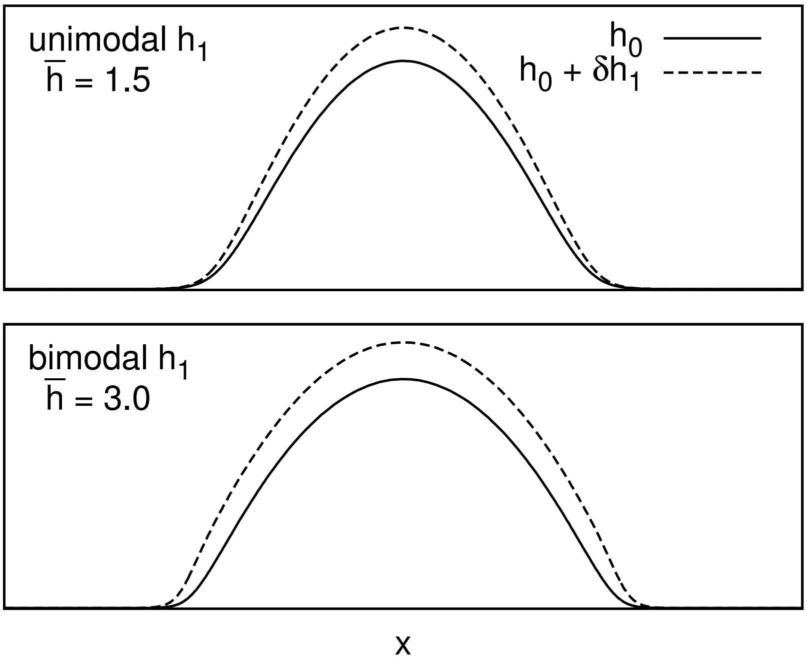

Fig. 11.14 Comparison of transversal instabilities with a unimodal eigenfunction $h_1(x)$ for small film heights (top, $\bar{h} = 1.5$) and a bimodal $h_1(x)$ for larger film heights (bottom, $\bar{h} = 3.0$). Shown are the steady ridge profiles (solid curves) together with the sum of the ridge profile and the eigenfunction multiplied by a small constant δ (dashed curve). In the first case the contact line stays fixed, in the second case it is shifted.

eigenfunction. This means that this instability leads to the formation of droplets *on* the MWS and therefore belongs to the morphologies I to III observed in the experiments, which are sketched in Fig. 8.2 (c).

In the region $\bar{h}_2 < \bar{h} < \bar{h}_3$ the critical eigenfunction has still only one maximum, but the growth rates are negative for finite wavenumbers (and zero for $q = 0$). In this region a ridge on the MWS is stable as it is no longer possible for the ridge to form droplets *on* the MWS. This can be seen from the critical eigenfunction for $\bar{h} = 2.1$ in Fig. 11.12. It becomes broader than the MWS. Since in this region it is not yet energetically favorable for the ridge to leave the stripe, the ridge is stabilized by the wettability pattern. This corresponds to the morphology of type V seen in the experiments (cf. 8.2 (c)).

For mean film heights above $\bar{h}_3$ it becomes energetically favorable for the liquid to partly cover also the LWS and the maximal growth rate becomes positive (cf. Fig. 11.13 (a)). At a critical film thickness of $\bar{h}^* \approx 2.5$, slightly greater than $\bar{h}_3 \approx 2.4$, the critical eigenfunction undergoes a shape transition from unimodal to bimodal. This is the instability that leads to the formation of bulges. This situation is sketched in the bottom panel of Fig. 11.14 for $\bar{h} = 3.0$. Here, the eigenfunction shifts the contact line region of the ridge. Therefore, the region $\bar{h} > \bar{h}_3$ corresponds to morphologies of type VI (cf. Fig. 8.2 (c)).

11.3.4 Small wettability contrasts

For small wettability contrasts ($\rho \lesssim 0.43$) we observe the same shape transition in the critical eigenmode, but the maximal growth rate remains positive for $\bar{h}$ above the curve in Fig. 11.10. This is demonstrated in Fig. 11.13 (b) for $\rho = 0.3$. Therefore, no stable ridge solutions exist for small wettability contrasts.

Finally we remark that at $\rho = 0$ the curve of the instability threshold in Fig. 11.10 reaches the value $\bar{h} \approx 1.26$. The same is true for the case with the sinusoidal wettability modulation (cf. Fig. 11.5). This value of $\bar{h} \approx 1.26$ corresponds, as it should be, to the analytically obtained threshold of the spinodal instability of a flat film, which is given by $\partial \Pi / \partial h = 0$ (cf. Eq. (9.37) in Sect. 9.5). This reinforces the interpretation that the first instability for small ρ and $\bar{h}$ is a spinodal instability. As one increases ρ from zero to a small finite values while keeping $\bar{h}$ constant, the 1d flat film solutions change towards more and more pronounced droplet solutions with increasing maximal film heights. This explains why the instability threshold with respect to $\bar{h}$ decreases with increasing ρ.

11.3.5 Influence of the sharpness of the wettability transition

Next we investigate the influence of the sharpness of the wettability transition. The dotted line in Fig. 11.10 shows the stability threshold in the $[\rho, \bar{h}]$ plane for $l_s = 0.001$, i. e. for a sharper wettability transition. In this case, stable ridges are possible at all for lower wettability contrasts ρ. For small ρ the region in the parameter space of $\bar{h}$ where ridges are stable is also larger. This is because a larger wettability gradient increases the pinning effect. On the other hand, for $\rho \gtrsim 0.57$, the onset of the instability leading to bulge formation is shifted towards lower $\bar{h}$. This is probably due to the fact that the effective width of the MWS decreases with decreasing l_s.

11.4 Comparison to system with diffusive mobility

The steady state solutions obtained in this chapter were computed from Eq. (11.1), which does not depend on the mobility coefficient $Q(h)$ (cf. Eqs. (9.5) and (9.7)). Therefore, one expects to observe the same equilibrium structures also with different mobility coefficients. Only the time scales of the formation of the equilibrium structures depend on the mobility.

The cubic term of our employed mobility term is derived from the Navier-Stokes equation and therefore results from a convective motion of the molecules on the substrate. Although there is some experimental evidence that the deposited molecules are in the liquid state after deposition (cf. Sect. 8.1) it is not clear whether or not the molecules really move by convection, especially at very low film heights. Since single molecules can only diffuse along the substrate, there has to be a transition from diffusive transport to convective transport as the film height is increased. It is not clear at which minimal film height one can assume a convective mobility.

Diffusive transport results in a mobility linear in h. This can be inferred from the entropic contribution to the free energy functional of a thermodynamic field ϕ [CH58],

$$F_{\mathrm{ent}}[\phi] = C \int \mathrm{d}x \phi(x) \log \phi(x) \,, \tag{11.28}$$

with the functional derivative

$$\frac{\delta F_{\mathrm{ent}}}{\delta \phi} = C(\log \phi + 1) \,. \tag{11.29}$$

If the temporal evolution of ϕ is given by

$$\partial_t \phi = \partial_x \left[Q(\phi) \partial_x \frac{\delta F_{\mathrm{ent}}}{\delta \phi} \right] \tag{11.30}$$

$$= \partial_x \left[Q(\phi) \frac{C}{\phi} \partial_x \phi \right] \,, \tag{11.31}$$

a linear mobility $Q(\phi) = \tilde{D}\phi$ leads to the diffusion equation

$$\partial_t \phi = D \partial_x^2 \phi \tag{11.32}$$

with $D = \tilde{D}C$. Thus, if we interpret the film height h as a thermodynamic field, diffusive transport results in a linear mobility coefficient.

In order to compare our findings to the case of diffusive transport, we repeat the calculations leading to Fig. 11.13 (a) with a mobility[2] $Q(h) = h$. The result is depicted in Fig. 11.15. While the fastest growing wavenumbers are almost identical for both transport times, the growth rates β differ dramatically. One should stress that we cannot make any statement about the absolute level of the growth rates since a prefactor in the mobility term has been scaled out. But what we can say is that the growth rates for larger film heights are, as expected, much smaller than for smaller film heights as compared to the case of diffusive transport. However, as expected, the stability thresholds $\bar{h}_1$, $\bar{h}_2$, $\bar{h}_3$ do not depend on the mobility term.

---

[2] By rescaling time in the thin film equation, one can easily get rid of a constant prefactor of the mobility term

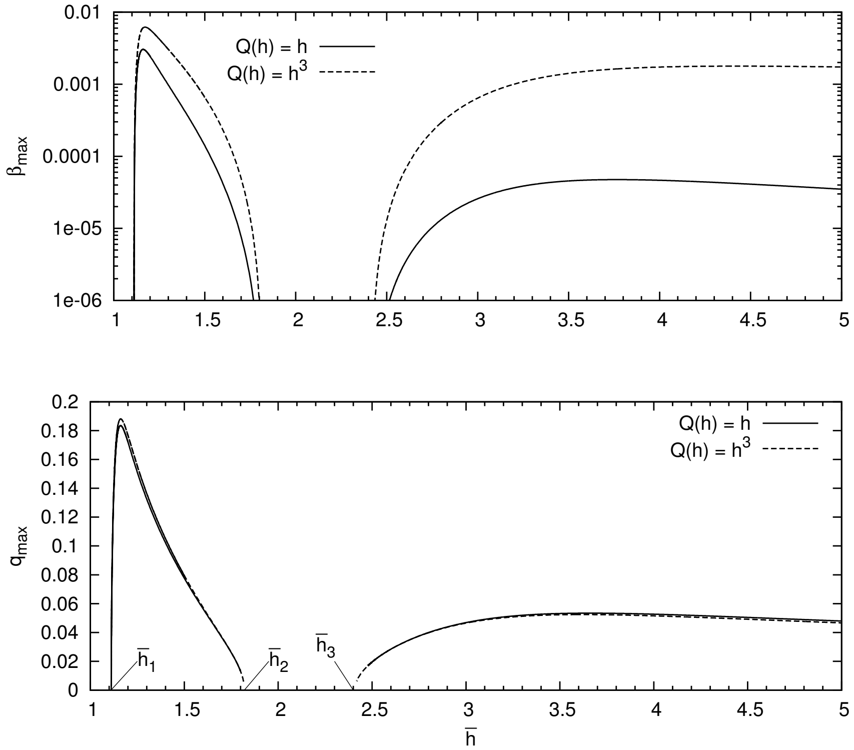

Fig. 11.15 Top: Maximal growth rates of the transversal instability for $\rho = 0.5$ against $\bar{h}$. The dotted line corresponds to a convective mobility. This curve is the same as in Fig. 11.13 (a), only in logarithmic scaling. The solid line corresponds to a diffusive mobility term. Bottom: The corresponding fastest growing wavenumbers. The growth rates are significantly larger for the convective instability, especially in the bulge formation regime. The fastest growing wavenumbers are almost identical for both mobilities. Also the stability thresholds remain the same.

12 Results of the DNS

The results of the transversal stability analysis presented in the previous chapter indicate that for low film heights and wettability contrasts, a ridge undergoes an instability towards droplets that are located only on the MWS and belong to the morphologies of type I to III rather than the bulges of type VI (cf. Fig. 8.2 (c)). In Sect. 12.1 we test this hypothesis by a DNS of Eq. (9.24) in this parameter regime. Section 12.2 presents a similar simulation with a mobility term that is only linear in h, corresponding to a diffusive transport behavior. Finally, Sect. 12.3 discusses a DNS in the parameter regime where bulge formation is expected.

12.1 Droplets on the MWS

We choose a wettability contrast $\rho = 0.5$ and an initial film height $\bar{h} = 1.16$, which corresponds to the largest maximal growth rate $\beta_{\max}$ w. r. t. $\bar{h}$ and roughly coincides with the maximum in the corresponding fastest growing wavenumber $q_{\max}$ (cf. Fig. 11.13). This has the advantage that the wavelength of the transversal instability is minimal and we can select a smaller domain size in y direction. At $\bar{h} = 1.16$, $q_{\max} \approx 0.188$, which corresponds to a fastest growing wavelength $\Lambda_{\max} = 2\pi/q_{\max} \approx 33$. We set the domain size in y direction to 100, such that three wavelengths fit into the domain. For the spatial discretization we use 230×200 grid points and employ a nine-point finite difference stencil, whose coefficients are listed in Tab. 10.1. Periodic boundary conditions are applied in both x and y direction.

During the time simulation, the free energy functional, Eq. (9.9), is measured. Figure 12.1 shows the corresponding time series. We can identify four energy plateaus. Each plateau corresponds to a transient configuration that is closely related to a steady state solution. They are shown in Figure 12.2. The last one is the final absolutely stable state.

Starting from a flat film configuration which is slightly perturbed by white noise, the first plateau is reached very quickly after about 200 dimensionless time units. This plateau corresponds to a configuration with a uniform ridge centered on the MWS (cf. top left panel of Fig. 12.2). Figure 12.3 shows the profile of this ridge configuration. For comparison, also the profile obtained by steady state continuation is shown. Both profiles agree perfectly. This proves that the state considered in the transversal linear

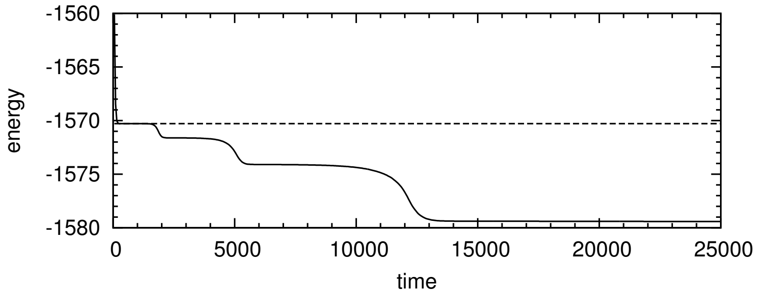

Fig. 12.1 Time series of the energy during a simulation of the thin film equation (9.24) with $\bar{h} = 1.16$ and $\rho = 0.5$ (solid curve). The dashed horizontal line shows the energy corresponding to the ridge profile computed by steady state continuation (cf. Chap. 11). It coincides with the level of the first energy plateau. The configurations that correspond to the four energy plateaus are plotted in Fig. 12.2.

stability analysis presented in Chap. 11 is really assumed (and maintained for a long time) during the dynamical evolution, even if it is linearly unstable. This justifies the approach of Chap. 11 retrospectively.

It takes approximately 1400 more time units until the ridge begins to break up into three droplets. Since the domain size in y direction is approximately three times the wavelength of the fastest growing mode of the transversal instability, at first three droplets are formed on the MWS (cf. top right panel of Fig. 12.2). Two of them vanish in successive coarsening events. Thereby the volume of the vanishing droplet is transferred to the neighboring droplet(s) while the centers of all droplets hardly move. Eventually, only one droplet remains that is slightly elongated in the stripe direction (cf. bottom panels of Fig. 12.2). Figure 12.4 shows a cut through the drop profile at $y = 10$, the broadest part of the drop, together with the wettability profile. We see that the drop is still pinned to the MWS. This confirms our hypothesis about the instability for small film thicknesses that was stated in Sect. 11.3.

12.2 Comparison to diffusive mobility

We repeat the same simulation of the previous section, but replace the cubic mobility term $Q(h) = h^3$ in Eq. (9.24) by a linear one, $Q(h) = h$, which corresponds to a diffusive transport behavior. Thereby, the same sequence of transient configurations is passed, only the time scales change as can be seen in Fig. 12.5, which shows the energy time series of the diffusive simulation together with the convective case. This observation is in agreement with the discussion in Sect. 11.4.

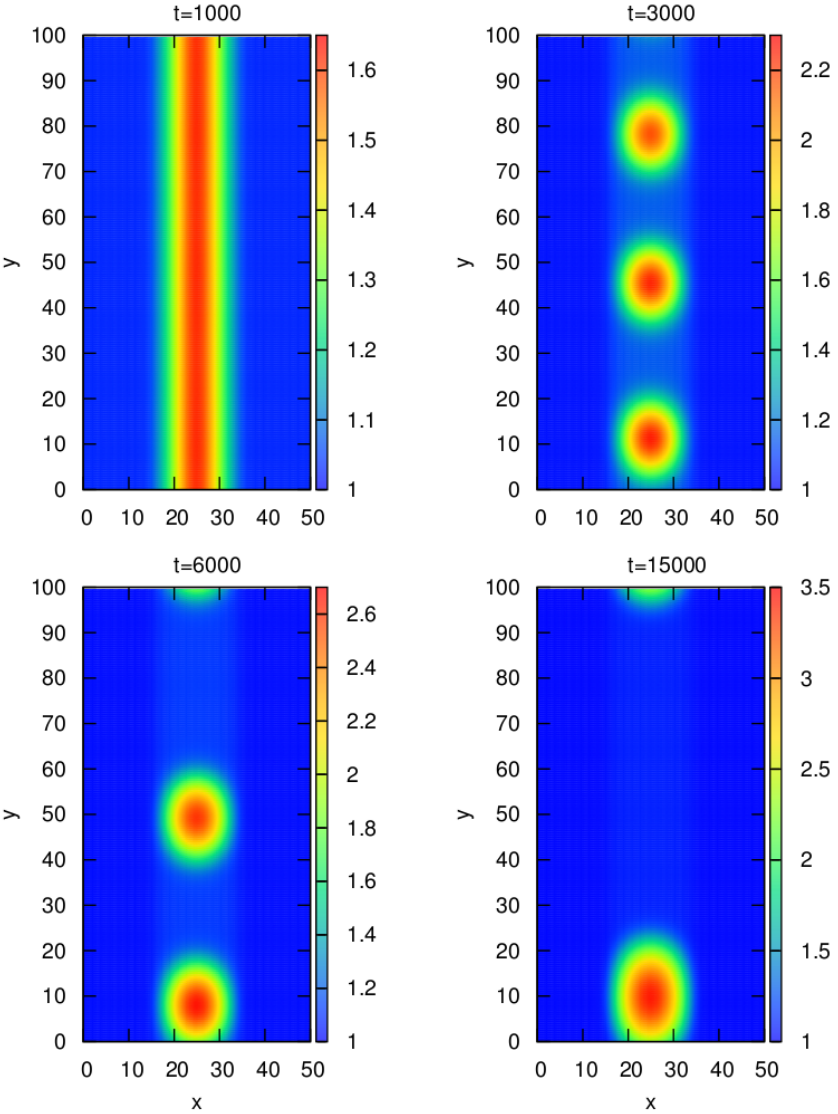

Fig. 12.2 Snapshots of a time simulation of the thin film equation (9.24) with $\bar{h} = 1.16$ and $\rho = 0.5$. Figure 12.1 shows the time series of the energy of the same simulation. The four snapshots at times $t = 1000$ (top left), $t = 3000$ (top right), $t = 6000$ (bottom left), and $t = 15000$ (bottom right) correspond to the four energy plateaus in Fig. 12.1.

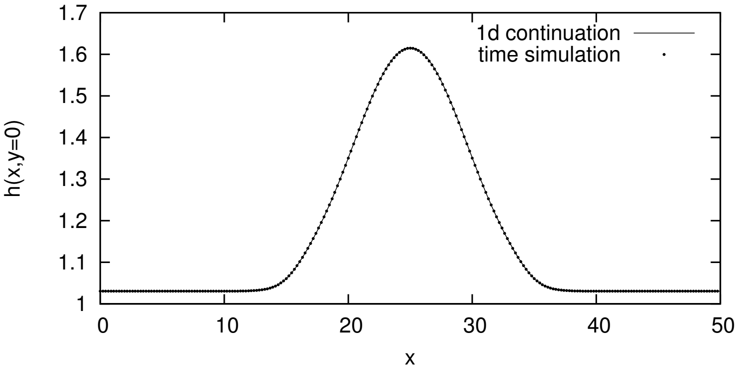

Fig. 12.3 Comparison between the time simulation and the 1d continuation. The solid line shows the result of the 1d continuation, the dots show a cut through the ridge configuration at $y = 0$ and $t = 1000$. No deviations can be seen by eye.

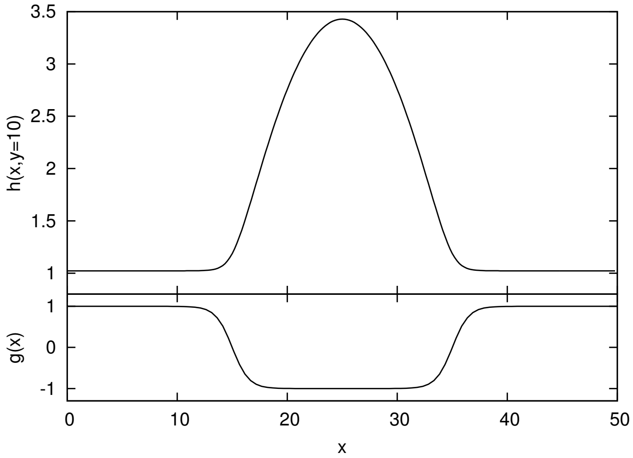

Fig. 12.4 Top: Cut through the final droplet at $y = 10$. Bottom: Wettability profile $g(x)$. The droplet is pinned to the MWS. This configuration belongs to the morphologies of type II (cf. Fig. 8.2 (c)).

12.3 Bulge formation

Now we perform a simulation in the parameter regime where, according to Sect. 11.3, bulge formation is expected to occur. Justified by the discussions of Sects. 11.4 and 12.2, we select a diffusive mobility term $Q(h) = h$, because this makes the numerics more stable. Again, we set ρ to 0.5, but choose a larger initial film height $\bar{h} = 2.8$. The fastest growing wave number is $q_{\max} \approx 0.04$ which corresponds to a wavelength $\Lambda_{\max} \approx 157$. Therefore we choose the domain size in y direction as $L_y = 300$. In x direction the domain size is again $L_x = 50$. We employ a 210×210 grid, periodic

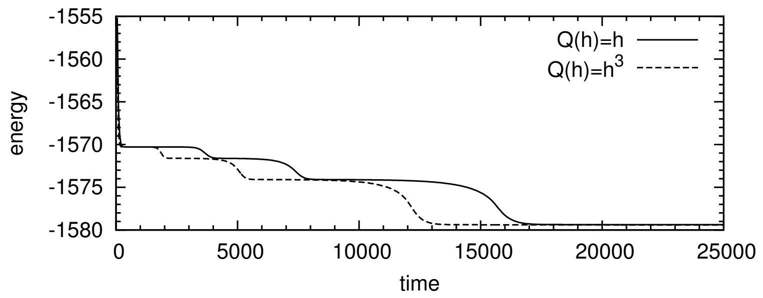

Fig. 12.5 Time series of the energy during a simulation with the same parameters as in Fig. 12.1 for diffusive mobility (solid curve) and a convective mobility (dashed curve). The diffusive case shows the same energy plateaus, only the time scales are larger as compared to the convective case.

boundary conditions in both x and y direction, and a 15 point finite difference stencil, whose coefficients are listed in Tab. 10.2.

Figure 12.6 shows four snapshots from the time simulation. As in the simulations of Sect. 12.1, the homogeneous ridge configuration (panel (a) in Fig. 12.6) is assumed quickly. The system stays close to this unstable steady state for a long time. Eventually the ridge shows undulations in y direction (panel (b)). These undulations grow and form large bulges (panel (c)). Finally, the material between two neighboring bulges is soaked up by the bulges (panel (d)). The emerged configurations resemble the experimental AFM image shown in Fig. 8.2 (d).

When the bulge configuration is assumed, the spatial resolution is too low to compute the large derivatives in y direction with sufficient accuracy. As a consequence, the norm

$$\mathcal{N} = \frac{1}{L_x L_y \bar{h}} \int_0^{L_x} \mathrm{d}x \int_0^{L_y} \mathrm{d}y\, h(x,y)\,, \tag{12.1}$$

which should stay constant at $\mathcal{N} = 1$, is observed to decrease rapidly in the time simulation. At time $t = 1.045 \cdot 10^6$ (panel (d)), $\mathcal{N}$ is still larger than 0.99, i. e., more than 99% of the initial volume is conserved. However, because of the subsequent, numerically caused evaporation, one cannot be sure whether the configuration shown in panel (*d*) is the final, absolutely stable state. It is possible that the remaining bulges will coarsen on a long time scale in a similar manner as in the simulations of the previous sections such that only one bulge remains in the end.

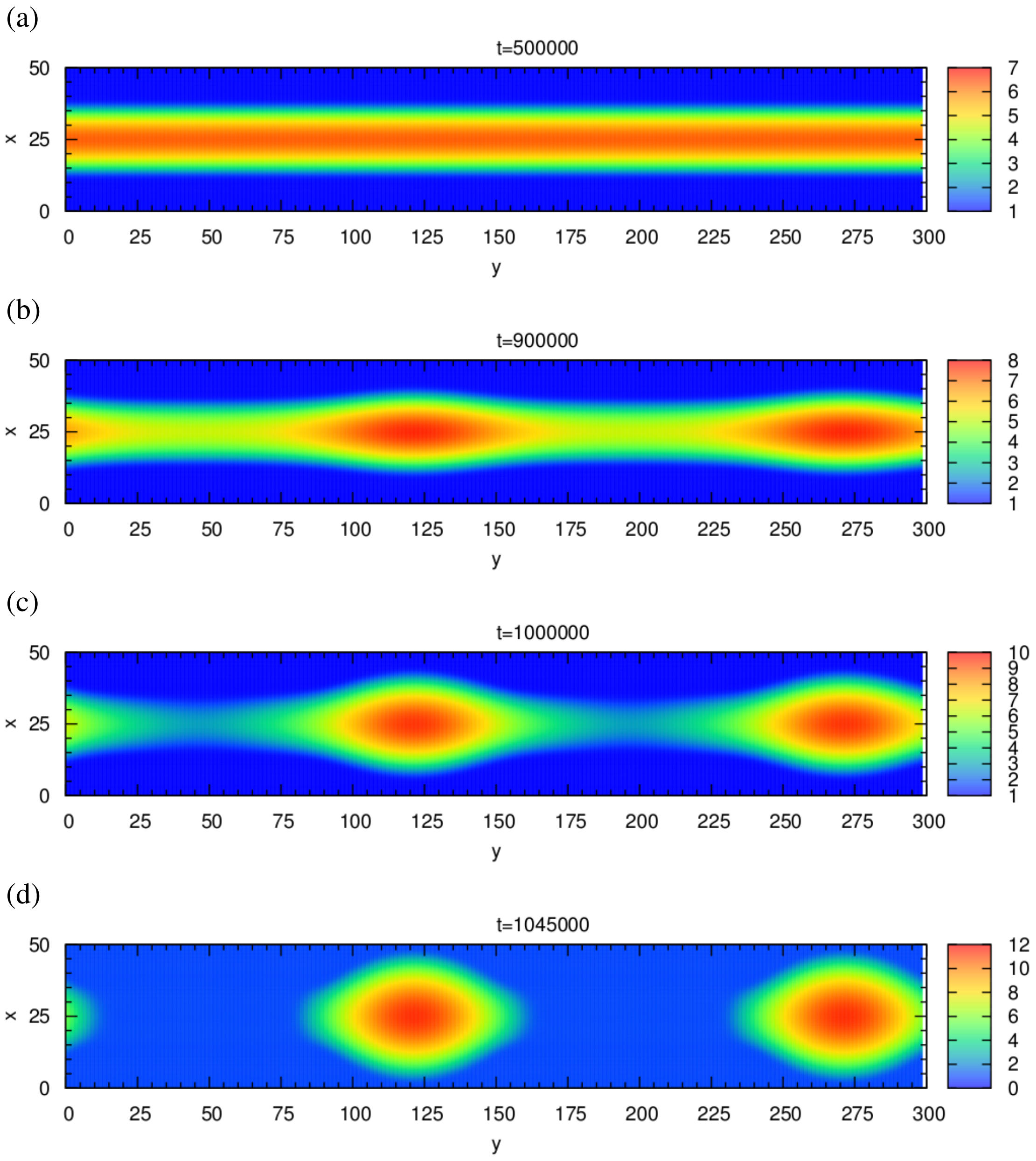

Fig. 12.6 Snapshots of a time simulation of the thin film equation (9.24) with $\bar{h} = 2.8$ and $\rho = 0.5$ and a diffusive mobility term $Q(h) = h$. Panels (a), (b), (c), and (d) show snapshots at times $t = 0.5 \cdot 10^6$, $t = 0.9 \cdot 10^6$, $t = 1.0 \cdot 10^6$, and $t = 1.045 \cdot 10^6$, respectively.

13 Conclusion

In the second part of the thesis we have investigated the pattern formation of a thin layer of small organic molecules on a substrate with a periodic chemical stripe pattern which was studied experimentally before. To this end, a thin film equation was employed that describes the temporal evolution of the height profile of the molecule layer.

In Chap. 11 the stability of steady state solutions which correspond to homogeneous ridges centered on stripes with increased wettability was analyzed employing numerical continuation techniques. Thereby, two types of instabilities were found that were also observed in the experiments. For small layer thicknesses ridges can break up into small droplets that are pinned to the MWS. For large layer thicknesses ridges can develop large bulges that also cover the region between two neighboring MWSs. For sufficiently large wettability contrasts the ridges are stable for intermediate layer thicknesses. A linear stability diagram in the parameter space of the mean layer thickness and the wettability contrast was determined for a fixed stripe geometry. Furthermore, the influence of the mobility of the molecules on the stability of ridge solutions was investigated. It was found that the stability thresholds do not depend on whether the molecules move by convection or by diffusion. Only the *time scales* of the instabilities are influenced by the mobility.

The outline of the transversal linear stability analysis employing numerical continuation was introduced in Refs. [BKTB02, TBBB03]. In these works the diffuse interface model for the disjoining pressure [PP00] is used together with a sinusoidal wettability profile. In [BKTB02] the transversal instability is studied only for fixed mean film height and for a single stripe in dependence of the wettability contrast and the period of the stripe pattern. In [TBBB03] the authors also investigate the interaction of two neighboring stripes finding four major eigenfunctions that correspond to in-phase and anti-phase varicose and zigzag modes, respectively. A comprehensive analysis of the stability of ridges in dependence of various system parameters is not presented.

A very similar analysis is also presented in Ref. [MRD08]. The authors employ a disjoining pressure and a wettability profile that is qualitatively similar to the one considered here. But in this work only the second kind of instability for larger film heights, the bulge formation, is investigated. Instead of the mean film height $\bar{h}$, the excess cross section of the ridge

$$V = \int \mathrm{d}x(h_0(x) - h_p) \tag{13.1}$$

is used as a control parameter. This makes the results more independent of the overall system size as compared to the results presented here. However, the mean film height $\bar{h}$ is the quantity that is accessible by experimentalists. The authors find the stability criterion $\mathrm{d}P/\mathrm{d}V > 0$, where P is the generalized pressure inside the ridge, which corresponds to our parameter C in Eq. (11.1). This means that a ridge is stable with respect to bulge formation if the pressure increases with the cross-sectional area. For chemical channels with a smooth transition of equilibrium contact angles Θ_{eq}, they find the stability criterion $\frac{\mathrm{d}}{\mathrm{d}x} \ln \Theta_{\mathrm{eq}}(x) > \frac{1}{x}$, where x is the lateral distance from the stripe center. Furthermore, the influence of a body force parallel to the stripe is investigated. It turns out that a driven flow has a stabilizing effect on the ridge as it decreases the critical transversal wavenumber, but does not change the stability criteria. However, a linear stability diagram like Fig. 11.10 showing the stability of ridges depending on explicit system parameters has, to the author's best knowledge, not been presented in the literature before.

Our findings of the linear stability analysis were complemented by three direct numerical simulations of the thin film equation, presented in Chap. 12. The first simulation is performed in the parameter regime where the first kind of instability is predicted. As expected, the final absolutely stable configuration is a small droplet on the MWS. The second simulation is done with the same parameters but employs a diffusive mobility term instead of a convective one. The same kind of structures are seen, only the time scales of the dynamics change. The third simulation does also employ a diffusive mobility term and is carried out for parameters where bulge formation is predicted by the stability analysis. In this simulation the emerged bulges soak up the molecules between them, leaving parts of the MWS uncovered. Similar morphologies have been experimentally observed, however, more frequently one finds bulges on top of a regular ridge. Overall, the obtained results confirm the predictions of the linear stability analysis.

In the course of all simulated time evolutions the homogeneous ridge state is assumed very quickly and is maintained for quite a long time although it is linearly unstable. This shows that unstable steady states play an important role in the dynamics of nonlinear systems, which in turn demonstrates the power of continuation techniques which allow one to study also unstable steady states systematically.

Time simulations of a thin film equation for two-dimensional substrates with a chemical stripe pattern are also presented in Refs. [KS01, SBK$^+$12]. In both articles the wettability profile is a periodic step function. This is on the one hand unphysical because wettability profiles result from intermolecular interactions that vary smoothly in space. On the other hand it is problematic because the wettability gradient in the simulation then depends on the grid resolution. However, the focus of both articles does not lie in the instabilities of individual ridges, but on the way the geometry of stripe patterns influences the templating behavior. It is found that if the width of the LWSs are above a critical value, they do not dewet completely and are covered with droplets. If the width of the LWS is below another critical value, it might not dewet at all, or only every *n*th LWS might dewet. The critical values depend on specific length scales of the system. For intermediate widths, perfect templating can occur. Morphologies that resemble the bulges on top of regular ridges, as seen in the AFM image, Fig. 8.1 (a), are not observed in these simulations.

This thesis shows how the stability of homogeneous ridges, the morphology that is desired by experimentalists, can be analyzed systematically by continuation techniques. This analysis can be continued to study a larger variety of stripe geometries. Especially configurations with larger distances between MWSs are interesting. The experiments as well as the theoretical analysis in [SBK+12] show that for large distances droplets appear on the LWSs. Employing the methodology presented here, one could study systematically under which conditions these droplets emerge. Also many experiments employ stripe patterns of alternating widths of the MWS, like for instance, the AFM images of Fig. 2 of Ref. [WDW+11] show. Therefore, an analysis of such geometries would also be worthwhile.

Concerning the bulge formation, an interesting open question is whether or not the employed model does also contain equilibrium configurations corresponding to a bulge on top of a regular ridge. This is probably the case for different stripe geometries and mean layer thicknesses. This question cannot be answered by stability analyses and therefore requires more extensive time simulations. The DNSs presented here suffered from the problem that the library routine for the implicit time stepping had problems in the linear algebra routines that did not allow us to employ higher grid resolutions. This problem has to be solved in order to perform more extensive simulations.

Throughout the whole analysis the process of condensation was not considered. The system was treated as if the whole material was deposited onto the substrate instantaneously, forming an initial homogeneous layer. The similarity of the morphologies found in the DNSs with those seen in the experiments suggests that the system approaches nevertheless the same equilibrium structures. However, it would be interesting to study the influence of condensation (and different condensation rates) on the dynamics as well as on the final equilibrium morphologies.

A Existence of the second moment

In the following it is shown that the second moment of the stationary PDF of a Langevin process with $D^{(1)}(x) = -\gamma x$ and $D^{(2)}(x) = \alpha + \beta x^2$ exists for $\gamma > \beta$, and diverges otherwise. This is important because it explains why the corresponding finite time diffusion coefficient (4.17) diverges for $\beta \geq \gamma$ as τ goes to infinity. The following calculation shows that this is in accordance with Eq. (4.22b).

The stationary solution of the one-dimensional FPE for stationary drift and diffusion coefficients reads [Ris89]

$$f(x) = \frac{N}{D^{(2)}(x)} \exp\left\{ \int^{x} \frac{D^{(1)}(x')}{D^{(2)}(x')} \mathrm{d}x' \right\} . \tag{A.1}$$

For $D^{(1)}(x) = -\gamma x$ and $D^{(2)}(x) = \alpha + \beta x^2$ this yields

$$\begin{aligned} f(x) &= \frac{N}{\alpha + \beta x^2} \exp\left\{ -\frac{\gamma}{2\beta} \ln\left(1 + \frac{\beta}{\alpha} x^2\right) \right\} \\ &= \frac{N}{\alpha} \frac{\left(1 + \frac{\beta}{\alpha} x^2\right)^{-\frac{\gamma}{2\beta}}}{1 + \frac{\beta}{\alpha} x^2} \\ &= \frac{N}{\alpha} \left(1 + \frac{\beta}{\alpha} x^2\right)^{-\frac{\gamma}{2\beta} - 1} \end{aligned} \tag{A.2}$$

with the normalization constant

$$N = \frac{\sqrt{\alpha\beta}\,\Gamma\left(1 + \frac{\gamma}{2\beta}\right)}{\sqrt{\pi}\,\Gamma\left(\frac{\beta+\gamma}{2\beta}\right)} . \tag{A.3}$$

The second moment is defined as

$$\langle x^2 \rangle = \frac{N}{\alpha} \int_{-\infty}^{\infty} x^2 \left(1 + \frac{\beta}{\alpha} x^2\right)^{-\frac{\gamma}{2\beta} - 1} \mathrm{d}x . \tag{A.4}$$

For the existence of the integral, only the asymptotic behavior of the integrand for $x \to \pm\infty$ is important. This goes with $x^{-\frac{\gamma}{\beta}}$. We have

$$\int x^{-\frac{\gamma}{\beta}} \propto x^{-\frac{\gamma}{\beta}+1}, \tag{A.5}$$

so the second moment exists for $\gamma > \beta$.

Bibliography

[ABT05] R. C. Aster, B. Borchers, and C. H. Thurber, *Parameter estimation and inverse problems*, Elsevier Academic Press, 2005.

[ABV$^+$05] J. A. Acebrón, L. L. Bonilla, C. J. P. Vicente, F. Ritort, and R. Spigler, *The Kuramoto model: A simple paradigm for synchronization phenomena*, Rev. Mod. Phys. **77** (2005), 137.

[AGL09] G. Ahlers, S. Grossmann, and D. Lohse, *Heat transfer and large scale dynamics in turbulent Rayleigh-Bénard convection*, Rev. Mod. Phys. **81** (2009), 503.

[AMFL08] M. S. Arnold, G. J. McGraw, St. R. Forrest, and R. R. Lunt, *Direct vapor jet printing of three color segment organic light emitting devices for white light illumination*, Appl. Phys. Lett. **92** (2008), 053301.

[AQ10] C. Anteneodo and S. M. Duarte Queirós, *Low-sampling-rate Kramers-Moyal coefficients*, Phys. Rev. E **82** (2010), 041122.

[BD00] C. Bauer and S. Dietrich, *Phase diagram for morphological transitions of wetting films on chemically structured substrates*, Phys. Rev. E **61** (2000), 1664.

[BDP99] C. Bauer, S. Dietrich, and A. O. Parry, *Morphological phase transitions of thin fluid films on chemically structured substrates*, Europhys. Lett. **47** (1999), 474.

[BEI$^+$09] D. Bonn, J. Eggers, J. Indekeu, J. Meunier, and E. Rolley, *Wetting and spreading*, Rev. Mod. Phys. **81** (2009), 739.

[Ber55] A. Bernanose, *Electroluminescence of organic compounds*, Brit. J. Appl. Phys. **6** (1955), S54.

[BHYM03] S. Brandon, N. Haimovich, E. Yeger, and A. Marmur, *Partial wetting of chemically patterned surfaces: The effect of drop size*, J. Colloid Interface Sci. **263** (2003), 237.

[BKTB02] L. Brusch, H. Kühne, U. Thiele, and M. Bär, *Dewetting of thin films on heterogeneous substrates: Pinning versus coarsening*, Phys. Rev. E **66** (2002), 011602.

[BL02] M. Brinkmann and R. Lipowsky, *Wetting morphologies on substrates with striped surface domains*, J. Appl. Phys. **92** (2002), 4296.

[BM74] D. Bedeaux and P. Mazur, *Brownian motion and fluctuating hydrodynamics*, Physica **76** (1974), 247.

[BT10] P. Beltrame and U. Thiele, *Time Integration and Steady-State Continuation for 2d Lubrication Equations*, SIAM J. Appl. Dyn. Sys. **9** (2010), 484.

[CAR08] A. A. G. Cortines, C. Anteneodo, and R. Riera, *Stock index dynamics worldwide: a comparative analysis*, Eur. Phys. J. B **65** (2008), 289.

[CGT00] A. R. Conn, N. I. M. Gould, and P. L. Toint, *Trust-Region Methods*, SIAM, Society for Industrial and Applied Mathematics, 2000.

[CH58] J. W. Cahn and J. E. Hilliard, *Free Energy of a Nonuniform System. I. Interfacial Free Energy*, J. Chem. Phys. **28** (1958), 258.

[CJ08] R. Courant and F. John, *Introduction to Calculus and Analysis II/1*, Springer, 2008.

[CRA07] A. A. G. Cortines, R. Riera, and C. Anteneodo, *From short to fat tails in financial markets: a unified description*, Eur. Phys. J. B **60** (2007), 385.

[CS92] H. J. H. Clercx and P. P. J. Schram, *Brownian particles in shear flow and harmonic potentials: A study of long time tails*, Phys. Rev. A **46** (1992), 1942.

[Dav04] P. A. Davidson, *Turbulence: An introduction for scientists and engineers*, Oxford University Press, 2004.

[Del10] R. Delmdahl, *The excimer laser: Precision engineering*, Nature Photonics **4** (2010), 286.

[Der40] B. Derjaguin, Zh. Fiz. Khim. **14** (1940), 137.

[dG85] P.-G. de Gennes, *Wetting: Statics and dynamics*, Rev. Mod. Phys. **57** (1985), 827.

[DO13] E. J. Doedel and B. E. Oldeman, *AUTO-07p: Continuation and bifurcation software for ordinary differential equations*, Concordia University, Montreal, Canada, 2011. Available from: <http://indy.cs.concordia.ca/auto/>. [23 October 2013].

[Doe] E. J. Doedel, *Lecture Notes on Numerical Analysis of Nonlinear Equations*, available from: <http://indy.cs.concordia.ca/auto/notes.pdf> [23 October 2013].

[DTMW00] A. A. Darhuber, S. M. Troian, S. M. Miller, and S. Wagner, *Morphology of liquid microstructures on chemically patterned surfaces*, J. Appl. Phys. **87** (2000), 7768.

[FEB$^+$07] F. Farahpour, Z. Eskandari, A. Bahraminasab, G. R. Jafari, F. Ghasemi, M. Sahimi, and M. R. R. Tabar, *A Langevin equation for the rates of currency exchange based on the Markov analysis*, Phys. A **385** (2007), 601.

[For04] St. R. Forrest, *The path to ubiquitous and low-cost organic electronic appliances on plastic*, Nature **428** (2004), 911.

[FP97a] R. Friedrich and J. Peinke, *Description of a Turbulent Cascade by a Fokker-Planck Equation*, Phys. Rev. Lett. **78** (1997), 863.

[FP97b] R. Friedrich and J. Peinke, *Statistical properties of a turbulent cascade*, Physica D: Nonlinear Phenomena **102** (1997), 147.

[FPR00] R. Friedrich, J. Peinke, and C. Renner, *How to Quantify Deterministic and Random Influences on the Statistics of the Foreign Exchange Market*, Phys. Rev. Lett. **84** (2000), 5224.

[FPST11] R. Friedrich, J. Peinke, M. Sahimi, and M. R. R. Tabar, *Approaching complexity by stochastic methods: From biological systems to turbulence*, Phys. Rep. **506** (2011), 87.

[FPT09] R. Friedrich, J. Peinke, and M. R. R. Tabar, *Fluctuations, importance of: Complexity in the view of stochastic processes*, Encyclopedia of Complexity and Systems Science (R. A Meyers, ed.), Springer, 2009, p. 3574.

[FRSP02] R. Friedrich, Ch. Renner, M. Siefert, and J. Peinke, *Comment on "Indispensable Finite Time Corrections for Fokker-Planck Equations from Time Series Data"*, Phys. Rev. Lett. **89** (2002), 149401.

[Gar86] C. W. Gardiner, *Handbook of Stochastic Methods*, 2nd sub ed., Springer Series in Synergetics, Springer, 1986.

[GBSM+06] F. Ghasemi, A. Bahraminasab, M. Sadegh Movahed, S. Rahvar, K. R. Sreenivasan, and M. R. R. Tabar, *Characteristic angular scales in cosmic microwave background radiation*, J. Stat. Mech. (2006).

[GHLL99] H. Gau, St. Herminghaus, P. Lenz, and R. Lipowsky, *Liquid morphologies on structured surfaces: From microchannels to microchips*, Science **283** (1999), 46.

[GMR06] G. Grün, K. Mecke, and M. Rauscher, *Thin-film flow influenced by thermal noise*, Journal of Statistical Physics **122** (2006), 1261.

[GPST05] F. Ghasemi, J. Peinke, M. Sahimi, and M. Reza Rahimi Tabar, *Regeneration of stochastic processes: an inverse method*, Eur. Phys. J. B **47** (2005), 411.

[GPTS06] F. Ghasemi, J. Peinke, M. R. R. Tabar, and M. Sahimi, *Statistical properties of the interbeat interval cascade in human hearts*, Int. J. Mod. Phys. C **17** (2006), 571.

[GSPT06] F. Ghasemi, M. Sahimi, J. Peinke, and M. Reza Rahimi Tabar, *Analysis of Non-stationary Data for Heart-rate Fluctuations in Terms of Drift and Diffusion Coefficients*, J. Biol. Phy. **32** (2006), 117.

[Hak85] H. Haken, *Light, Volume 2 - Laser light dynamics*, North-Holland, 1985.

[Hak00] ______, *Information and self-organization*, 2nd enlarged ed., Springer Series in Synergetics, Springer, 2000.

[Hak04] ______, *Synergetics: Introduction and Advanced Topics*, 3rd repr. ed., Springer Series in Synergetics, Springer, 2004.

[Hak09] ______, *Synergetics: Basic concepts*, Encyclopedia of Complexity and Systems Science, Springer New York, 2009.

[HF11] C. Honisch and R. Friedrich, *Estimation of Kramers-Moyal coefficients at low sampling rates*, Phys. Rev. E **83** (2011), 066701.

[HFHD12] C. Honisch, R. Friedrich, F. Hörner, and C. Denz, *Extended Kramers-Moyal analysis applied to optical trapping*, Phys. Rev. E **86** (2012), 026702.

[HFS+00] St. Herminghaus, A. Fery, St. Schlagowski, K. Jacobs, R. Seemann, H. Gau, W. Mönch, and T. Pompe, *Liquid microstructures at solid interfaces*, J. Phys.: Condens. Matter **12** (2000), A57.

[HKB85] H. Haken, J. A. S. Kelso, and H. Bunz, *A Theoretical Model of Phase Transitions in Human Hand Movements*, Biol. Cybern. **51** (1985), 347.

[HMSW04] W. Härdle, M. Müller, St. Sperlich, and A. Werwatz, *Nonparametric and Semiparametric Models*, Springer Series in Statistics, Springer, 2004.

[HS71] C. Huh and L. E. Scriven, *Hydrodynamic model of steady movement of a solid/liquid/fluid contact line*, J. of Colloid and Interface Science **35** (1971), 85.

[Isr11] J. N. Israelachvili, *Intermolecular and surface forces*, 3rd ed., Academic Press, London, 2011.

[JFG$^+$03] G. R. Jafari, S. M. Fazeli, F. Ghasemi, S. M. Vaez Allaei, M. Reza Rahimi Tabar, A. Iraji zad, and G. Kavei, *Stochastic Analysis and Regeneration of Rough Surfaces*, Phys. Rev. Lett. **91** (2003), 226101.

[Joh] V. John, *Lecture notes: Numerical methods for ordinary differential equations*, available from: <www.wias-berlin.de/people/john/LEHRE/NUMERIK_II/ode_2.pdf>. [10 September 2013].

[KBF00] C. Kim, P. E. Burrows, and St. R. Forrest, *Micropatterning of Organic Electronic Devices by Cold-Welding*, Science **288** (2000), 831.

[KF07] D. Kleinhans and R. Friedrich, *Maximum likelihood estimation of drift and diffusion functions*, Phys. Lett. A **368** (2007), 194.

[KFNP05] D. Kleinhans, R. Friedrich, A. Nawroth, and J. Peinke, *An iterative procedure for the estimation of drift and diffusion coefficients of Langevin processes*, Phys. Lett. A **346** (2005), 42.

[KKS00a] K. Kargupta, R. Konnur, and A. Sharma, *Instability and Pattern Formation in Thin Liquid Films on Chemically Heterogeneous Substrates*, Langmuir **16** (2000), 10243.

[KKS00b] R. Konnur, K. Kargupta, and A. Sharma, *Instability and Morphology of Thin Liquid Films on Chemically Heterogeneous Substrates*, Phys. Rev. Lett. **84** (2000), 931.

[KM94] A. J. Koch and H. Meinhardt, *Biological pattern formation: from basic mechanisms to complex structures*, Rev. Mod. Phys. **66** (1994), 1481.

[KMKT11] S. Kimiagar, M. S. Movahed, S. Khorram, and M. R. R. Tabar, *Markov Properties of Electrical Discharge Current Fluctuations in Plasma*, J. Stat. Phys. **143** (2011), 148.

[KP99] P. E. Kloeden and E. Platen, *Numerical Solution of Stochastic Differential Equations*, corr. ed., Stochastic Modelling and Applied Probability, Springer, 1999.

[KS01] K. Kargupta and A. Sharma, *Templating of Thin Films by Dewetting on Patterned Surfaces*, Phys. Rev. Lett. **86** (2001), 4536.

[KS03] H. Kantz and T. Schreiber, *Nonlinear Time Series Analysis*, 2nd ed., Cambridge University Press, 2003.

[KTH91] R. Kubo, M. Toda, and N. Hashitsume, *Statistical Physics II: Nonequilibrium Statistical Mechanics*, 2nd ed., Springer Series in Solid-State Sciences, Springer, 1991.

[Lad09] St. J. Lade, *Finite sampling interval effects in Kramers-Moyal analysis*, Phys. Lett. A **373** (2009), 3705.

[LBD+05] R. Lipowsky, M. Brinkmann, R. Dimova, T. Franke, J. Kierfeld, and X. Zhang, *Droplets, bubbles, and vesicles at chemically structured surfaces*, J. Phys.: Condens. Matter **17** (2005), S537.

[Leh11] B. Lehle, *Analysis of stochastic time series in the presence of strong measurement noise*, Phys. Rev. E **83** (2011), 021113.

[Leh13] ______, *Stochastic Time Series with Strong, Correlated Measurement Noise: Markov Analysis in N Dimensions*, J. Stat. Phys. **152** (2013), 1145.

[LL00] P. Lenz and R. Lipowsky, *Stability of droplets and channels on homogeneous and structured surfaces*, Eur. Phys. J. E **1** (2000), 249.

[LL09] D. Lamouroux and K. Lehnertz, *Kernel-based regression of drift and diffusion coefficients of stochastic processes*, Phys. Lett. A **373** (2009), 3507.

[LMW+12] F. Lied, T. Mues, W. Wang, L. Chi, and A. Heuer, *Different growth regimes on prepatterned surfaces: Consistent evidence from simulations and experiments*, J. Chem. Phys. **136** (2012), 024704.

[LPF+10] M. Langner, J. Peinke, F. Flemisch, M. Baumann, and D. Beckmann, *Drift and Diffusion based models of driver behavior*, Eur. Phys. J. B **76** (2010), 99.

[LS03] B. Lohmann and B. Salimbahrami, *Introduction to Krylov-Subspace Methods in Model Order Reduction*, Methoden und Anwendungen der Automatisierungstechnik. Ausgewählte Beiträge der internat. automatisierungstechnischen Kolloquien Salzhausen 2001 und 2002. (B. Lohmann and A. Gräser, eds.), Shaker, 2003.

[Mat] Wolfram Mathematica 9, computer software 2013. Available from: <http://www.wolfram.com/mathematica/>. [23 October 2013].

[Mit93] V. S. Mitlin, *Dewetting of solid surface: Analogy with spinodal decomposition*, Journal of Colloid and Interface Science **156** (1993), 491.

[MKL] Intel Math Kernel Library, computer software 2013. Available from: <http://software.intel.com/en-us/articles/intel-mkl/>. [23 October 2013].

[MRD08] S. Mechkov, M. Rauscher, and S. Dietrich, *Stability of liquid ridges on chemical micro- and nanostripes*, Phys. Rev. E **77** (2008), 061605.

[Mue12] T. Mues, *Wachstumsprozesse auf Oberflächen*, Ph.D. thesis, Westfälische Wilhelms-Universität Münster, 2012.

[NAG] The NAG Fortran Library, computer software 2013. Available from: <http://http://www.nag.co.uk/numeric/fl/FLdescription.asp>. [25 November 2013].

[ODB97] A. Oron, St. H. Davis, and S. G. Bankoff, *Long-scale evolution of thin liquid films*, Rev. Mod. Phys. **69** (1997), 931.

[OMP] OpenMP Application Program Interface. Available from: <www.openmp.org>. [19 November 2013].

[Pis02] L. M. Pismen, *Mesoscopic hydrodynamics of contact line motion*, Colloid Surf. A-Physicochem. Eng. Asp. **206** (2002), 11.

[PM03] A. Pikovsky and Y. L. Maistrenko, *Synchronization: Theory and Application*, Springer, 2003.

[PP00] L. Pismen and Y. Pomeau, *Disjoining potential and spreading of thin liquid layers in the diffuse-interface model coupled to hydrodynamics*, Phys. Rev. E **62** (2000), 2480.

[RD08] M. Rauscher and S. Dietrich, *Wetting Phenomena in Nanofluidics*, Annu. Rev. Mater. Res. **38** (2008), 143.

[Ris89] H. Risken, *The Fokker-Planck Equation*, 2nd ed., Springer Series in Synergetics, Springer, 1989.

[SBK⁺12] A. Sehgal, D. Bandyopadhyay, K. Kargupta, A. Sharma, and A. Karim, *From finite-amplitude equilibrium structures to dewetting in thin polymer films on chemically patterned substrates*, Soft Matter **8** (2012), 10394.

[SFP98] S. Siegert, R. Friedrich, and J. Peinke, *Analysis of data sets of stochastic systems*, Phys. Lett. A **243** (1998), 275.

[SJA⁺05] P. Sangpour, G. R. Jafari, O. Akhavan, A. Z. Moshfegh, and M. Reza Rahimi Tabar, *Controlling surface statistical properties using bias voltage: Atomic force microscopy and stochastic analysis*, Phys. Rev. B **71** (2005), 155423.

[SK98] A. Sharma and R. Khanna, *Pattern Formation in Unstable Thin Liquid Films*, Phys. Rev. Lett. **81** (1998), 3463.

[Son] Sony XEL-1. Available from: <http://www.sony.de/product/tv-28-11-oled/xel-1>. [23 October 2013].

[SP06] M. Siefert and J. Peinke, *Joint multi-scale statistics of longitudinal and transversal increments in small-scale wake turbulence*, J. Turbulence **7** (2006), 1.

[Sur02] P. Sura, *Stochastic Analysis of Southern and Pacific Ocean Sea Surface Winds*, J. Atm. Sc. **60** (2002), 654.

[SV09] V. M. Starov and M. G. Velarde, *Surface forces and wetting phenomena*, J. Phys.-Condes. Matter **21** (2009), 464121.

[TAY13] K Tang, P. Ao, and B. Yuan, *Robust reconstruction of the Fokker-Planck equations from time series at different sampling rates*, Europhys. Lett. **102** (2013), 40003.

[TBB⁺99] P. F. Tian, V. Bulovic, G. Burrows, P. E. nad Gu, S. R. Forrest, and T. X. Zhou, *Precise, scalable shadow mask patterning of vacuum-deposited organic light emitting devices*, J. Vac. Sci. Technol. A **17** (1999), 2975.

[TBBB03] U. Thiele, L. Brusch, M. Bestehorn, and M. Bär, *Modelling thin-film dewetting on structured substrates and templates: Bifurcation analysis and numerical simulations*, Eur. Phys. J. E **11** (2003), 255.

[TGP$^+$06] M. R. R. Tabar, F. Ghasemi, J. Peinke, R. Friedrich, K. Kaviani, F. Taghavi, S. Sadeghi, G. Bizhani, and M. Sahimi, *New Computational Approaches to the Analysis of Interbeat Interval in Human Subjects*, Comp. Sim. **8** (2006), 54.

[Thi10] U. Thiele, *Thin film evolution equations from (evaporating) dewetting liquid layers to epitaxial growth*, J. Phys.-Cond. Mat. **22** (2010), 084019.

[Thi11] ______, *Note on thin film equations for solutions and suspensions*, Eur. Phys. J. Special Topics **197** (2011), 213.

[TM04] M. Tutkun and L. Mydlarski, *Markovian properties of passive scalar increments in grid-generated turbulence*, New J. Phys. **6** (2004), 49.

[VK07] N. G. Van Kampen, *Stochastic Processes in Physics and Chemistry*, 3rd ed., North Holland, 2007.

[WC12] W. Wang and L. Chi, *Area-Selective Growth of Functional Molecular Architectures*, Acc. Chem. Res. **45** (2012), 1646.

[WDB$^+$10] W. Wang, C. Du, H. Bi, Y. Sun, Y. Wang, C. Mauser, E. Da Como, H. Fuchs, and L. Chi, *Tunable Multicolor Ordered Patterns with Two Dye Molecules*, Advanced Materials **22** (2010), 2764.

[WDW$^+$11] W. Wang, C. Du, C. Wang, M. Hirtz, L. Li, J. Hao, Q. Wu, R. Lu, N. Lu, Y. Wang, H. Fuchs, and L. Chi, *High-Resolution Triple-Color Patterns Based on the Liquid Behavior of Organic Molecules*, Small **7** (2011), 1403.

[WDZ$^+$09] W. Wang, C. Du, D. Zhong, M. Hirtz, Y. Wang, N. Lu, L. Wu, D. Ebeling, L. Li, H. Fuchs, and L. Chi, *Control over Patterning of Organic Semiconductors: Step-Edge-Induced Area-Selective Growth*, Advanced Materials **21** (2009), 4721.

Lebenslauf

Der Lebenslauf ist in dieser digital publizierten Version nicht enthalten.

Danksagung

Eine Promotion hat viele Gemeinsamkeiten mit der Erstbesteigung eines schwierigen Berges. Niemand kann im Vorhinein sagen, ob der angepeilte Weg tatsächlich zum Gipfel führt. Oft läuft man lange Zeit in eine bestimmte Richtung, stellt dann fest, dass man umkehren und einen anderen Weg probieren muss. Es können allerhand unvorhergesehene Dinge passieren, die die Expedition manchmal erheblich erschweren. Doch wenngleich man die einzelnen Schritte bis zum Gipfel selbständig gehen muss, wird das Unterfangen erheblich durch eine gut funktionierende Seilschaft erleichtert. Bei eben dieser "Seilschaft“ möchte ich mich im Folgenden bedanken und freue mich schon auf den gemeinsamen Gipfelschnaps.

Zunächst danke ich Prof. Dr. Rudolf Friedrich, der mich während meiner Diplomarbeit und der ersten zwei Jahre meiner Promotion betreute. Ihm verdanke ich die Freiheit und das Selbstbewusstsein, weitgehend selbständig wissenschaftlich arbeiten zu können. Außerdem bin ich dafür dankbar, dass es ihm durch seine wissenschaftlichen Fähigkeiten und seine humorvolle Art gelang, so viele wunderbare Menschen um sich zu versammeln, mit denen ich die letzten Jahre zusammenarbeiten durfte. Sein unerwarteter Tod im August 2012 war nicht nur in wissenschaftlicher Hinsicht ein großer Verlust für mich.

In diesem Zusammenhang möchte ich ganz besonders Dr. Svetlana Gurevich, Dr. Michael Wilczek und Dr. Oliver Kamps danken, die nach Herrn Friedrichs Tod Verantwortung für die Gruppe übernahmen und sich um die Zukunft der verbleibenden Diplomanden und Doktoranden kümmerten. Insbesondere danke ich Svetlana für das Erledigen sämtlicher administrativer Aufgaben.

Des Weiteren gilt mein Dank Prof. Dr. Uwe Thiele. Nach Herrn Friedrichs Tod übernahm er die Betreuung meiner Arbeit, wobei der zweite Teil entstand. Ohne seine Hilfe wäre ich in diesem für mich neuen Forschungsgebiet völlig verloren gewesen. Ich freue mich sehr darüber, dass er die Nachfolge von Herrn Friedrich in Münster antritt. Menschlich wie wissenschaftlich könnte ich mir keinen besseren vorstellen.

Außerdem bedanke ich mich bei Prof. Dr. Andreas Heuer und Dr. Svetlana Gurevich für viele hilfreiche Diskussionen und Anregungen im Zusammenhang mit dem zweiten Teil der Arbeit.

Für das Anfertigen der Gutachten meiner Dissertation danke ich ein weiteres mal

Prof. Dr. Uwe Thiele sowie Prof. Dr. Joachim Peinke. Letzterem gilt außerdem mein Dank für fruchtbare Diskussionen im Zusammenhang mit der Kramers-Moyal-Analyse.

Für die gute Zusammenarbeit im Zusammenhang mit der Anwendung des Datenanalyseverfahrens auf Messdaten des optischen Experiments danke ich Prof. Dr. Cornelia Denz sowie Florian Hörner. Außerdem danke ich Konrad Berghoff und Martin Boguslawski dafür, dass sie mich auf die Experimente aufmerksam machten und den Kontakt vermittelten.

Für einige Diskussionen und die Beantwortung zahlreicher Fragen zu den Experimenten mit organischen Halbleitern danke ich Prof. Lifeng Chi und Dr. Wenchong Wang.

Für die Organisation meines Forschungsaufenthaltes in Peking danke ich Dr. Hedwig Roderfeld und Prof. Dr. Huaping Xu. Prof. Lifeng Chi sei für die Vermittlung des Kontaktes zu Prof. Dr. Qi Ouyang gedankt. Letzterem sowie Prof. Dr. Xi Zhang, Prof. Dr. Huaping Xu und Bin Yuan danke ich für die nette Gastfreundschaft und interessante wissenschaftliche Diskussionen. Außerdem danke ich Markus Wilczek dafür, dass er es in Peking vier Wochen lang mit mir in einem Doppelzimmer ausgehalten hat. Seine Gesellschaft trug maßgeblich dazu bei, dass ich die Zeit in sehr schöner Erinnerung behalte. Ohne ihn als Augenzeugen hätte man mir einige erlebte Geschichten wahrscheinlich nicht geglaubt.

Ein besonders großes Dankeschön an meinen Bürokollegen Dr. Oliver Kamps. Danke für die Organisation der vielen AG-Fahrten ins Kleinwalsertal, für aufbauende Worte und stetige Erheiterungsversuche während zwischenzeitlicher Durststrecken, für die Organisation der Fußballrunde, für zahllose Diskussionen und das stetige Interesse an meiner Arbeit sowie für emotionalen Beistand bei vielen dramatischen BVB-Spielen.

Für motivierende Worte und weitere spannende Diskussionen danke ich Dr. Maria Haase, Bernd Lehle und Dr. David Kleinhans.

Ich danke den bereits erwähnten Oliver, Svetlana und Uwe für das Korrekturlesen der Arbeit und der gesamten Arbeitsgruppe für eine schöne Arbeitsatmosphäre und allgegenwärtige Hilfsbereitschaft.

Für die Finanzierung meiner Arbeit während der letzten 16 Monate sowie des Forschungsaufenthaltes in Peking im Rahmen des Sonderforschungsbereiches TRR 61 danke ich der Deutschen Forschungsgemeinschaft und der National Natural Science Foundation of China.

Schließlich danke ich meiner Familie dafür, immer und in jeder Beziehung für mich da zu sein und ganz besonders natürlich meiner Frau Lisa, die für ihre Liebe und Unterstützung mindestens einen Ehrendoktor verdient hätte.